Designing a Terahertz Spatial Light Modulator

IMHOTEP THOMAS BOOTH

Designing a Terahertz Spatial Light Modulator

Imhotep T. Booth

A thesis submitted in partial fulfilment of the requirements for the degree of

Doctor of Philosophy

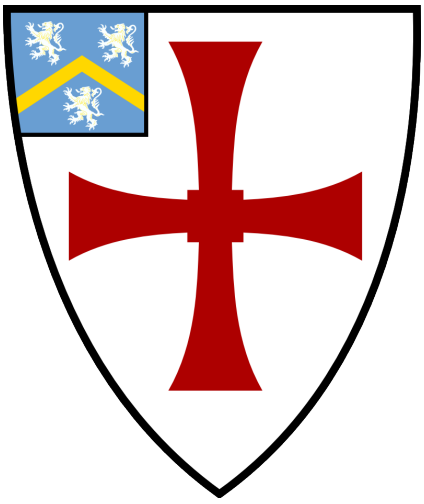

Quantum Light and Matter

The University of Durham

United Kingdom

April 2025

Designing a Terahertz Spatial Light Modulator

Imhotep T. Booth

Abstract

This thesis presents the design, development, and characterisation of a novel spatial light modulator operating in the terahertz (THz) regime. It addresses key limitations in current THz technologies, including the scarcity of efficient modulators with high spatial resolution, fast response times, and integration compatibility with THz imaging systems. The device employs a high-resistivity (5000 Ohm $\cdot$ cm), 480 µm-thick silicon wafer modulated via photoexcitation at intensities up to 1.5 W/cm^2 and wavelengths spanning 405–920 nm. Spatially patterned excitation is delivered using a digital micromirror device (DMD), enabling reconfigurable and high-resolution THz modulation. The modulator is integrated into a 550 GHz imaging system, where its performance is assessed in terms of spatial resolution, contrast, modulation depth, and frame rate. The system achieves real-time image formation with a diffraction-limited resolution of 340 µm and a modulation depth of 29%. Dynamic modulation tests demonstrate operational frame rates exceeding 10 kHz while maintaining consistent contrast. These results highlight the system's potential for applications in security screening, non-destructive testing, and biomedical imaging. Ultimately, this work bridges disciplines across materials science, photonics, and semiconductor engineering, delivering a scalable and efficient platform that advances the capabilities of THz modulation and imaging.

Supervisors: Prof. K.J. Weatherill and Prof. C.S. Adams

Acknowledgements

I would like to start by thanking my dearest and closest friend for his unrivalled support throughout the entirety of my project here at Durham and my life. Peter, whom I met at school, has lived with me for the last 10 years of my life before I started my time at Durham. He is always there to discuss anything on my mind from emotional difficulties to the very results in this thesis!

Kaviya whom I met here at Durham on the same course has helped me in countless ways through these last years, I only hope she knows how much I appreciate her assistance.

And, of course, my family, who supported me long before my PhD began. I would like to thank them for that continued support throughout the last few years completing this project, especially my father who took the time to begin teaching me all those years ago. Without his patience and dedication to my education, I would never have been able to reach this level.

My project was guided by Prof. Kevin Weatherill and Prof. Charles Adams. It was Prof. Weatherill who also carried out my interview prior to attending Durham, and from even that early moment, his interest in my work and progress was above and beyond. I cannot thank him enough for his patience and expertise in the field. Prof. Adams also was a key contributor to my progress at Durham, perhaps most notably in a short but sincere email just after I delivered my first year talk. I don't think he realises how much his few words have impacted my life for the better since.

During the majority of my first year, I was directed by Dr. Shuying Chen. Her kindness and dedication to my well-being greatly helped me on my way at the beginning of the course. I also would like to thank all the members of the THz team for their support and encouragement during my time at Durham.

Contents

Declaration

The work in this thesis is based on research carried out with the Quantum, Light and Matter group, Department of Physics, University of Durham, England. No part of this thesis has been submitted elsewhere for any other degree or qualification, and it is the sole work of the author unless referenced to the contrary in the text.

List of Figures

List of Tables

Nomenclature

AR Anti-Reflection

BF-TEM Bright Field - Transmission Electron Microscopy

CZ Czochralski

DMD Digital Micromirror Device

EDS Energy-Dispersive X-ray Spectroscopy

FCC Face Centred Cubic

FFT Fast Fourier Transmform

FIB Focused Ion Beam

FPAs Focal Plane Arrays

FSR Free Spectral Range

FZ Float Zone

HRFZ High Resistivity Float Zone

IR Infra-Red

LC-SLM Liquid Crystal - Spatial Light Modulator

MAPE Mean Absolute Percentage Error

MTF Modulation Transfer Function

R-RMSE Relative Root Mean Square Error

SAED Selected Area Electron Diffraction

STEM Scanning Transmission Electron Microscopy

TEM Transmission Electron Microscopy

THz Terahertz

TIR Total Internal Reflection

QCLs Quantum Cascade Lasers

Chapter 1

Introduction

Terahertz (THz) technology has emerged as a frontier in the field of electromagnetic research, offering vast potential across diverse applications such as medical imaging, security screening, and high-speed wireless communications. Despite its promise, the development of efficient THz modulators—a crucial component for controlling and utilising THz waves—remains a significant challenge [1]. Current THz modulator designs, including electro-optic [2], all-optical [3], and metamaterial-based modulators [4], have made strides but often fall short in modulation speed, efficiency, and integration with existing technologies [5]. This thesis seeks to address these limitations by exploring the design and development of a novel spatial THz light modulator, leveraging innovative modulation techniques to seamlessly integrate with existing THz imaging systems [6]. By advancing the capabilities of THz modulators, this research aims to bridge the so-called "THz gap" and unlock new avenues for applications of THz technology [7]. The results of this work could lead to more effective and versatile solutions in fields ranging from healthcare to industrial quality control, underscoring the transformative potential of THz technology.

1.1 Terahertz Band Gap

The THz band, spanning frequencies from 0.1 to 10 THz [8], occupies a unique position within the electromagnetic spectrum, situated between the microwave and

Infra-Red (IR) regions. This frequency range, often referred to as the "THz gap," is illustrated in **Figure 1.1** and presents both challenges and opportunities for scientific and technological advancement. Historically, the THz band has been underutilised due to the difficulties associated with generating, detecting, and modulating THz waves [9]. These challenges arise from the lack of efficient THz sources and detectors, often due to the technological limitations of traditional electronic and photonic devices, which are not optimised for this specific range.

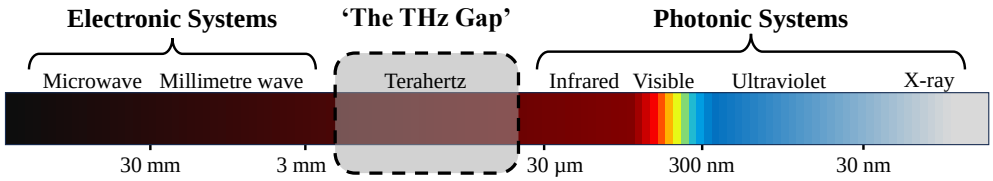

Figure 1.1: A chart of the electromagnetic spectrum ranging in wavelength from 300 mm to 3 nm, depicting commonly named regions to highlight the so-called 'THz band gap'. Additionally, regions of typical electronic-based and photonic-based systems are shown.

Recent advancements in materials science and semiconductor technology have started to unlock the potential of the THz band [10], allowing for the development of innovative devices and systems capable of overcoming the "THz gap." The key characteristics of the THz band include wavelengths ranging from 30 µm to 3 mm [11]. These wavelengths enable unique interactions with a wide variety of materials, facilitating non-ionising and non-invasive probing techniques [12]. The low photon energy of THz radiation, which lies within the millielectronvolt (meV) range, ensures its safety for biological tissues, making it particularly suitable for applications such as medical imaging and security screening [13], where non-invasive and safe techniques are of paramount importance.

While the THz band offers several advantages, its application in fields like medical imaging is hampered by significant challenges, notably its interaction with water molecules—a major component of biological tissues [14]. THz radiation is strongly absorbed by water due to the rotational transitions of water molecules within the THz frequency range, leading to high levels of attenuation

and scattering [15]. This presents a major obstacle for THz imaging in medical diagnostics, as it restricts the depth of penetration and the clarity of the image.

To address these challenges, researchers have proposed strategies such as the use of THz modulation devices to dynamically manipulate the amplitude of THz wavefronts. These devices enable adaptive beam shaping, allowing the circumvention of areas with a high water content [16]. By providing real-time control over THz wave amplitudes, modulators can enhance the depth of penetration and improve image resolution, optimising the propagation path through tissues and mitigating the effects of water absorption and scattering. This approach leverages the flexibility and precision of THz modulators to dynamically adapt to varying tissue compositions and environmental conditions, thus improving the effectiveness of THz imaging for medical diagnostics [17].

Despite these technological advances, the THz band remains challenging to harness due to the persistent lack of efficient sources and detectors [18]. Traditional electronic devices struggle to operate at these high frequencies, while photonic devices optimised for IR wavelengths do not perform well in the THz range [19]. However, progress in areas such as THz quantum cascade lasers [20], photoconductive antennas [21], and non-linear optical crystals [22] has begun to bridge this gap, making THz applications more viable [23]. These advancements indicate a promising future for the integration of THz technologies in various sectors, offering safer and more precise imaging solutions that can transcend the limitations of existing technologies.

1.2 THz Technology

Terahertz technology represents a rapidly evolving field that focuses on the development of devices and systems capable of generating, manipulating, and detecting THz radiation [1]. This technology stands out due to its unique properties, which distinguish it from other forms of electromagnetic radiation such as X-rays and IR

light. THz waves offer several advantageous characteristics, including the ability to penetrate a variety of non-metallic materials and provide spectroscopic information. These properties have spurred recent advancements in THz technology, leading to significant progress in areas such as THz imaging and modulation. Unlike X-rays, THz radiation is non-ionising, making it inherently safer for human exposure. In addition, the spectroscopic capabilities of THz waves allow for a detailed analysis of material properties, which can be leveraged for applications ranging from security screening and biomedical imaging to the detection of explosives and the development of advanced communication systems. This section will explore the current state of THz technology, examining the techniques and applications that drive its innovation, and set the stage for the specific work presented in this thesis.

1.2.1 Terahertz Imaging

Terahertz imaging is an emerging technology that capitalises on the distinctive interactions of THz waves with various materials, offering unique insights that are not possible with conventional imaging methods. This imaging modality is gaining significant attention in multiple fields, including medical diagnostics, security, and industrial inspections, due to its non-ionising nature and its ability to penetrate non-conductive materials such as plastics and ceramics [24, 25]. The primary mechanism behind THz imaging involves transmitting or reflecting THz waves through a sample, followed by the detection and analysis of the resulting signals [26, 27]. The contrast in THz images arises from variations in the absorption and reflection properties of different materials at THz frequencies [11], allowing for the identification of substances and structures that are invisible to other types of radiation, such as X-rays or infrared light [28, 29].

The fundamental principle of THz imaging lies in the unique absorption and reflection characteristics exhibited by different materials when exposed to THz radiation. For instance, water has a high absorption coefficient for THz waves, which can be exploited to differentiate between dry and wet materials or to identify biolo-

gical tissues with high water content [30, 31]. This capability makes THz imaging particularly useful for applications that require distinguishing between materials with varying moisture levels or detecting the presence of biological materials. Unlike X-rays, which are suitable for applications that require detailed internal images, such as medical diagnostics of bone fractures, THz radiation is non-ionising and poses no health risks with prolonged exposure. As a result, THz imaging offers a safer alternative for applications involving repeated imaging, particularly in healthcare settings.

Terahertz imaging systems are generally classified into time- and frequency-domain systems, each offering distinct advantages and limitations [32, 33]. Time-domain THz imaging systems utilise pulsed THz radiation to capture both the amplitude and phase information of the sample. This technique involves generating short pulses of THz radiation directed at a sample, and the transmitted or reflected pulses are then detected and analysed to reconstruct an image [34]. Time-domain systems are highly sensitive and can achieve high-resolution imaging, making them ideal for time-resolved studies and detailed material characterisation [35, 36]. For example, they can measure the thickness of layers, identify material compositions, and detect defects within structures [37, 38], owing to their ability to capture transient responses of a system or material.

In contrast, frequency-domain THz imaging systems employ continuous-wave THz sources and measure the response of a sample at specific THz frequencies. Although generally simpler and more cost-effective, these systems typically offer lower resolution compared to time domain systems [39, 40]. This is because they measure steady-state responses averaged over time, which can smooth out rapid changes and finer details, leading to a loss of transient information and reduced ability to resolve short-duration events. Despite this limitation, frequency-domain systems are valuable for applications where high speed and cost efficiency are more critical than high resolution, such as large-scale industrial inspections [9].

Several advanced imaging techniques are employed in THz imaging to enhance

its capabilities. Raster scanning is one such technique, involving the movement of a single-pixel detector across the sample in a systematic pattern, capturing data point by point to construct an image [41, 42]. While this method can be time-consuming, it is advantageous in applications requiring high spatial resolution and detailed analysis. Raster scanning is particularly useful in research and laboratory settings where precision is critical and the area of interest is relatively small. However, the slow speed of image acquisition makes raster scanning less suitable for applications requiring rapid image processing, such as real-time security screening.

An alternative to raster scanning is the use of Focal Plane Arrays (FPAs), which consist of a grid of detectors that can simultaneously capture THz images over a wide area, allowing parallel processing of data [43]. This capability significantly accelerates the imaging process compared to raster scanning, making FPAs well-suited for applications where rapid image acquisition is essential, such as security screening and industrial quality control. FPAs provide faster imaging while maintaining adequate resolution and sensitivity, although they may have lower resolution for very detailed analyses compared to raster scanning due to the limited pixel size and spatial sampling resolution [44]. Despite this, advancements in FPAs continue to improve their performance, making them increasingly viable for a wide range of applications.

Microbolometers are another type of detector used in THz imaging, measuring temperature changes induced by the absorption of THz radiation [45]. These detectors operate at room temperature, making them more practical and cost-effective than other detector types requiring cryogenic cooling. Microbolometers offer a good balance between performance and affordability, making them attractive for various applications, including portable and handheld THz imaging devices. However, their relatively lower resolution and sensitivity compared to more advanced detectors, such as superconducting arrays, may limit their suitability for applications that require extremely high sensitivity or precision [46].

Superconducting arrays, such as transition-edge sensors [47] and kinetic in-

ductance detectors [48], offer ultra-high sensitivity and fast response times, making them ideal for applications requiring precise measurements of weak THz signals. These detectors are particularly useful in environments with low-temperature requirements, such as astronomical observations or fundamental research in physics [49]. The exceptional sensitivity of superconducting arrays allows for the detection of faint THz signals that other detectors might miss, enabling more detailed and accurate imaging. However, the need for cryogenic cooling adds complexity and cost to the system, limiting their practicality for some applications. Despite these challenges, the superior performance of superconducting arrays makes them invaluable for high-end scientific research and specialised industrial applications.

Atomic imaging is another advanced technique that involves the use of atomic vapours or gases to detect and image THz radiation [50]. This technique leverages the unique interactions between THz waves and atoms to achieve high sensitivity and frequency selectivity. Atomic-based detectors are particularly suitable for spectroscopic applications and the study of fundamental THz interactions with matter. The sensitivity of atomic-based imaging systems allows for the precise characterisation of material properties and the detection of minute changes in THz signals. However, the complexity of these systems and their reliance on specific environmental conditions can pose challenges in terms of implementation and scalability. Despite these challenges, atomic-based imaging continues to be a valuable tool for advanced research and specialised applications, contributing to the overall advancement of THz imaging technologies.

Quantum Cascade Lasers (QCLs) play a crucial role in THz imaging, serving as efficient and tunable THz sources. QCLs operate by utilising inter-subband transitions in semiconductor superlattices to emit THz radiation. They offer high power and narrow linewidths, making them ideal for both time- and frequency-domain THz imaging systems. The development of THz, QCLs has been crucial in advancing the capabilities of THz imaging, enabling applications that require precise control over the frequency and intensity of emitted signals.

Terahertz imaging has a broad range of applications across different fields, largely due to its unique ability to penetrate various materials and its non-ionising nature [51]. In the field of security, THz body scanners are employed in airports and other high-security environments to detect concealed objects. These scanners use millimeter-wave technology to create a generic outline of a person's body rather than an anatomically accurate image, effectively maintaining passenger privacy while identifying hidden threats [40]. THz waves can penetrate clothing and packaging materials, revealing hidden weapons, explosives, and other contraband items. Unlike X-rays, THz radiation is non-ionising, making it safer for repeated use in security screenings.

In non-destructive testing applications, THz imaging is used to inspect the integrity of composite materials in the aerospace and automotive industries [52, 53]. THz waves can detect delamination, cracks, and other defects within composite structures, ensuring the reliability and safety of critical components without damaging them [1]. This capability is crucial to maintaining the high standards required in these industries, where the safety and performance of materials are paramount [54].

Medical imaging represents another promising area for THz technology. The non-ionising nature of THz radiation makes it a safer alternative to X-rays for medical applications [55]. THz imaging can be used to monitor burns, identify cancerous tissues, and detect dental cavities [56, 57]. For example, THz waves can differentiate between healthy and cancerous tissues based on their water content and other molecular differences, which could lead to more accurate cancer diagnoses and advances in Deoxyribonucleic Acid (DNA) related science [33, 58].

In the pharmaceutical industry, THz spectroscopy can analyse the molecular composition of substances, ensuring the quality and consistency of pharmaceutical products [59]. THz imaging can detect impurities, measure the thickness of coatings, and ensure uniformity in drug formulations [60]. Similarly, in chemical sensing, THz waves can identify and characterise chemical compounds, making

them useful for environmental monitoring and detection of hazardous materials [61]. While IR technology is also employed in these areas, THz technology offers unique advantages, such as reduced heating effects and enhanced sensitivity to broader structural interactions.

The continued development of THz imaging technologies promises significant advancements across multiple sectors, leveraging the unique properties of THz waves to achieve safe, effective, and innovative imaging solutions. As research progresses, the integration of THz imaging into existing systems and its application in new domains will likely lead to further breakthroughs and enhanced capabilities, solidifying its position as a critical tool in modern technology.

1.2.2 Terahertz Modulation

The design and development of THz modulators are pivotal in advancing THz technology. These modulators are essential for controlling the properties of THz waves, allowing their application in a wide range of fields, including high-speed communication systems and advanced imaging techniques. Efficient THz modulation involves manipulating the amplitude, phase, or polarisation of THz radiation, enabling dynamic control over THz signals. Despite the promising potential of THz waves, which can penetrate materials opaque to visible and IR light such as clothing, paper, and certain plastics, achieving efficient THz modulation is challenging [62]. This difficulty arises from the longer wavelengths of THz radiation and the lack of suitable materials and devices capable of directly manipulating them at high resolutions.

In classical optics, passive elements such as lenses, mirrors, and gratings are sufficient for many imaging and beam-shaping applications. However, in the THz regime, passive elements alone cannot provide the dynamic control required for modern applications. This is due to the inherent limitations in spatial reconfigurability and speed offered by passive optics. Active THz modulation is essential in

systems that demand real-time adaptability, such as dynamic beam steering, image encoding, and material discrimination in scattering media. Moreover, THz imaging is particularly sensitive to environmental variations, especially water content, and thus benefits from modulators that can adaptively optimise the wavefront during operation. Without active control over amplitude or phase, many of the potential advantages of THz technology, such as safe, non-ionising imaging in biomedical or security contexts, remain underutilised. Therefore, the integration of fast, reconfigurable modulation elements marks a key differentiator between proof-of-principle THz systems and deployable, high-performance solutions.

It should be noted that this thesis does not explore electro-optic or interferometric single-mode THz modulator systems. Instead, it focuses on the design and implementation of a spatially reconfigurable THz modulator based on optical excitation of a high-resistivity silicon wafer. Modulation is achieved indirectly through the projection of spatially patterned visible light, using a Digital Micromirror Device (DMD), which induces localised changes in carrier concentration and thus modulates THz transmission spatially across the wafer. This configuration distinguishes itself from classical amplitude or phase modulators by offering pixel-level spatial control over THz wavefronts, enabling integration into high-resolution imaging systems.

A fundamental challenge in THz modulation is the absence of materials and devices optimised for the THz frequency range. Traditional electronic and photonic devices, such as the DMD in this work, are typically designed for visible light and face significant limitations when applied to THz radiation. For example, DMDs consisting of an array of micromirrors that tilt to reflect light into or away from an optical path are highly effective in modulating visible light. However, they are not as effective for THz waves due to the larger wavelengths involved. The pixel size and mechanical movement of the micromirrors are not optimised for THz frequencies, leading to substantial diffraction and scattering losses. Furthermore, the materials used in conventional DMD technologies often lack the necessary proper-

ties to interact efficiently with THz radiation.

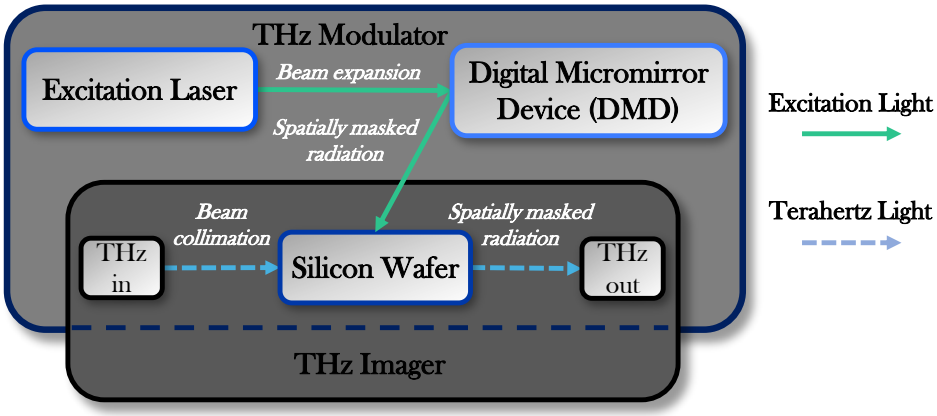

Figure 1.2: A flow chart diagram showing a THz Modulator, and a THz imager. Typical components for such devices are also displayed being a spatial mask (DMD), an excitation laser, and a semiconductor (silicon wafer) as the interface between the modulator and the imager.

To overcome these limitations, innovative modulation techniques have emerged that utilise advances in materials science and semiconductor technology. One promising approach involves the use of semiconductors, such as silicon, as in this work, which can be photoexcited to generate free carriers that interact with THz waves, effectively modulating their amplitude. Optical excitation allows for local changes in silicon conductivity, enabling precise control over THz wave interactions. However, achieving spatial modulation of THz waves at a fine resolution necessitates additional techniques, such as using spatially dynamic masks to control where photoexcitation occurs on the semiconductor surface. In this context, DMDs can play a pivotal role, not by directly modulating THz waves, but by projecting dynamic optical patterns onto the silicon surface, thereby creating a reconfigurable photoexcitation mask that allows for high-resolution control over THz wave properties. This design for the modulator is illustrated in **Figure 1.2** in a flowchart form along with the connections to the THz imager for ease of understanding.

Alternatively, electro-optic modulators are also widely employed for THz modulation. These modulators utilise materials whose refractive index changes when subjected to an electric field, permitting precise control of THz wave properties

such as amplitude and phase [63, 64]. Materials like lithium niobate and gallium arsenide are commonly used due to their significant electro-optic coefficients. Electro-optic modulators achieve high modulation speeds and are compatible with existing electronic and photonic systems [65–67], making them suitable for applications requiring rapid signal processing.

All-optical modulators, on the other hand, exploit the interaction between THz waves and optical signals in non-linear materials [68]. Techniques such as the Kerr effect [69, 70], where the refractive index of a material changes in response to the intensity of the optical signal, enable high-speed modulation. All-optical modulators offer faster modulation capabilities than their electro-optic counterparts, making them ideal for applications demanding rapid signal processing [71] and integration with high-speed imaging systems [72].

Another alternative is metamaterial-based modulators which use engineered structures with electromagnetic properties not found in natural materials [73–75]. These metamaterials can be designed to exhibit specific responses to THz waves, such as negative refractive indices or tailored absorption characteristics. By carefully designing the structure of these metamaterials, efficient THz modulation systems can be achieved [76, 77], allowing for significant flexibility in controlling THz wave properties.

Semiconductors like graphene and indium phosphide have also shown promise in THz modulation due to their high electron mobility and tunability. These materials facilitate ultrafast THz modulation, potentially reaching speeds necessary for next-generation wireless technologies [78, 79]. The integration of semiconductor technologies with silicon photonics is paving the way for more efficient and compact THz modulators [80, 81], enhancing their practicality for a wide range of applications.

Terahertz modulators play a crucial role in various applications, providing dynamic control over THz signals to optimise the performance of THz technolo-

gies. In high-speed communication systems, THz frequencies offer the potential for data rates that surpass current wireless technologies, making them attractive for high-speed communication and data transfer. THz modulators enable ultra-high-speed data transmission by dynamically controlling the amplitude, phase, and frequency of THz waves, supporting data-intensive applications such as streaming high-definition video and real-time data analytics [82].

In imaging systems, THz modulators allow for the dynamic manipulation of THz wavefronts [63, 64], enabling adaptive beam shaping and enhancing image resolution. This capability is particularly valuable in medical imaging, where THz modulators can optimise the propagation path through tissues, reducing the detrimental effects of absorption and scattering, and thereby improving image clarity.

In spectroscopic applications, THz modulators are employed to selectively modulate THz waves, enabling the precise characterisation of material properties. This capability is crucial for chemical sensing, environmental monitoring, and the detection of hazardous materials, where accurate identification and analysis of chemical compounds are essential.

Significant progress has been made in developing THz modulators, driven by advancements in materials science and semiconductor technology. Recent developments include the use of metamaterials and semiconductors with high electron mobility, which exhibit exceptional modulation speeds and tunability. These advancements have paved the way for integrating THz modulators into existing systems, enhancing their practicality and expanding their applications across various fields.

In recent years, several THz modulator systems have demonstrated significant advances in spatial resolution and modulation speed, but persistent limitations remain. Modulation speeds now span from single-digit kHz to, in some metasurface implementations, low-GHz levels, while typical spatial resolutions lie within the 400–800 µm range. The reported values represent experimentally realised perform-

ance in published systems, rather than theoretical proposals or simulations. For example, a 2019 Nanomaterials review reports modulation speeds rising from kHz to GHz over the past decade, with modulation depths nearing 100% at kHz rates; however, spatial resolution remains relatively coarse [83]. Another 2022 MDPI Micromachines survey frames the challenges in achieving true pixel-level THz SLMs, citing typical pixel pitches of several hundred micrometres [84]. In contrast, this thesis presents an optically addressed silicon device achieving 340 µm spatial resolution—near the diffraction limit at 550 GHz (545 µm wavelength) with dynamic modulation exceeding 10 kHz frame rate, thereby providing a benchmark for both resolution and speed simultaneously.

In conclusion, designing and developing efficient THz modulators is critical to harnessing the full potential of THz technology. By overcoming the challenges associated with traditional modulation techniques and leveraging innovative approaches, THz modulators can enhance the capabilities of THz systems and unlock new opportunities for their application. This research aims to advance the field of THz modulation by exploring novel designs and materials, contributing to the broader adoption and integration of THz technologies in both scientific and practical domains.

1.3 Thesis Overview

The research in this thesis aims to address the persistent challenges in THz modulation and imaging discussed, particularly the limitations in modulation speed, efficiency, and integration with current technologies. By advancing the capabilities of THz modulators, this study seeks to bridge the technological gap in the THz frequency range and unlock new avenues for practical applications across diverse fields, including medical diagnostics, security screening, and high-speed communication systems.

Chapter 2 lays the foundational theoretical principles underpinning THz

modulation and imaging. It delves into the physics of THz interactions with materials, exploring the unique properties of THz waves that facilitate their application in various domains. This chapter provides a comprehensive framework for understanding the complex interactions involved in THz modulation, setting the stage for the experimental investigations that follow.

Chapter 3 outlines the experimental setup and methodologies employed in designing, fabricating, and testing the modulator. It provides a detailed account of device selection, component fabrication processes, and measurement techniques used to evaluate the modulator's performance. The chapter emphasises the importance of selecting suitable materials that can interact effectively with THz waves, highlighting the role of semiconductors and metamaterials in achieving efficient modulation.

In **Chapter 4**, the thesis presents the results of experimental investigations into the Digital Micromirror Device (DMD), evaluating its performance across various applications and its integration with the modulator. This chapter assesses the DMD's capability to project dynamic optical patterns onto a semiconductor surface, thereby facilitating high-resolution spatial modulation of THz waves. The findings from these investigations inform the subsequent development and optimisation of the modulator.

Chapter 5 focuses on the characterisation of silicon, the chosen semiconductor for the modulator. It evaluates silicon's performance in numerous applications, examining its suitability for THz modulation through photoexcitation techniques. This chapter provides insights into the electronic properties of silicon and its interaction with THz waves, underscoring its role as a critical component in the modulator's design.

In **Chapter 6**, the thesis explores the modulator's application within a high-resolution atomic-based imager. Evaluations are performed on its effectiveness in compatible high resolution image creation, image contrast, and fast dynamic modu-

lation. The integration of the modulator with the THz imager aims to demonstrate its potential to enhance imaging capabilities, providing valuable information on the practical applications of THz technology.

The thesis culminates in **Chapter 7**, which summarises the key findings and their implications for the field of THz technology. It highlights the contributions of this research to the advancement of THz modulators and imaging systems, offering suggestions for future research directions that could further enhance the design and development of THz spatial light modulators. This chapter underscores the transformative potential of THz technology, emphasising the role of innovative modulation techniques in bridging the THz gap and enabling new applications across scientific and practical domains.

In summary, this thesis aims to contribute significantly to the field of THz technology by designing and developing a spatial THz light modulator that addresses existing challenges and enhances the integration of THz systems. By leveraging novel materials and techniques, the research advances the understanding and application of THz modulators, paving the way for more efficient and versatile solutions in various sectors. The outcomes of this work have the potential to revolutionise the use of THz technology, offering more precise and innovative imaging and communication solutions.

Chapter 2

Theoretical Framework for Silicon Excitation

In this chapter, we delve into the theoretical aspects of silicon excitation, exploring its fundamental electronic properties which we then use to develop a foundation for its electro-optical phenomena. By exploiting carrier dynamics and recombination properties of silicon, the electro-optical properties can be manipulated to alter THz propagation through the sample. This propagation is examined using Fresnel transfer matrix equations. The resulting comparison in propagation between excitation states known as modulation depth is then arrived at, providing a numerical measure of the designed modulator's performance. In addition to formulaic explanations in this chapter, graphical simulations of the theory are used throughout to enhance comprehension of the entire modulation process. The concepts discussed here will be utilised in **Chapter 3** for the development of experimental methods as well as in **Chapter 4**, **Chapter 5**, and **Chapter 6** to enhance understanding of the results.

2.1 Introduction

Understanding silicon excitation theory is crucial for designing efficient THz modulators. The properties of silicon, including its band structure, charge carrier dynamics, and doping capabilities, make it an ideal candidate for THz applications. Silicon's indirect band gap allows for effective manipulation of electrons and holes, which is essential for modulating THz radiation. The relevance of silicon in THz technology lies in its ability to be excited through various mechanisms, such as optical, electrical, and thermal excitation. These excitation methods facilitate the generation and control of charge carriers, thereby altering the material's conductivity and refractive index. This capability is vital for THz devices, which require precise control over wave propagation and interaction with matter.

This chapter provides a comprehensive overview of silicon's electronic properties and the fundamental mechanisms of excitation. By examining carrier dynamics, recombination processes, and the interaction of excited silicon with THz waves, we set the stage for a detailed exploration of how these factors contribute to the design and performance of silicon-based THz modulators.

2.2 Electronic Properties of Silicon

Silicon's electronic properties are fundamental to its role in THz modulation and are characterised by its crystal structure, band structure, and carrier dynamics. Silicon crystallises in a diamond cubic lattice, which significantly influences its electronic behaviour. The silicon atoms are arranged in a tetrahedral configuration, creating a semiconductor with an indirect band gap of approximately 1.12 eV at room temperature [85]. This band gap is a crucial parameter because it dictates the energy required to excite electrons from the valence band to the conduction band, thus generating electron-hole pairs.

2.2.1 Silicon Band Gap

The electronic band structure of silicon is seen in **Figure 2.1** ***a)***, depicting the relationship between the energy levels and the high symmetry wave vectors [86]. These high symmetry wave vectors are determined from the first Brillouin zone which is a diamond cubic lattice represented in reciprocal space seen in **Figure 2.1** ***b)***. The band structure reveals that the valence band maximum and the conduction band minimum do not occur at the same wave vector; hence the term 'indirect band gap.' This indirect nature impacts the absorption of photons; only photons with sufficient energy can excite electrons across the band gap. Additionally, a non-radiative process known as phonon interaction occurs, where excess energy is dissipated as heat in an energy packet. This quasiparticle associated with vibrations of the crystal lattice enables conservation of momentum in the excitation process. This characteristic influences silicon's optical properties, making it less efficient for light absorption compared to direct band gap materials but still effective for THz applications.

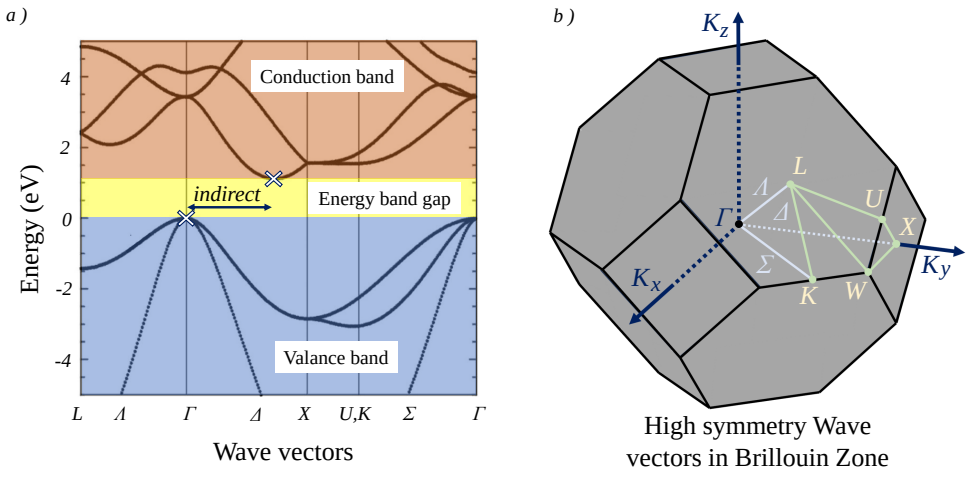

Figure 2.1: ***a)*** The electronic band structure of silicon demonstrating the energy levels associated with high symmetry wave vectors of the silicon lattice. ***b)*** The first Brillouin zone diagram for a primitive cell in reciprocal space of a Face Centred Cubic (FCC) lattice showing the high symmetry wave vector definitions used in the band structure graph [87].

2.2.2 Carrier Mobility

Carrier dynamics in silicon are defined by the behaviour of mobile electrons and holes. These carriers are intrinsic to the silicon before excitation, and increase in number during excitation. The mobility of these carriers is a critical parameter, influenced by factors such as doping, temperature, and the presence of defects.

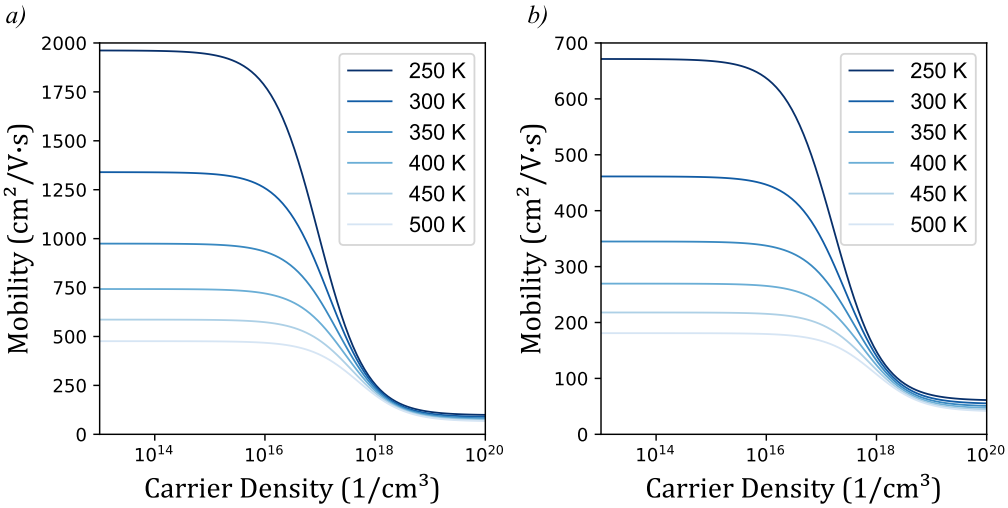

Figure 2.2: Mobility of charge carriers against charge carrier density within the silicon showing both electron ***a)*** and hole ***b)*** mobility characteristics for varying temperatures between 250 and 500 K [88].

Doping is a controlled process in which impurities are introduced into silicon to alter its electrical properties. Pentavalent (n-type) doping, achieved by adding elements such as phosphorus or arsenic, introduces extra electrons, while trivalent (p-type) doping, achieved with elements such as boron, creates holes. The concentration and type of dopants determine the free charge carrier density and hence the carrier mobility of the material. At room temperature, the electron mobility in intrinsic silicon is approximately 1300 cm^2/Vs whereas hole mobility is roughly 300 cm^2/Vs as seen in **Figure 2.2**. These values are subject to change with doping, which introduces additional energy levels within the band gap [88], modifying electrical conductivity and carrier concentration.

As the density of the charge carriers increase, the mobilities of both of these

carriers decrease. Adjusting the temperature of silicon mainly impacts the maximum possible mobilities in silicon, seen at the lower end of the carrier density. It should be noted that later the lasers responsible for the excitation process can lead to increased temperatures on the silicon wafer thus slightly affecting carrier mobility.

2.2.3 Wafer Resistivity

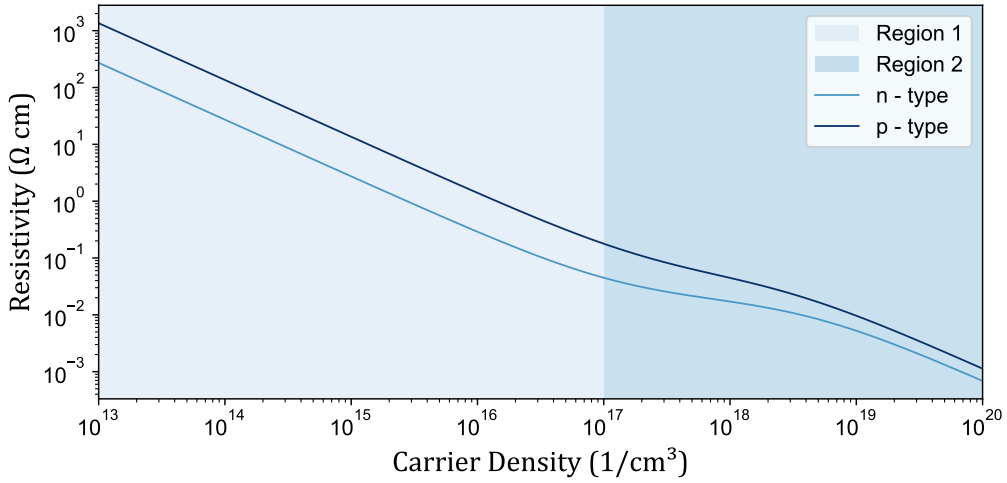

Figure 2.3: Resistivity against charge carrier density within the silicon showing both n- and p-type characteristics from **Equation 2.1**. Region 1 depicts a linear relationship between n and p-type characteristics, while region 2 contains a non-linear relationship.

Resistivity is another fundamental property of silicon, one that quantifies how strongly a material opposes the flow of electric current. While the mobility of holes and electrons provides insight into the ease with which charge carriers can move through silicon, resistivity [89], defined as

$$\rho_{\mathrm{n,p}} = \frac{1}{Ne\mu_{\mathrm{e,h}}}, \tag{2.1}$$

offers a more comprehensive picture by encompassing not only the electron or hole mobility (μ_{e} or μ_{h} respectively) but also the concentration of these charge carriers (N), and electron charge (e). Hence, a better understanding of the general ability of the material to conduct electrical current is required, as seen in **Figure 2.3**.

Pure, intrinsic silicon has a low carrier density and therefore also a high resistivity as the conductivity of the silicon has decreased. Alternatively, heavily doped silicon has an increased carrier density and, therefore, corresponds to a decreased resistivity and an increase in conductivity.

2.2.4 Justification for Silicon

The decision to use silicon as the active substrate in this spatial THz light modulator was made based on a combination of electronic performance, fabrication compatibility, material availability, and thermal and mechanical properties. While alternative materials such as germanium and compound semiconductors (e.g. InP, GaAs) offer attractive physical properties, silicon remains the most balanced and scalable option for this application.

From an electronic standpoint, silicon's indirect band gap of 1.12 eV is well-suited for optical excitation using commercially available laser wavelengths. This range permits efficient generation of free carriers at moderate powers without risking excessive thermal loading. Germanium, by contrast, has a smaller band gap (approximately 0.66 eV), making it more susceptible to thermal noise and unsuitable for the same range of pump wavelengths without introducing dark current or extraneous background effects.

Fabrication-wise, silicon benefits from decades of development in the computer industry, offering highly refined surface preparation, doping, and wafer-scale uniformity. In contrast, germanium wafers often suffer from higher costs, lower defect tolerances, and limited high-resistivity substrate options. The high-resistivity float-zone silicon used here is commercially available and well-characterised, enabling minimal intrinsic free-carrier absorption before excitation. Such high-resistivity wafers are not widely available for many alternative materials.

Silicon also offers exceptional thermal conductivity, which assists in dissipating heat from the localised optical excitation during high-speed modulation. Its

mechanical hardness and chemical stability further allow for repeated experimental testing and compatibility with optical and THz systems.

While materials such as GaAs exhibit higher electron mobilities and could offer faster carrier response, their optical transparency windows and costs pose major drawbacks. Furthermore, achieving high spatial modulation resolution requires wide-bandgap behaviour and excellent carrier confinement at micron scales properties well met by silicon when passivated and polished appropriately.

Thus, the choice of silicon reflects a deliberate optimisation across optical compatibility, spatial resolution, fabrication readiness, and system integration requirements. This ensures the approach remains reproducible, scalable, and consistent with future photonic integration.

2.3 Electro-optical Phenomena

Silicon demonstrates a variety of electro-optical phenomena when subjected to electromagnetic fields. This section begins by examining the theoretical foundations through the Drude model, which provides insight into these phenomena. We then extend the discussion by integrating the results from the Drude conductivity equations with plasma frequency equations to derive the permittivity characteristics of silicon. This framework lays the groundwork for understanding how these characteristics evolve upon excitation of silicon, leading to subsequent changes in its electro-optical properties.

2.3.1 Drude Conductivity

The classical Drude model provides a framework for understanding the behaviour of charge carriers in silicon when interacting with THz waves by expressing the complex conductivity in terms of incident angular frequency:

$$\tilde{\sigma}(\omega) = \frac{\sigma_0}{1 - i\tau_{\mathrm{m}}\omega_{\mathrm{THz}}}, \tag{2.2}$$

where $\sigma_0 = \frac{Ne^2\tau_m}{m}$ from Ohm's law [90], N is the free charge carrier density, m is the electron mass, τ_m is the momentum relaxation lifetime which is derived as $\tau_m = (\frac{m_e\mu_e}{e} + \frac{m_h\mu_h}{e})/e$ in which $m_{e,h}$ and $\mu_{e,h}$ are the effective masses and mobilities of the electrons and holes respectively, and ω_{THz} is the incident angular THz frequency.

The Drude model is well-suited for explaining THz modulation in photoexcited silicon because it provides a simple yet accurate description of free charge carrier behaviour under an electric field, focusing on their density and mobility. Unlike quantum mechanical models [91], which require detailed consideration of band structure and quantum effects, or the Boltzmann transport equation [92], which involves complex non-equilibrium dynamics, the Drude model captures the essential physics with fewer assumptions and computational demands. This balance between simplicity and accuracy makes the Drude model optimal for understanding and designing spatial THz modulators using silicon, where macroscopic conductivity changes are the primary concern.

2.3.2 Plasma Frequency

Another key characteristic of silicon is its plasma frequency which represents the natural oscillation frequency of free charge carriers in a material when displaced from their equilibrium position. Plasma frequency [93] is denoted by ω_{plas} where

$$\omega_{plas} = \sqrt{\frac{(N_0 + N_{ex})e^2}{m_e\epsilon_0}}, \tag{2.3}$$

in which, ϵ_0 is the permittivity of free space, and N_0 is the charge carrier density present within the silicon before excitation occurs, and N_{ex} is the additional charge carriers resulting from the excitation process.

The plasma frequency plays a crucial role in the determination of the optical properties of silicon. It marks the boundary between reflective and transparent behaviour. For frequencies below the plasma frequency, the material behaves like

a metal, reflecting electromagnetic waves. For frequencies above the plasma frequency, the material becomes transparent and allows the waves to pass through. In terms of modulation, if the plasma frequency remains below the incident THz frequency, such as when no additional N_{ex} are present, silicon will allow THz waves to pass through with minimal reflection, acting as a transparent medium.

In contrast, when additional charge carriers are present, there is a shift in the plasma frequency above the incident THz frequency, and silicon will reflect the THz waves more effectively, acting as a mirror and thus modulating the signal.

2.3.3 Permittivity Dynamics

By using the relationship $\tilde{\epsilon}(\omega) = \epsilon_\infty + \frac{i\tilde{\sigma}(\omega)}{\epsilon_0 \omega_{\text{THz}}}$, the complex conductivity of the silicon from the Drude model in **Equation 2.2** can be combined with the plasma frequency of the silicon in **Equation 2.3** to be rewritten as the Drude-Lorentz complex dielectric function [94] for the permittivity of the silicon:

$$\tilde{\epsilon}(\omega) = \epsilon_\infty - \frac{\omega_{\text{plas}}^2}{\omega_{\text{THz}}^2 + i\gamma\omega_{\text{THz}}}. \tag{2.4}$$

Here γ is the damping rate specific to the silicon such that $\gamma = \frac{1}{\tau_m}$, and ϵ_∞ is the high-frequency dielectric constant [95] which is a background constant specific to the silicon at 11.7. This relationship now allows us to express the permittivity of the silicon sample relative to its total charge carrier density at a given incident THz frequency. This is crucial to allow us to compare and analyse how inducing additional charge carriers directly affects the dielectric properties of silicon during modulation of any given THz frequency.

2.4 Carrier Generation, Diffusion, and Recombination

The understanding of charge carrier dynamics is crucial in the development of spatial THz light modulators as we have seen that charge carriers play a fundamental role in determining the electro-optical properties of the modulator. When silicon

is excited, energy is absorbed, causing the promotion of electrons from the valence band to the conduction band, thereby generating electron-hole pairs.

Upon generation in silicon, the processes of recombination of charge carriers play a crucial role in influencing THz modulation. Recombination, where electrons in the conduction band return to the valence band and annihilate holes, occurs through various mechanisms, each with distinct effects on the dynamics of charge carriers, as shown for reference in **Figure 2.4**. Understanding these processes is essential for optimising the efficiency of silicon-based THz modulators. The dynamics of these charge carriers—including their generation, recombination, and transport—significantly influence the modulator's performance.

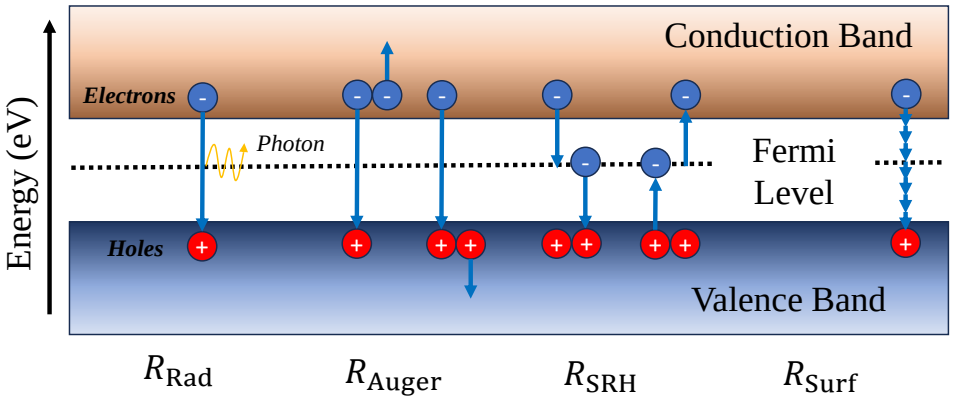

Figure 2.4: Schematic of recombination mechanisms for radiative (R_{Rad}), Auger (R_{Auger}), SRH (R_{SRH}), and surface (R_{Surf}) recombination. Demonstrating the transitions between the conduction and valence bands in each case.

2.4.1 Carrier Generation

There are three primary mechanisms for exciting silicon: optical, electrical, and thermal excitation. Each mechanism has unique advantages and applications in the context of THz technology. Optical excitation offers high-speed and precise control, making it suitable for applications requiring rapid modulation, and it will be the chosen mechanism for excitation in this work.

Optical excitation can be achieved using laser sources with wavelengths less

than 1107 nm, providing a controllable and efficient means of generating charge carriers when the photon energy is higher than that of the energy band gap ($\hbar\omega_{\mathrm{ex}} \geq E_{\mathrm{g}}, \omega_{\mathrm{ex}} = \frac{2\pi c}{\lambda_{\mathrm{ex}}}$). The efficiency of the process is influenced by factors such as the wavelength of light (λ_{ex}), intensity, and duration of exposure. Shorter wavelengths, closer to the blue and ultraviolet spectrum, are more effective at generating carriers due to higher photon energy. The intensity and duration of the light exposure also play critical roles, as higher intensities and longer exposures increase the number of carriers generated, enhancing the modulation depth.

When analysing the rate of charge carrier generation in silicon under photo-excitation, we begin with the fundamental relationship that describes how light is absorbed within a semiconductor material. The Beer-Lambert law is essential in this context, as it quantifies the attenuation of light as it propagates through a medium [96]. Mathematically, the intensity of light $I(z)$ at a depth z within the silicon is given by:

$$I(z) = I_0 \mathrm{e}^{-\alpha z}, \tag{2.5}$$

where I_0 is the initial light intensity at the surface of the silicon, α is the absorption coefficient of the material, and z is the distance from the surface. The absorption coefficient α is excitation wavelength dependent and determines how effectively silicon absorbs photons at a given excitation wavelength. It is defined as $\alpha = \frac{4\pi\kappa_{\mathrm{ex}}}{\lambda_{\mathrm{ex}}}$ where κ_{ex} is the imaginary part of the complex refractive index of the semiconductor ($\tilde{n}_{\mathrm{ex}} = n_{\mathrm{ex}} + i\kappa_{\mathrm{ex}}$) [97].

The generation rate $G(z)$ of electron-hole pairs at depth z can then be given by the product of the absorption coefficient and the local photon flux in the equation

$$G(z) = \frac{\alpha I_0}{\hbar\omega_{\mathrm{ex}}}(1 - R)\mathrm{e}^{-\alpha z}, \tag{2.6}$$

where $\hbar\omega_{\mathrm{ex}}$ is the energy of the incident photons and R is the reflectivity of the silicon surface [98]. The reflectivity value, defined as $R = \left|\frac{(1-\tilde{n}_{\mathrm{ex}})}{(1+\tilde{n}_{\mathrm{ex}})}\right|^2$, comes from the complex refractive index of the semiconductor [97].

2.4.2 Carrier Diffusion

Once carriers are generated, their movement within the semiconductor can be described by the current density, which includes contributions from both drift and diffusion processes. The drift current arises from the motion of the carriers under the influence of an electric field. When an electric field $\mathbf{E}$ is applied across the semiconductor, the carriers experience a force that drives them in the direction of the field (for electrons) or opposite to the field (for holes). The drift current density $\mathbf{J}_{\text{drift}}$ for electrons and holes in an electric field $\mathbf{E}$ can be expressed respectively as:

$$\mathbf{J}_{\text{drift:e,h}} = eN_{\text{e,h}}\mu_{\text{e,h}}\mathbf{E}. \tag{2.7}$$

Diffusion Current arises from the movement of carriers from regions of high concentration to regions of low concentration, driven by concentration gradients. The diffusion current density $\mathbf{J}_{\text{diff}}$ for electrons is given by Fick's first law [99]:

$$\mathbf{J}_{\text{diff}} = eD_{\text{e}}\frac{dN_{\text{e}}}{dz}, \tag{2.8}$$

where D_{e} is the diffusion coefficient for electrons (this can be substituted for D_{h} to calculate $-\mathbf{J}_{\text{diff}}$ for holes), $\frac{dN_{\text{e}}}{dz}$ is the concentration gradient of electrons (this must be substituted for $\frac{dN_{\text{h}}}{dz}$ when calculating $-\mathbf{J}_{\text{diff}}$ for holes).

The diffusion coefficients are derived from the Einstein Relationship [100] such that

$$D_{\text{e,h}} = \mu_{\text{e,h}}\frac{k_{\text{B}}T}{e}, \tag{2.9}$$

where k_{B} is Boltzmann's constant and T is the temperature of the wafer. Combining **Equation 2.7**, **Equation 2.8**, and **Equation 2.9**, we arrive at a definition for the electron current density:

$$\mathbf{J}_{\text{e}} = eN_{\text{e}}\mu_{\text{e}}\mathbf{E} + eD_{\text{e}}\frac{dN_{\text{e}}}{dz}. \tag{2.10}$$

Solving this equation allows us to calculate the diffusion of charge carriers within the silicon.

2.4.3 Radiative Recombination

Radiative recombination, seen in **Figure 2.4**, also known as band-to-band recombination, occurs when an electron recombines directly with a hole, emitting a photon. This process is less significant in indirect bandgap materials such as silicon, where the recombination process typically involves phonons to conserve momentum. The rate of radiative recombination R_{Rad} can be expressed as follows:

$$R_{\mathrm{Rad}} = BN_{\mathrm{e}}N_{\mathrm{h}}, \tag{2.11}$$

where B is the radiative recombination coefficient. This is a well-documented coefficient and can be extracted from existing literature [101].

2.4.4 Auger Recombination

Auger recombination, seen in **Figure 2.4**, is a non-radiative process in which the recombination energy of an electron-hole pair is transferred to another electron or hole, which is then excited to a higher energy state within the same band. This process is significant under high carrier injection conditions such as photoexcitation. The Auger recombination rate R_{Auger} is given by:

$$R_{\mathrm{Auger}} = C_{\mathrm{e}}N_{\mathrm{e}}^2N_{\mathrm{h}} + C_{\mathrm{h}}N_{\mathrm{e}}N_{\mathrm{h}}^2, \tag{2.12}$$

where $C_{\mathrm{e,h}}$ are the Auger recombination coefficients for electrons and holes respectively. The Auger recombination coefficients are also well-researched values from semiconductor physics and can be taken from literature [102].

2.4.5 SRH Recombination

Shockley-Read-Hall (SRH) recombination, seen in **Figure 2.4**, also known as trap-assisted recombination, occurs through defect states within the bandgap, which act as recombination centres. These defects capture an electron and a hole in two

separate events, facilitating their recombination. The rate of SRH recombination R_{SRH} is given by:

$$R_{\mathrm{SRH}} = \frac{N_{\mathrm{e}}N_{\mathrm{h}} - N_0^2}{\tau_{\mathrm{h}}(N_{\mathrm{e}} + N_{\mathrm{e1}}) + \tau_{\mathrm{e}}(N_{\mathrm{h}} + N_{\mathrm{h1}})}, \tag{2.13}$$

where $\tau_{\mathrm{e,h}}$ are the carrier lifetimes for electrons and holes respectively, and $N_{\mathrm{e1,h1}}$ are the equilibrium concentrations of electrons and holes in the presence of trap states respectively.

2.4.6 Surface Recombination

Surface recombination, seen in **Figure 2.4**, is a critical phenomenon that occurs at interfaces between the semiconductor material and its surrounding environment or at the boundaries of different materials within a device. In silicon-based THz spatial light modulators, surface recombination can significantly impact device performance, especially in structures with high surface-to-volume ratios.

Surface recombination occurs because the atomic bonds at the surface of a semiconductor are often incomplete, leading to the formation of surface states or traps within the bandgap. These traps can capture carriers, leading to recombination. The rate of surface recombination R_{Surf} is typically characterised by the surface recombination velocity S, which describes how quickly carriers recombine at the surface:

$$R_{\mathrm{Surf}} = \frac{S(N_{\mathrm{e}}(z=0) + N_{\mathrm{h}}(z=0))}{2}, \tag{2.14}$$

where $N_{\mathrm{e,h}}(z=0)$ are the electron and hole concentrations at the surface or specifically at depth $z = 0$. Due to the importance of reducing recombinations, and ensuring that generation rates are as high as possible, the majority of THz modulators utilise surface passivation techniques [103] to reduce the dangling bonds responsible for the high R_{Surf} rates.

2.4.7 Carrier Lifetime and Resolution

The total bulk recombination rate (R_{bulk}) in a semiconductor is the sum of the rates of all individual recombination mechanisms excluding surface recombination rates. These processes occur simultaneously and independently, meaning that their contributions to the total recombination rate are additive such that

$$R_{\text{bulk}} = R_{\text{Rad}} + R_{\text{Auger}} + R_{\text{SRH}}. \tag{2.15}$$

The bulk carrier lifetime (τ_{bulk}) is a crucial parameter that characterises how long, on average, a carrier (electron or hole) exists before recombining. The inverse of the lifetime of the bulk carrier is equal to the sum of the inverses of the lifetimes associated with each recombination process [104]. This relationship can be expressed:

$$\frac{1}{\tau_{\text{bulk}}} = \frac{1}{\tau_{\text{Rad}}} + \frac{1}{\tau_{\text{Auger}}} + \frac{1}{\tau_{\text{SRH}}}. \tag{2.16}$$

By calculating τ_{bulk} along with diffusion coefficients from **Equation 2.9**, we can determine the diffusion length (L_{D}) and therefore the spatial resolution of the THz modulator [105]. The diffusion length is defined as

$$L_{\text{D}} = \sqrt{D\tau_{\text{bulk}}}, \tag{2.17}$$

which implies that for any given excitation location, there will be a diffusion of carriers within a radius of L_{D} from that location. This results in a spatial resolution of $\Delta(x) \approx 2L_{\text{D}}$.

In practice, minimising non-radiative mechanisms, such as Auger and SRH recombination, is often a priority in device design to extend the bulk carrier lifetime and improve overall device performance. Improving Auger recombination involves typically decreasing the density of charge carriers by decreasing the excitation intensity, which leads to less modulation. Therefore as seen in **Equation 2.17**, this means there is an inherent trade-off between better modulation performance, and better spatial resolution to be aware of during the design of a spatial THz modulator.

2.4.8 Continuity Equation

The continuity equation provides a comprehensive description of the temporal and spatial evolution of carrier densities within the semiconductor. It is derived from the conservation of charge and accounts for both carrier generation (**Equations 2.6**) and recombination processes (**Equations 2.11–2.15**), as well as carrier transport through drift and diffusion (**Equations 2.7–2.10**). For electrons and holes, the continuity equation can be expressed respectively as

$$\frac{\delta N_{\mathrm{e}}}{\delta t} = G - R_{\mathrm{bulk}} - R_{\mathrm{Surf}} + \nabla \cdot \mathbf{J}_{\mathrm{e}}. \tag{2.18}$$

This equation combines all the carrier dynamics equations of generation (G), bulk and surface recombination ($R_{\mathrm{bulk}}, R_{\mathrm{Surf}}$), and diffusion (specifically $\nabla \cdot \mathbf{J}_{\mathrm{e}}$ is used to compute the divergence of the current density vector) to calculate the changing electron carrier density within the wafer during a photoexcitation event [85].

Figure 2.5 is a simulation of **Equation 2.18**, with an emphasis on demonstrating the effects of altering excitation intensity from **Equation 2.6**. At depth 0 mm is where the excitation is taking place on the wafer, for which there is an exponential decay into the wafer back to the intrinsic state. For higher intensities, there is a correspondingly higher magnitude of generated charge carriers.

Note the logarithmic scale on the generated carrier densities. This scale suggests that the majority of carriers (90%) generated by the excitation process occur within the first 10 or so microns of the wafer. While excitation does occur deeper into the sample, it should be evident how influential the surface layers of the wafer are in the effectiveness of the modulator design.

2.5 Fresnel Transfer Matrix Equations

The Fresnel transfer matrix equations provide an effective framework for analysing the propagation of electromagnetic waves through stratified media. These equations are pivotal in understanding how THz interacts with different layers of silicon.

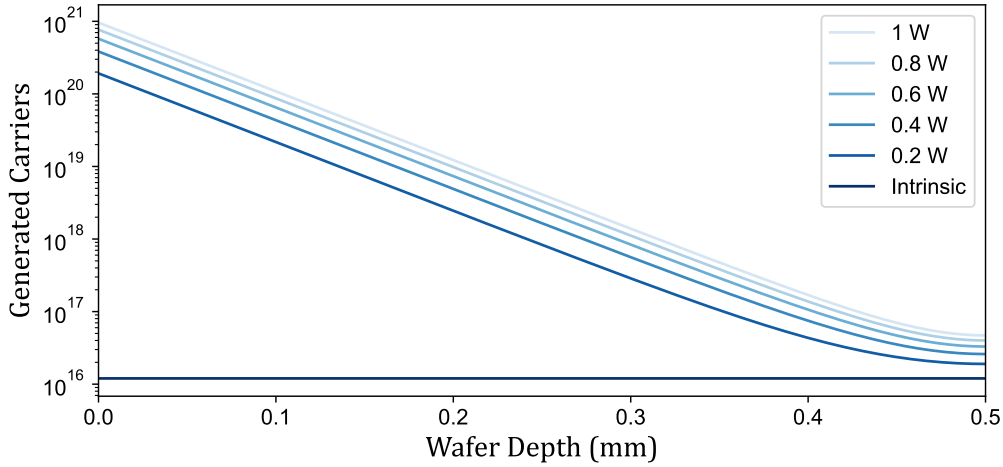

Figure 2.5: Generated charge carriers against depth into a photoexcited silicon wafer showing the unexcited carrier count (intrinsic), compared to the effects of altering excitation intensities.

By modelling the interfaces and the propagation within each layer of a silicon wafer (see **Figure 2.7**), applying Fresnel transfer matrices then enable precise calculations of reflection, transmission, and absorption coefficients.

2.5.1 Complex Refractive Index

Beginning by examining silicon's refractive index which can be established from the complex permittivity $\tilde{\epsilon}(\omega) = \epsilon_{\mathrm{Re}}(\omega) + i\epsilon_{\mathrm{Im}}(\omega)$ where ϵ_{Re} and ϵ_{Im} are the real and imaginary terms respectively according to the Kramers-Kronig relation [97]. From the Fresnel formula in which we attain $\tilde{n}^2 = \tilde{\epsilon}(\omega)$, we arrive at $\tilde{n}(\omega) = n_{\mathrm{Re}}(\omega) + in_{\mathrm{Im}}(\omega)$ where

$$n_{\mathrm{Re}}(\omega) = \sqrt{\frac{\epsilon_{\mathrm{Re}}(\omega) + \sqrt{\epsilon_{\mathrm{Re}}^2(\omega) + \epsilon_{\mathrm{Im}}^2(\omega)}}{2}}, \tag{2.19}$$

and

$$n_{\mathrm{Im}}(\omega) = \sqrt{\frac{-\epsilon_{\mathrm{Re}}(\omega) + \sqrt{\epsilon_{\mathrm{Re}}^2(\omega) + \epsilon_{\mathrm{Im}}^2(\omega)}}{2}}. \tag{2.20}$$

The outputs to **Equation 2.19** and **Equation 2.20** during excitation are crucial to the modulation phenomena we are designing the THz modulator for.

Therefore, for clarity, these functions have been simulated in **Figure 2.6** for various different levels of excitation (generated free-charge carrier concentrations) to illustrate exactly how excitation alters the properties of the wafer.

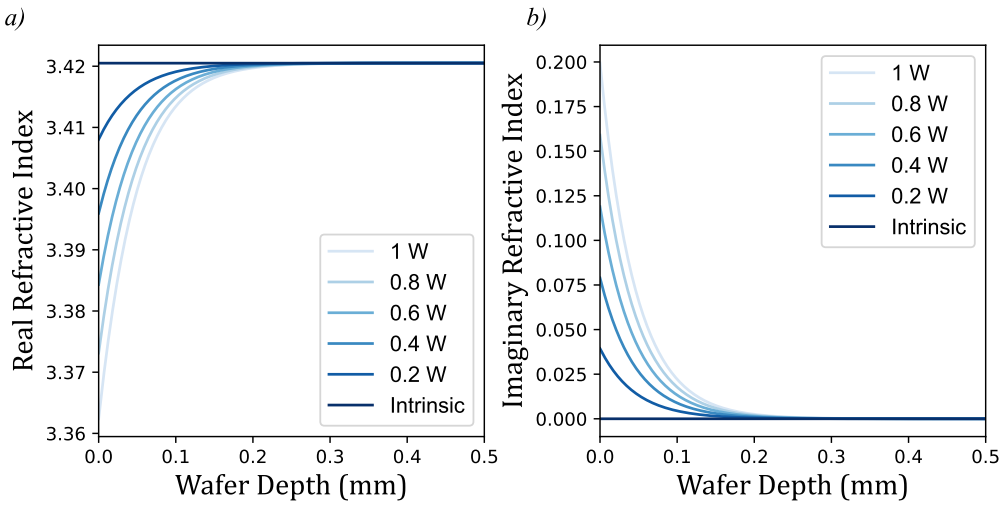

Figure 2.6: Refractive index against depth into the silicon wafer showing the real ***a)*** and imaginary ***b)*** parts of the refractive index for various levels of generated charge carriers.

At depth 0 mm is where excitation is taking place on the silicon. It is here that the largest change in refractive index is witnessed in **Figure 2.6**. The stronger the excitation, the larger the change in refractive index from the intrinsic state. The intrinsic state has a real refractive index of 3.42 and it can be seen that over the depth of the silicon, the excited silicon's refractive index is returning to this value. The imaginary component of the refractive index relates to absorption of the THz taking place across the depth of the silicon; this also depletes back to the intrinsic state.

2.5.2 Transfer Matrices

Having now attained refractive index information, we use Fresnel transfer matrix equations to achieve transmission and reflection formulae from the refractive index distribution of the wafer. By slicing the wafer of thickness h into k homogenous layers we realise a multilayered structure with slices of identical thickness δ and a

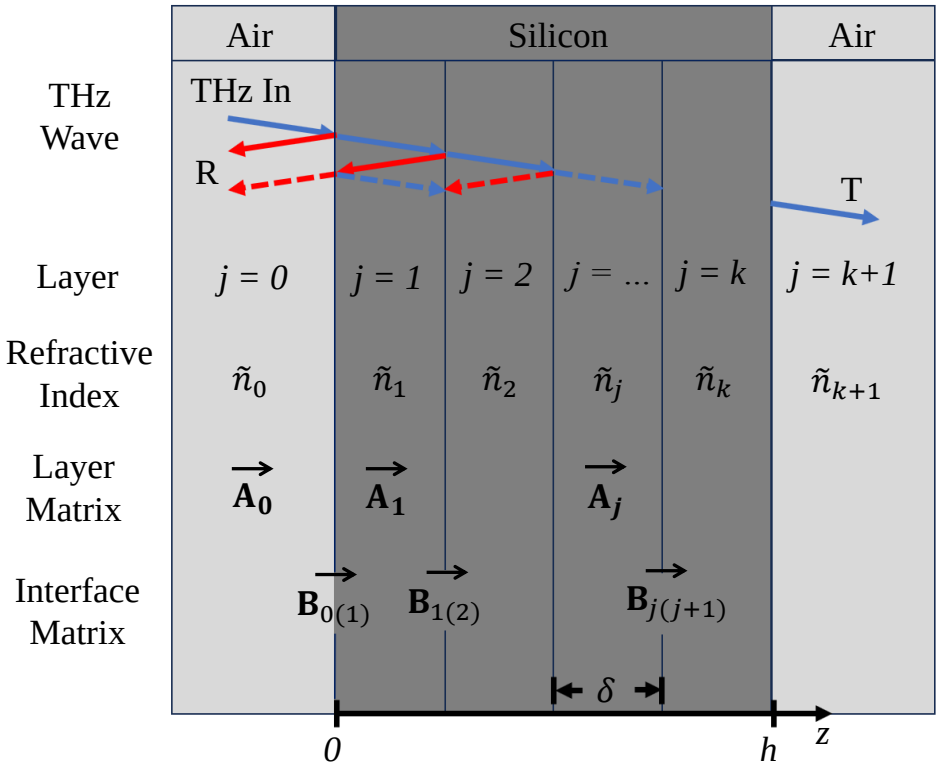

Figure 2.7: Schematic diagram for the multilayered silicon with its corresponding layer, refractive index, and matrices identified. Demonstrating the propagation of the THz through the layers resulting in a total reflection and transmission according to the layer and interface matrices across the wafer.

respective complex refractive index of $\tilde{n}_\mathrm{j} = \tilde{n}(z = j\delta)$, where z is the depth into the silicon at which the j_th layer lies as seen in **Figure 2.7**.

A key feature of this multilayered structure and its many interfaces are the wave vectors that describe the propagation of the THz waves relative to these interfaces. The general free-space wave vector equation is

$$k_0 = \frac{2\pi f_\mathrm{THz}}{c}, \tag{2.21}$$

where f_THz is the frequency of the propagating THz wave.

From this we can attain the in-plane wave vector ($k_\parallel$) which represents the component of the wave vector that lies parallel to the interfaces of the layers. It describes the propagation of the wave along the plane of the interface, which is typically the direction of the horizontal projection of the incident wave. It is

defined as

$$k_{\parallel} = k_0 \tilde{n}_0 \sin\theta_{\mathrm{THz}}, \tag{2.22}$$

where $\tilde{n}_0$ is the complex refractive index of the first layer, which is it important to note is that of air, as is the $\tilde{n}_{k+1}$ layer and are positioned on either side of the silicon wafer. θ_{THz} is the angle at which the THz radiation is incident on the wafer; usually this is 0 during normal operation.

Additionally, the out-of-plane wave vector ($k_{\perp}$) can be derived which represents the component of the wave vector that is perpendicular to the interfaces. It describes the propagation of the wave through the thickness of the layers, which is typically the direction normal to the interface and is defined as

$$k_{\perp} = \sqrt{\tilde{n}^2 k_0^2 - k_{\parallel}^2}. \tag{2.23}$$

To ensure the precision of the simulation, the number of layers (k) is chosen such that δ is smaller than the wavelength of incident THz. With these parameters set, the propagation matrix $\mathbf{A}_j$ for the wave traversing the j_{th} layer is expressed:

$$\mathbf{A}_j = \begin{pmatrix} e^{i\phi_j} & 0 \\ 0 & e^{-i\phi_j} \end{pmatrix}, \tag{2.24}$$

where $\phi_j = 2\pi\delta\tilde{n}_j f_{\mathrm{THz}}/c$ represents the phase shift exhibited on the traversing THz wave of frequency f_{THz}. Additionally, the propagation matrix $\mathbf{B}_{j(j+1)}$ for the j_{th} and the $(j+1)_{\mathrm{th}}$ layer interface can now be expressed:

$$\mathbf{B}_{j(j+1)} = \frac{1}{t_{j(j+1)}} \begin{pmatrix} 1 & r_{j(j+1)} \\ r_{j(j+1)} & 1 \end{pmatrix}, \tag{2.25}$$

where $t_{j(j+1)} = \frac{2\tilde{n}_j}{\tilde{n}_{(j+1)}+\tilde{n}_j}$ and $r_{j(j+1)} = \frac{\tilde{n}_{(j+1)}-\tilde{n}_j}{\tilde{n}_{(j+1)}+\tilde{n}_j}$ are the Fresnel transmission and reflection coefficients respectively [97].

Using these matrices, the transfer matrix equation can be constructed as

$$\mathbf{M} = \prod_{j=1}^{k} \mathbf{A}_j \mathbf{B}_{j(j+1)} = \begin{pmatrix} \mathbf{M}_{00} & \mathbf{M}_{01} \\ \mathbf{M}_{10} & \mathbf{M}_{11} \end{pmatrix}, \tag{2.26}$$

where the two propagation matrices are repeatedly multiplied over the entire thickness of the wafer between $j = 1$ and k. The relation between waves incident to the wafer with the exiting waves is given by $\binom{1}{r} = \mathbf{M}\binom{t}{0}$, where r and t are the reflection and transmission coefficients respectively [106]. When rearranged, the combination of these concepts result in definition for wafer transmittivity ($Trans$) as follows:

$$Trans = \left| \frac{1}{\mathbf{M}_{00}} \right|^2 . \tag{2.27}$$

A key point to note is from **Equation 2.2** the term ω_{THz} used in the derivation of transmittivity from **Equation 2.27** means that the transmittivity value only holds for that specific incident THz radiation. However, by scanning a range of incident THz frequencies and therefore a range of ω_{THz} values it becomes possible to visualise transmittivity as a function of incident THz frequencies. This is shown in **Figure 2.8** where it now becomes apparent that etalon cavity affects are taking place in the silicon, dependent on the silicon wafer thickness. Moreover, evidence of the intended modulation affects start to become visible as the transmittivity values for excited and intrinsic example wafers are plotted together for comparison.

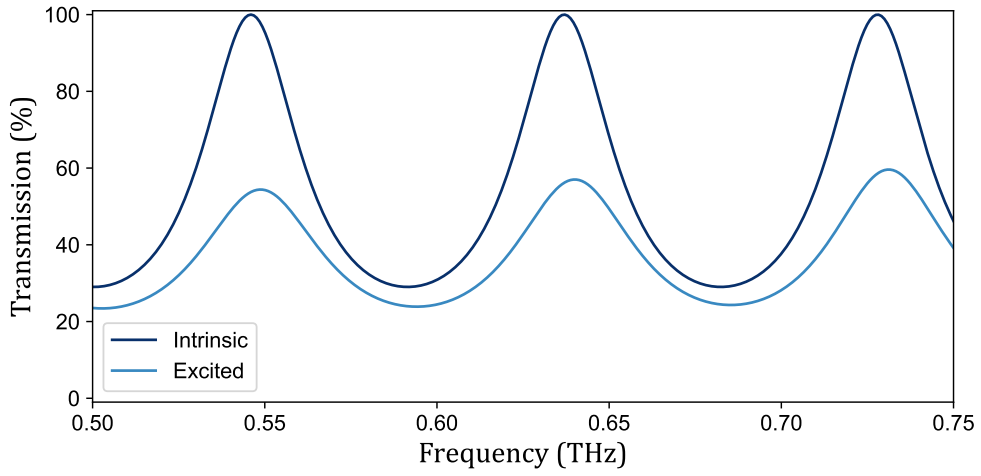

Figure 2.8: Example transmission against incident THz frequencies for both excited and intrinsic states of silicon showing etalon cavity affects and initial observations of modulation affects via excitation.

Figure 2.8 shows notable effects of thickness on transmission for both the

excited and intrinsic states. Upon closer inspection of the excited transmission, it is seen that there is an offset in apex locations. This is due to the slight change in the refractive index upon excitation inducing a further change in the free spectral range in the etalon cavity, resulting in an offset from the intrinsic state.

A common means of measuring modulator performance is via modulation depth [107]. This is a comparison between excited and non-excited transmittivity. Modulation depth (MD), defined as

$$MD = \frac{Trans_0 - Trans_{\text{ex}}}{Trans_0}, \tag{2.28}$$

where $Trans_0$ is the transmittivity of the intrinsic (non-excited) silicon wafer, and $Trans_{\text{ex}}$ is the transmittivity of the excited silicon wafer. This is usually expressed as a percentage, as shown in **Figure 2.9** which is the modulation depth produced from the transmissions seen in **Figure 2.8**.

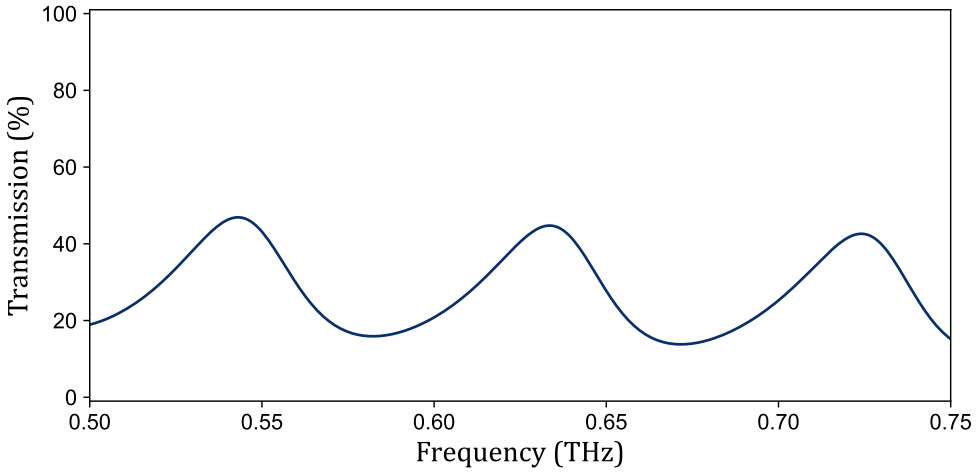

Figure 2.9: Simulation of modulation depth of a silicon wafer against incident THz frequencies demonstrating etalon affects induced upon the modulation depth.

In conclusion, through the combination of light and matter theory and semiconductor physics, it is possible to examine the fundamental phenomena that affect the modulation processes involved in the modulator described in this work. By finally simulating the modulation depth and therefore the performance of a THz modulator, parameters which impact this metric can be determined and then ac-

counted for in the design of the modulator. This theory therefore acts as a guide in the upcoming results chapters where experimentation has been specifically targeted towards these performance-impacting parameters.

Chapter 3

Experimental Methods and Procedures

This chapter presents the experimental methodologies that underpin the development and validation of the THz spatial light modulator. The methods described here serve to characterise both the material system and the optical-THz setup, establishing the foundation for interpreting the device's performance in later chapters.

It begins with the integration of Focused Ion Beam (FIB) technology for precise Transmission Electron Microscopy (TEM) sample preparation, followed by advanced electron microscopy techniques—Bright Field - Transmission Electron Microscopy (BF-TEM), Scanning Transmission Electron Microscopy (STEM), Energy-Dispersive X-ray Spectroscopy (EDS), and Selected Area Electron Diffraction (SAED)—to assess the silicon wafer structure and impurity profile, as discussed in **Chapter 5**. These measurements are essential for confirming the wafer's suitability as a photoexcited modulation medium.

The chapter then outlines the implementation of optical systems including diode, Ti:Sapphire, and NKTEvo supercontinuum lasers, along with THz systems for spectroscopic and imaging analysis. These systems are used to generate and evaluate spatial excitation patterns and modulation performance, with results developed in **Chapter 4** and **Chapter 6**.

3.1 Focused Ion Beam

Focused Ion Beam (FIB) systems, based on gallium ion sources, have become indispensable for high-precision micromachining and sample preparation [108, 109]. Their integration with Scanning Electron Microscopes (SEM) has further enabled simultaneous milling and imaging, making them ideal for site-specific Transmission Electron Microscopy (TEM) sample preparation.

Today, FIBs are widely used in materials science, nanotechnology, and failure analysis. One of its most critical applications is TEM sample preparation, where FIBs enables site-specific thinning of bulk materials to electron-transparent thickness (100 nm or less). Additionally, FIB techniques are employed in nanofabrication, including maskless lithography, and 3D prototyping [110, 111]. The ability to precisely mill, modify, and deposit materials at the nanoscale makes FIB technology a fundamental tool as shown in **Chapter 5**.

In this thesis, the thin lamellae produced are essential for directly examining lattice structure, defect density, and crystallinity, properties that influence charge carrier dynamics such as SRH and surface recombination discussed in **Section 2.4.5** and **Section 2.4.6**. Confirmation of crystal integrity ensures consistency with the assumptions used in modelling carrier mobility and recombination lifetimes. For further information on the FIB procedure and the milling performed on the Silicon wafer, refer to **Appendix A**.

3.2 Transmission Electron Microscopy

Transmission Electron Microscopy (TEM) enables atomic-scale imaging through the interaction of high-energy electrons with ultra-thin samples. Its superior resolution, stemming from the short de Broglie wavelength of electrons [112, 113], has made it a foundational tool in materials characterisation. TEM is now widely used for atomic-scale imaging in various fields. In materials science, crystallography,

grain boundaries, and defects in metals, ceramics, and polymers are examined. Nanotechnology relies on it for analysing nanoparticles, quantum dots, and 2D materials like graphene. The semiconductor industry uses TEM for failure analysis and quality control, while geosciences apply it to study minerals and meteorites. In this discourse, we shall use TEM to analyse silicon wafers to determine the presence of any defects or impurities.

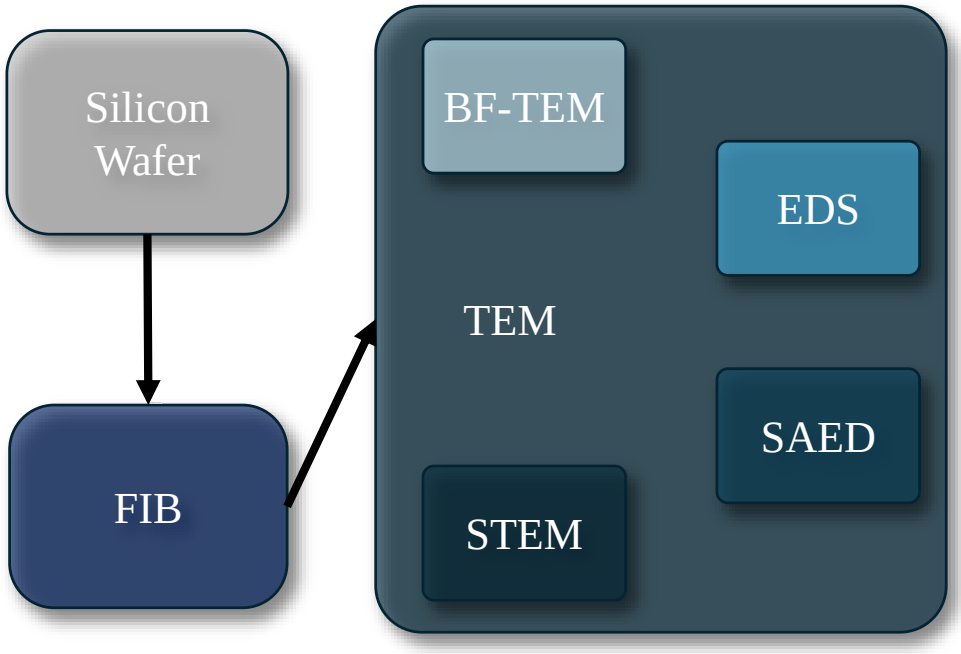

Figure 3.1: A flowchart depicting the integration of the silicon wafer into the Focused Ion Beam (FIB) milling process before implementation into the Transmission Electron Microscopy (TEM) system. The TEM system is shown to contain four subsystems, namely Bright Field - Transmission Electron Microscopy (BF-TEM), Energy-Dispersive X-ray Spectroscopy (EDS), Selected Area Electron Diffraction (SAED), and Scanning Transmission Electron Microscopy (STEM).

There are several imaging modes in TEM, each optimised for specific types of analysis as shown in **Figure 3.1**. In the following sections we shall discuss the modes used in **Chapter 5** for characterisation of a silicon wafer. Bright Field - Transmission Electron Microscopy (BF-TEM) which collects unscattered electrons, producing images where denser regions appear darker. SAED provides crystallo-

graphic information by generating diffraction patterns from the sample's atomic structure. Energy-Dispersive X-ray Spectroscopy (EDS) for elemental mapping combined with Scanning Transmission Electron Microscopy (STEM) which scans a focused electron probe across the sample, enabling high-resolution imaging. For additional information on the TEM schematics and the corresponding subsystem operations, refer to **Appendix A**.

3.2.1 Bright-Field TEM

Bright Field - Transmission Electron Microscopy (BF-TEM) [114] is the most commonly used imaging mode in transmission electron microscopy and we make use of it in **Section 5.2**. It operates by collecting the unscattered and low-angle elastically scattered electrons that pass through the specimen. The resulting image is formed based on electron transmission, where variations in sample thickness, density, and atomic composition create contrast. Thicker or denser regions absorb or scatter more electrons, appearing darker, while thinner or less dense regions transmit more electrons, appearing brighter.

The fundamental contrast mechanism in this mode is mass-thickness contrast, where heavier elements and thicker regions attenuate more electrons, leading to greater image contrast. Another key factor is diffraction contrast, particularly in crystalline materials, where differences in lattice orientation cause variations in electron scattering, affecting the image intensity. This makes BF-TEM particularly effective for analysing grain boundaries, defects, and dislocations in materials.

To optimise imaging, BF-TEM typically uses an objective aperture to block high-angle scattered electrons, enhancing contrast while reducing background noise. The quality of the image depends on parameters such as accelerating voltage, focus, and sample thickness. High-voltage TEM (above 200 kV) allows for imaging thicker samples but may reduce contrast due to increased electron penetration.

3.2.2 Energy Dispersive X-ray Spectroscopy

Energy-Dispersive X-ray Spectroscopy (EDS) [115] is an analytical technique commonly integrated with TEM to provide elemental composition analysis of a specimen as described in **Section 5.2**. It operates by detecting characteristic X-rays emitted from a sample when it is bombarded with high-energy electrons as shown in **Appendix A**. These X-rays have element-specific energy levels, allowing for qualitative and quantitative elemental identification.

The technique can be applied in two modes: point analysis, where the beam is focused on a small region to determine its composition, and elemental mapping, which generates a spatial distribution of elements across the sample. Although EDS is highly effective for elemental analysis, it has limitations, such as low sensitivity to light elements ($Z < 10$) and the need for thin samples to avoid X-ray absorption. Additionally, spatial resolution is limited by the interaction volume of electrons in the sample. However, when combined with STEM, EDS can achieve nanoscale spatial resolution, making it a powerful tool for analysis in TEM.

3.2.3 Selected Area Electron Diffraction

Selected Area Electron Diffraction (SAED) [116] is a technique used to analyse the crystalline structure, phase identification, and orientation of materials at the nanoscale as seen in **Section 5.2**. It is based on the wave-particle duality of electrons, where a highly energetic electron beam interacts with a crystalline specimen, producing a diffraction pattern that reveals the material's structural properties.

In SAED, a parallel electron beam is directed at a specific region of the sample, typically selected using a selected area aperture in the image plane of the objective lens. This aperture isolates a defined area, ensuring that the resulting diffraction pattern originates from a single phase or grain. When the electrons pass through the periodic atomic lattice of a crystalline material, they undergo elastic scattering and interfere constructively at Bragg's angle, forming a distinct diffraction pattern

of bright spots. These spots correspond to reciprocal lattice points, providing direct information about the sample's lattice planes.

SAED is widely used in materials science, nanotechnology, and metallurgy to determine crystal structure, lattice spacing, and grain orientation. It is also valuable for detecting defects such as twinning, stacking faults, and phase transformations. Additionally, polycrystalline or amorphous materials produce diffuse rings rather than discrete spots making it efficient at determining sample crystallinity. However, SAED has limitations, including low spatial resolution due to the relatively large selected area (typically 200–1000 nm), making it unsuitable for very fine structural analysis.

Crystallographic confirmation via SAED ensures that no significant lattice distortion alters the effective mass values of electrons and holes assumed in **Equation 2.2** and **Equation 2.3**. Likewise, elemental analysis via EDS validates the absence of dopants or contaminants, which would otherwise affect free carrier concentration in all recombination and transport models discussed in **Chapter 2**.

3.2.4 Scanning Transmission Electron Microscopy

Scanning Transmission Electron Microscopy (STEM) [117] is an advanced imaging mode that combines high-resolution imaging with EDS, as performed in **Section 5.2**. Unlike conventional TEM, which uses a broad, parallel electron beam, STEM employs a highly focused, nanometre-scale electron probe that is raster-scanned across the specimen, collecting signals at each point to form an image.

The core advantage of STEM lies in its flexibility in contrast mechanisms. By using different detectors, multiple imaging modes can be achieved. In this work we use Bright-Field STEM which records unscattered or low-angle scattered electrons, generating contrast similar to conventional BF-TEM. When combined with EDS, STEM enables spatially resolved elemental analysis of samples.

Despite its advantages, STEM has limitations, including higher electron dose

requirements, which can cause beam damage in sensitive materials. Additionally, achieving atomic resolution requires careful aberration correction and high stability in the electron column. Nevertheless, STEM remains one of the most powerful tools in modern electron microscopy, offering unparalleled insights into the structure and composition of materials at the atomic scale.

3.3 Optical Systems

In order to achieve spatial modulation of the THz wave via photoexcited silicon, several laser sources were employed, each selected for its specific optical characteristics and experimental utility. The choice of wavelength impacts the absorption depth in silicon and therefore the spatial profile of carrier generation, which directly influences the modulation depth. Lasers were selected to allow coverage of a broad spectral range (405–920 nm) in order to investigate wavelength-dependent effects on excitation efficiency. Additionally, systems were chosen based on their compatibility with the DMD projection optics, power stability, beam collimation, and temporal modulation capabilities.

Specifically, the optical systems in this work can be split into three distinct sections where the lasers employed accommodate different experimental requirements: high-power continuous-wave diode lasers at 405, 450, and 637 nm for silicon photoexcitation studies in **Chapter 5**, a Ti:Sapphire laser for higher wavelength silicon photoexcitation also in **Chapter 5**, and a NKTEvo SuperK super continuum laser for characterisation in **Chapter 4**.

The diode lasers provide stable and high-intensity continuous-wave illumination with power outputs up to 1.6 W, requiring a custom thermoelectrically cooled mounting system to maintain operational stability. The Ti:Sapphire laser, featuring a bowtie cavity, enables tunable photoexcitation from 650 to 1100 nm. The NKTEvo SuperK supercontinuum laser extends spectral capabilities even further,

generating a broadband output spanning from 400 to 2400 nm via non-linear interactions in photonic crystal fibers.

Each laser system is integrated with optical components such as collimation optics, fiber coupling interfaces, and acousto-optic tunable filters to ensure controlled beam delivery and wavelength selection. Together, these systems provide the necessary flexibility and precision required for optical characterisation experiments.

3.3.1 405, 450, and 637 nm Lasers

These diode lasers were chosen for their fixed and stable wavelengths, each within a region of the spectrum where silicon exhibits strong absorption. The 405 nm laser, in particular, has a short absorption length, enabling shallow and high-density excitation, making it well-suited for fine-resolution patterning. The 450 and 637 nm lasers were employed to probe modulation depth dependence on longer penetration depths and to validate the modelling predictions for wavelength-selective excitation.

To implement these photoexcitation conditions in the experiments described in **Section 5.4**, a variety of high-powered continuous wave laser diodes were used, specifically the L405G1 diode (405 nm), the L450P1600MM diode (450 nm), and the L637G1 diode (637 nm). These diodes produced 1 W, 1.6 W, and 1.2 W of power respectively. To achieve this, a custom-built cooling mount had to be developed, designed for compatibility with all three diode models while ensuring adequate collimation capability.

Constructed from aluminium, this mount provided efficient heat dissipation and structural integrity. It was actively cooled using a TECF2S thermoelectric cooler, ensuring precise thermal control and stable diode operation. Two graphene Kryosheets [118] were integrated between the TECF2S, aluminium mount, and brace to enhance thermal conductivity, significantly improving heat transfer efficiency and maintaining consistent diode performance under prolonged high-power

operation. A key advantage of the Kryosheet over traditional thermal paste is its longevity. Unlike paste, which dries out and requires periodic replacement, the Kryosheet remains stable over time. This eliminates the need for routine disassembly to reapply thermal paste, avoiding the subsequent realignment of the laser system. Additional information can be found in **Appendix C**.

To ensure accurate beam delivery and optimal excitation conditions, the mount was engineered to be compatible with the LTN330-A adjustable collimation tube, enabling precise focusing and alignment of the laser beams onto the silicon sample. The diode current was supplied via an SR9HF-DB9 cable which was compatible with all three chosen diodes due to matching G pin configurations. The 'HF' model cable was used to supply the higher 7.5 V output required for the high power diodes. It should be noted that the S8060-4 socket that comes with the cable is not a perfect fit for the 5.6 mm diodes we use but it is functional. The LDC220C current driver was used to supply power to the diodes due to its 2 A maximum current output which matches the requirements for all three diodes.

The chosen wavelengths (405 - 637 nm) correspond to photon energies significantly above silicon's 1.12 eV band gap (**Section 2.2.1**), ensuring efficient carrier generation through direct interband transitions. These wavelengths result in depth-dependent carrier profiles governed by Beer–Lambert absorption, as modelled in **Equation 2.5**. These optical penetration depths and resulting carrier distributions directly inform the simulations shown previously in **Figure 2.5**, where excitation intensity and carrier density determine the refractive index profile relevant for THz interaction.

3.3.2 Ti:Sapphire Laser

The Ti:Sapphire laser was selected for its tunability and high peak power when mode-locked. It allowed excitation at 780 nm to 920 nm, which lies near the edge of efficient absorption for silicon. This laser was used primarily for assessing

long-wavelength excitation limits especially near the bandgap limit of silicon for comparison of experiment to theoretical expectations.

The Ti:Sapphire (titanium-doped sapphire) laser was developed in the early 1980s by Peter Moulton at MIT's Lincoln Laboratory, marking a transformative advancement in ultrafast optics and spectroscopy [119]. The laser utilises a titanium-doped sapphire crystal, notable for its exceptionally broad tunability range from approximately 650 to 1100 nm. This feature, combined with its efficient operational characteristics, has cemented its role as a crucial instrument in numerous fields, including ultrafast spectroscopy, microscopy, and super continuum generation, as used in **Section 5.4**.

However, despite their broad adoption, Ti:Sapphire lasers present certain operational challenges and limitations. They require intense optical pumping, typically achieved via frequency-doubled neodymium-doped yttrium aluminium garnet lasers or diode-pumped solid-state lasers. This requirement adds complexity, increases system costs, and necessitates precise cavity alignment, demanding specialised training and frequent maintenance. Thermal lensing within the gain medium is another critical challenge, as it adversely affects beam quality, pulse stability, and overall laser performance. Furthermore, the relatively large physical footprint and higher operational costs restrict the use of Ti:Sapphire lasers primarily to specialised research laboratories. For additional information on the internal operating principles of the Ti:Sapphire system used in this work, refer to **Appendix B**.

Figure 3.2 shows a range of recorded power outputs from the Ti:Sapphire laser across a range of operating wavelengths. The power outputs correspond to the internal system settings for the pump laser of the Ti:Sapphire. With an increasing pump laser power there is a corresponding increasing output power across all operating wavelengths with some occasional variations towards the higher operating wavelengths. These power outputs and variations will be discussed later in **Chapter 5**.

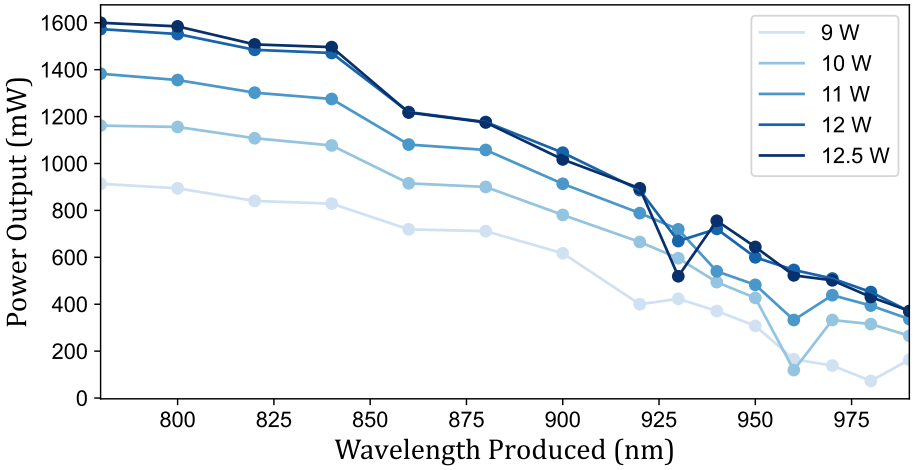

Figure 3.2: Experimentally attained power readings from the Ti:Sapphire laser as it scans across a range of emission wavelengths from 780 to 980 nm.

3.3.3 NKTEvo SuperK Laser

The SuperK Supercontinuum source was employed to provide a flexible and broadband source for characterising the performance and capabilities of the chosen DMD component. This source is capable of scanning across the visible and near-infrared range enabling the exploration of spectral regimes beyond the fixed diode lasers mentioned previously.

The NKTEvo SuperK Super continuum laser is a versatile broadband light source spanning wavelengths from 400 nm to 2400 nm [120]. This makes it suitable for applications in spectroscopy, microscopy, and various photonic experiments such as testing the illumination characteristics of a Digital Micromirror Device (DMD) as we perform in **Section 4.4**. It operates with configurable output power levels ranging from 100 mW up to 10 W, and repetition rates between 20 MHz and 320 MHz, allowing for tailored performance to specific experimental needs. For additional information on the internal operation of the NKTEvo SuperK laser and its surrounding components, refer to **Appendix B**.

Figure 3.3 depicts the emission spectra of the NKTEvo SuperK laser during an emission run between 400 and 650 nm. Multiple of such runs were completed to

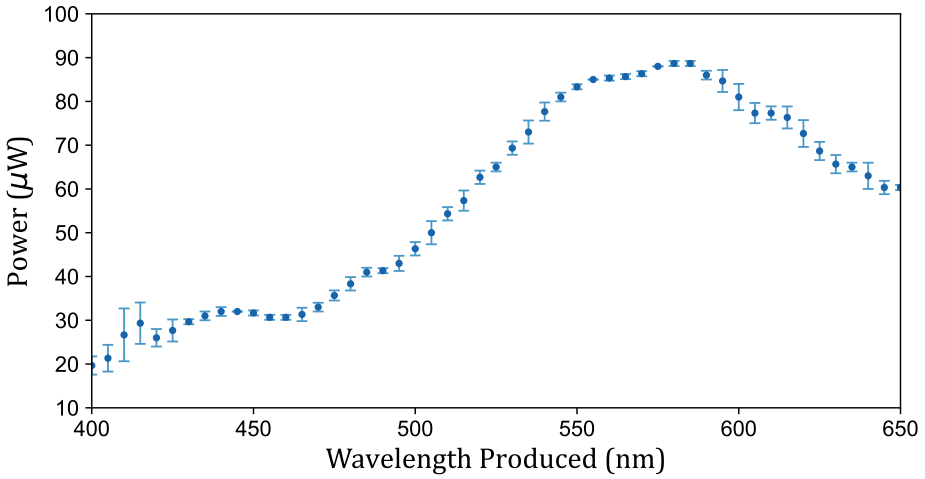

Figure 3.3: Experimentally attained power readings from the NKTEvo SuperK laser as it scans across a range of emission wavelengths from 400 to 650 nm.

produce the error bars present in the figure. While the NKTEvo laser is capable of up to 10 W of power in total, at any one specific frequency the power output is much lower. This enables the DMD surface coatings to adequately cope with the power levels presented during tests described in **Chapter 4**.

3.4 Terahertz Systems

In this work, two complementary THz systems were employed: the Terascan system for high-resolution spectroscopic analysis (**Chapter 5**) and a Rydberg atom-based THz imager for spatial mapping of THz fields (**Chapter 6**).

The Terascan system utilises a photomixing technique, in which two frequency stabilised diode lasers generate a tunable continuous wave THz signal. This heterodyne system achieves sub-megahertz level spectral resolution and allows precise phase-sensitive detection of THz interactions with silicon-based samples. Digital signal processing is used to extract the envelope function of the detected intermediate frequency signal, enabling accurate spectral reconstruction.

For spatially resolved THz field detection, a high-resolution THz imager based

on Rydberg atoms in a quartz vapour cell was used. Caesium atoms were excited to highly sensitive Rydberg states via a three-step laser excitation process. Incident THz fields induced transitions between Rydberg states, modifying the atomic absorption profile and altering the fluorescence intensity of the vapour. An Andor camera captured these fluorescence variations, providing high-resolution THz field imaging. These combined approaches enabled both spectroscopic and spatial analysis of modulated THz fields, crucial for evaluating the design parameters in the modulator.

3.4.1 Terascan System

The schematic for the Toptica Terascan 1550 system is shown in **Figure 3.4** containing a high-precision THz spectroscopy platform based on a photomixing scheme, enabling continuous-wave THz generation and detection with high spectral resolution [121]. These features make it a valuable tool for examining silicon's spectroscopic characteristics as described in **Section 5.3**. It operates by using two frequency-stabilised distributed feedback diode lasers, each emitting at slightly different wavelengths around 1550 nm. These laser beams are combined and coupled into a photomixer, where their interference produces an optical beat frequency corresponding to the difference between the two laser frequencies. An AC bias modulates the photocurrent before passing it to a photoconductive antenna emitter.

The system employs a heterodyne detection scheme [122], where a second photoconductive antenna, identical to the emitter, is used as the detector. The generated THz wave interacts with the sample before being directed to the detector, where it mixes with the local oscillator signal, which is a fraction of the original optical beat frequency. This mixing process produces an intermediate frequency signal, which carries amplitude and phase information about the THz wave after interaction with the sample. The intermediate signal is typically in the megahertz range and is extracted using a lock-in amplifier, which significantly improves the

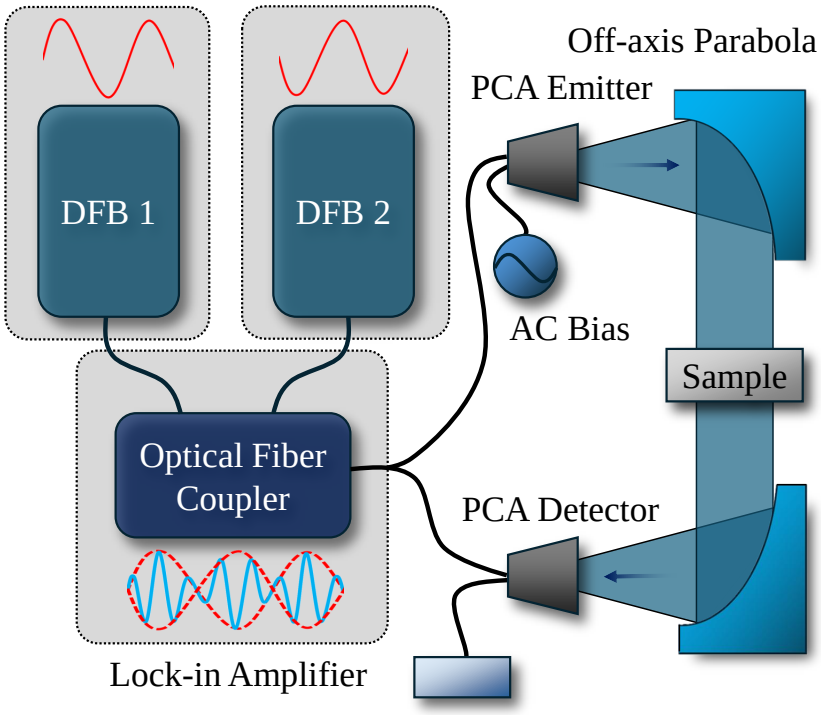

Figure 3.4: A schematic of the Toptica Terascan 1550 system. Two Distributed Feedback lasers (DFBs) with slightly different wavelengths around 1550 nm are coupled into an optical fiber coupler for photomixing. The difference between the two DFB signals is outputted to two Photoconductive Antennas (PCAs), one which acts as an emitter and one as a receiver in a hetrodyne scheme. The AC bias modulates the photocurrent at a fixed frequency (39.67 kHz). The lock-in amplifier then extracts the modulated signal by synchronising with this frequency, filtering out noise and enhancing sensitivity.

signal-to-noise ratio by selectively amplifying the modulated signal while suppressing noise.

To accurately retrieve the THz signal, the envelope function [122] of the detected intermediate frequency signal must be extracted. The envelope function represents the slowly varying amplitude of the intermediate signal, which is crucial for demodulating and extracting the underlying THz spectral features. The system software uses digital signal processing techniques to analyse this envelope, enabling precise reconstruction of the amplitude and phase response of the sample across the scanned frequency range. By carefully controlling the laser frequency difference and stabilising the optical path, the system achieves sub-megahertz-level spectral

resolution.

The scan range from 100 GHz to 1.2 THz overlaps with the predicted plasma frequency transitions for optically excited silicon as derived in **Equation 2.3**. This allows experimental testing of the dielectric switching behaviour across the modulated reflective–transparent boundary shown previously in **Figure 2.9**.

3.4.2 Terahertz Imager

In **Section 6.2**, we evaluate the capabilities of the designed THz modulator using a high-resolution THz imaging system [123]. This system enables accurate spatial mapping of THz fields with diffraction limited resolution through a combination of frequency-stabilised laser sources, tunable THz generation, and controlled attenuation.

The imager operates via a laser-based excitation scheme that prepares Rydberg atoms in an atomic quartz vapour cell. The atomic system utilises caesium (^{133}Cs), a stable isotope, contained within a quartz vapour cell that provides optimal optical access for laser excitation. The excitation scheme, depicted in **Figure 3.5** ***a)***, consists of a three-step laser process: a probe laser (Toptica DL100) at 852 nm excites atoms from the $6S_{1/2}$ to $6P_{3/2}$ state. A coupling laser (Toptica DLPro) at 1470 nm then transfers the atomic population to the $7S_{1/2}$ state, followed by excitation from a Rydberg laser (MOGLabs cateye diode) at 843 nm, which brings the vapour into a highly sensitive $14P_{3/2}$ Rydberg state. Additionally, the vapour is heated to 60°C as standard to further enhance sensitivity by increasing the atomic number density, thereby improving the interaction strength between the vapour and incident THz radiation. The full system schematic in **Figure 3.5** ***b)*** shows the probe, coupling, and Rydberg lasers all overlap inside the vapour cell which is positioned in a heating stage ready to be probed with the THz field.

The THz source employed in this system is a narrowband, continuous-wave field generated by an amplifier multiplier chain (AMC 702, Virginia Diodes Inc.),

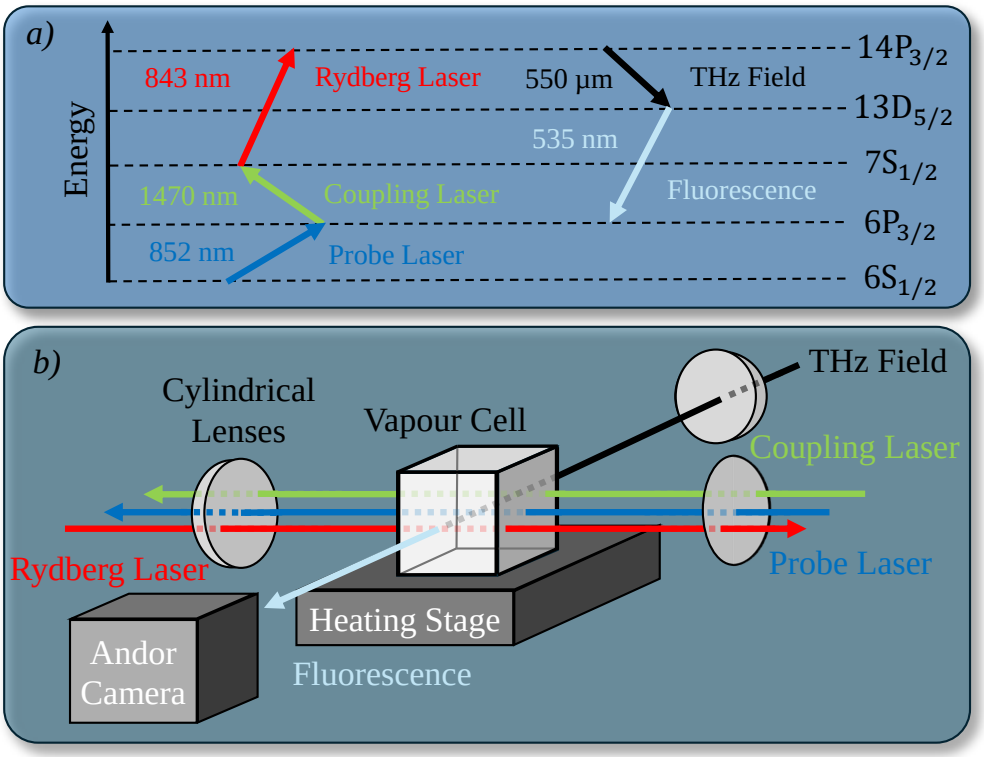

Figure 3.5: ***a)*** A diagram of the changing energy structure within the heated Caesium vapour cell when exposed to the probe, coupling, Rydberg and THz lasers. ***b)*** The THz imager schematic containing the probe (852 nm), coupling (1470 nm), Rydberg (843 nm), and THz (550 µm) lasers. The vapour cell is positioned in a heating stage with fluorescence (540 nm) directed towards an Andor iXon camera.

seeded by an HP8672A microwave signal generator. The amplifier multiplier chain utilises GaAs Schottky diodes for frequency multiplication while suppressing unwanted harmonic components. This configuration produces a high-power source with a maximum output of 4 mW, operating within a narrow tuning range (540 GHz to 560 GHz) and employing a multiplication factor of 36, optimised for imaging applications. Attenuation of the THz beam is finely controlled using a digital voltage-controlled user attenuator integrated into the THz source, enabling precise adjustments of the incident field strength.

During typical operation without THz radiation, the vapour exhibits a variety of wavelengths depending on the probabilistic decay path of the excited Rydberg atom from the $14P_{3/2}$ state back to the $6P_{3/2}$ state and then a final decay to the ground state ($6S_{1/2}$). When a THz field is applied, it induces transitions between

adjacent Rydberg states (from the $14P_{3/2}$ state to the $13D_{5/2}$), altering the energy structure of the vapour. This disruption leads to a cascade decay usually along a 535 nm pathway, which is the typical fluorescence picked up by the optical Andor camera. More details on the atomic theory underlying this process are presented in **Section 6.1**.

The net effect of this phenomenon is that the vapour spatially encodes the location of incident THz radiation based on variations in fluorescence intensity. This fluorescence is then captured by an Andor iXon Ultra 888 EMCCD camera, which has a 1024 × 1024 pixel resolution, allowing for high-resolution imaging of the designed THz modulator's field distribution and imaging characteristics. It should be noted, image contrast is ultimately modulated by the permittivity gradient generated across the silicon surface, as determined by **Equation 2.4**. The experimental setup thus probes the spatial extent of the permittivity gradient, governed by excitation geometry and diffusion length (see **Equation 2.17**).

3.5 Modulator Design

The methods and techniques discussed lay foundations to characterise both the DMD (**Chapter 4**) and silicon (**Chapter 5**) components. These components are then used in coordination with the optical systems (**Section 3.3**) and THz systems (**Section 3.4**) to form the modulator we are designing.

As discussed in **Section 1.2.2**, the modulator is formed by taking a photoexcitation source, which will be chosen from the detailed optical systems, then using that excitation source we illuminate the DMD. This allows us to spatially mask the excitation locations as the light is reflected onto the designated silicon surface. This excited surface is then probed with the chosen THz system depending on the required information, either spectroscopic or spatial in nature.

Several varieties of modulator design were prototyped in the course of this study, however the general principles discussed in **Chapter 2** remained resolute.

The general design followed a schematic shown in **Figure 3.6** where there are three main components, the excitation diode, the DMD spatial masking device, and the silicon interface.

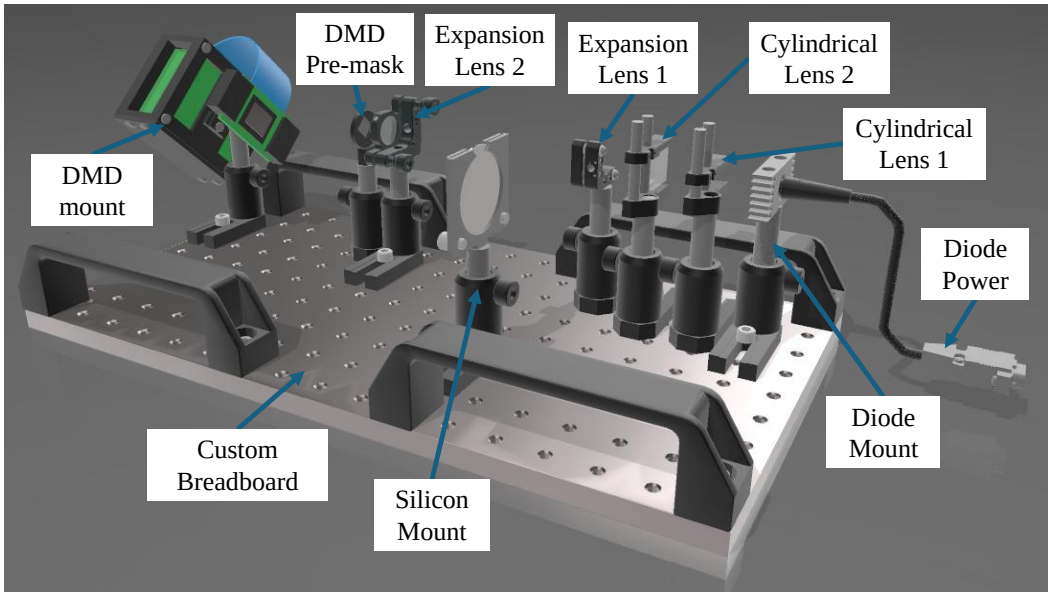

Figure 3.6: A 3D model of the entire spatial THz modulator design consisting of the custom breadboard to mount all components, the custom DMD mount and Vialux V7000 DMD, a pair of expansion lenses, a pair of cylindrical lenses, a DMD pre-mask, a testing mount for the diode, and the silicon mount containing the silicon wafer.

The DMD characterisation is discussed in depth in **Chapter 4** however some additional detailing will be discussed shortly. Similarly, the silicon interface which is arguably core of the modulator is discussed in depth in **Chapter 5**.

The excitation system consists of a pair of cylindrical lenses used to manipulate the elliptical beam produced by the diodes held within the thermal cooling mount. The manipulation varies depending on the diode in question, thus a variety of cylindrical lenses are used to achieve beam circularities between 85 and 92%. These beam circularities were measured experimentally with typical knife-edging techniques to confirm the theoretical design was performing as anticipated.

Once a circular beam was achieved, it has to be expanded to effectively fill the DMD array. This is achieved with a corresponding pair of expansion lenses used in a Galilean scheme. This scheme was used to ensure the high power radiation

does not cause the air to arc when the modulator is in operation at high optical excitation intensities. A variety of expansion lenses were chosen in correspondence with the variety of cylindrical lenses in use. Again, typical knife-edging techniques were used to ensure the theoretical expectations of the beam expansion were being achieved.

Finally, now that the beam is circular and expanded up to the dimensions of the DMD array, a precaution is placed into the system. This precaution is the DMD pre-masking which is an optical mask designed to exactly match the dimensions of the active DMD array. This ensures that light from the excitation source is only incident upon the active array and not the surrounding area. This precaution is taken due to the known limits of the DMD whereby there is an upper thermal limit under which the DMD operation is nominal. Any heating to the non-active surrounding section of the array will lead to additional heating of the device and could potentially lead to unpredictable behaviour over time.

Now the excitation section of the design is completed effectively, ensuring consistent and reliable optical radiation production onto the active DMD array surface. The DMD is then positioned perpendicular to the incident light such that the 'on' state of the mirrors leads to the high intensity radiation being directed towards the silicon mount. Notably, no imaging optics, such as a lens or re-imaging relay, are employed between the DMD and the wafer. Instead, the system relies on free-space propagation, whereby the patterned light reflected from the DMD is incident directly onto the wafer. This architecture was chosen for experimental simplicity and due to space constraints within the pre-existing imaging setup. However, it carries important consequences for image fidelity and system performance that merit detailed discussion.

In a conventional imaging system, relay optics are used to form a one-to-one image of the DMD mask at the desired target plane, preserving spatial features and minimising blurring or distortion. In the absence of such optics, the projected DMD pattern undergoes free-space diffraction, which inevitably causes high spatial

frequencies (i.e. fine features) to spread and blur before reaching the silicon. This prevents the formation of a sharply defined optical image on the wafer, particularly for patterns involving abrupt transitions or closely spaced elements. Given that the DMD mirrors are spaced at approximately 13.7 µm and the working distances are on the order of several centimetres, diffraction effects become highly significant, imposing a natural resolution limit independent of the modulator's semiconductor response.

Additional distortion arises from the angular geometry of the DMD itself. The micromirrors are operated with a mechanical tilt of ±12°, such that the 'on' state directs light orthogonally out of the DMD plane. However, in a free-space configuration without correction optics, this angle introduces projection errors due to the fact that different parts of the DMD surface lie at different effective distances from the wafer. This angular mismatch leads to a form of optical skewing that can be partially mitigated by satisfying the Scheimpflug condition, where the DMD plane, wafer plane, and imaging axis intersect at a common line. In the current system, this condition is not strictly enforced, and as a result, slight keystone distortion and focus gradients are present across the illumination field.

These optical effects are further complicated by the challenge of alignment. To a naïve observer, the task may appear to be a simple matter of projecting a pattern onto a surface. In practice, however, aligning the divergent beam from the DMD so that its spatial structure uniformly illuminates the correct region of the silicon wafer, while maintaining optical contrast and power efficiency, proves non-trivial. Minor deviations in angle or translation of the DMD result in substantial shifts at the wafer plane due to the long propagation distance. Furthermore, the alignment must be optimised across three axes simultaneously (x, y, and z), with angular tilt (pitch/yaw) contributing to additional asymmetries in pattern shape and intensity.

Finally, it is important to emphasise that the spatial limitations observed in the THz modulation results, such as reduced resolution or contrast at high spatial frequencies, cannot be attributed solely to semiconductor physics. Carrier diffusion,

lifetime, and surface recombination undoubtedly play a role, but the absence of a well-corrected optical imaging system introduces its own limitations that must be considered alongside material effects. In future implementations, the use of an imaging lens or a 1:1 relay system could offer a sharper and more controllable excitation pattern, thereby improving the overall modulation fidelity and reducing the burden on post-hoc theoretical explanation.

In summary, while the modulator is only composed of three components (source, mask, and semiconducting wafer), the resulting underlying interactions and engineering challenges render the system far more intricate than its apparent simplicity suggests. The precise coordination required between the optical excitation, the reflective spatial masking by the DMD, and the subsequent THz probing of the excited silicon surface demands an in-depth understanding of semiconductor properties and electromagnetic theory across multiple regions of the spectrum.

The interplay of these factors, coupled with the vast array of potential setup parameters—such as the excitation intensity and wavelength, THz probing angles and frequencies, the pixel configuration and switching speed of the DMD, the dopant concentration, presence of defects, and carrier lifetime in the silicon—leads to complex, non-linear effects that are highly sensitive to even minor variations. These variations can give rise to phenomena such as interference patterns, transient carrier dynamics, and modulation depth inhomogeneities, all of which require rigorous calibration and control. Furthermore, the integration of these disparate subsystems introduces challenges in terms of thermal management and component synchronisation, making the overall system a fertile ground for both theoretical exploration and practical innovation.

3.6 Limitations and Calibrations

The design and integration of the THz spatial modulator system, while highly flexible and functionally robust, is not without sources of experimental uncertainty

and systematic limitations. To ensure the accuracy, repeatability, and interpretability of the results discussed in later chapters, a number of calibration procedures and error mitigation strategies were implemented throughout the experimental process. This section outlines the principal sources of uncertainty, the corrective steps undertaken, and the inherent constraints of the current setup.

3.6.1 Systematic Sources of Error

High-power excitation, particularly from the 405 nm and SuperK laser sources, induced localised heating on the wafer surface. This heating effect will have altered the local carrier mobility as noted previously in **Figure 2.2**. To mitigate this, excitation was delivered in controlled bursts of no more than 2 minutes with resting periods to allow thermal relaxation, and temperature stability was monitored using a SEFRAM 9833 thermal imaging camera. The thermal camera was also used to monitor the stability of the diode within its custom built cooling mount to ensure regular performance within its limitations; an example of such monitoring can be seen in **Figure 3.7**.

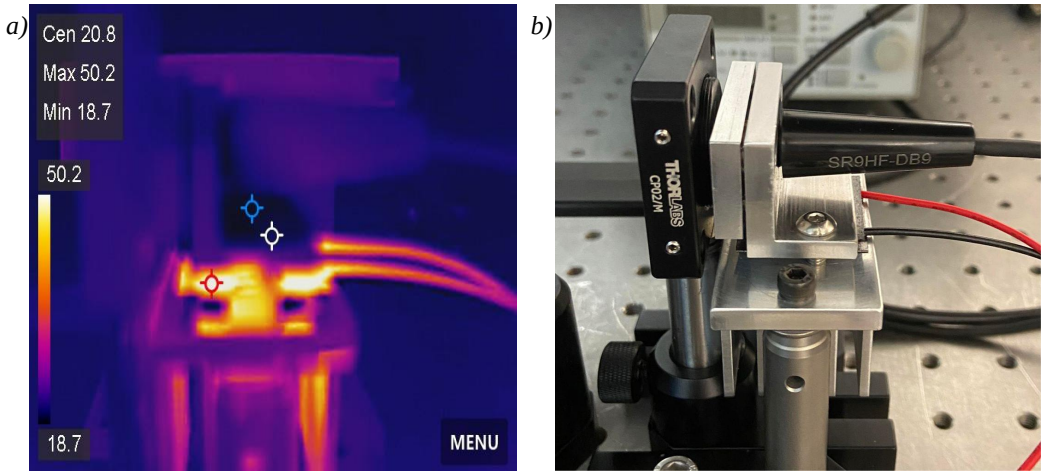

Figure 3.7: ***a)*** A thermal image of the custom laser mount during typical operation. ***b)*** The corresponding visible image of the mount during normal operation.

The mount shows a maximum temperature of 50.2°C located in the lower plate section, while the upper plate has the minimum recorded temperature of 18.7°C.

This shows the custom mount is working well within its designed limits, actively cooling the section of the mount holding the diode, while not excessively heating the dissipative region. Further details of this mount can be found in **Appendix C**.

The spatial modulation system relies on precise overlap between the projected optical excitation pattern and the silicon wafer surface. Small angular or translational misalignments can significantly affect carrier density profiles and spatial resolution. Alignment drift due to thermal expansion or stage movement was minimised using a fixed mechanical cage system, but residual misalignments were unavoidable over long durations. Regular rebuilding and alignment of the system with alternative optical lasers, described in **Section 3.3.1**, helped with correcting for these inevitable misalignments over time.

While high-resistivity float-zone silicon was chosen for its uniform electronic behaviour, inhomogeneities in doping and surface flatness across the wafer contributed to spatial variation in modulation performance. Characterisation using EDS and TEM (see **Section 5.2**) provided insight into these irregularities.

Synchronisation between the DMD projection sequence and the THz modulation depth capture window for the Terascan system was affected by delays in software triggering. While multiple runs were taken to enhance statistical accuracy, sub-millisecond discrepancies may have introduced minor inconsistencies in the acquired frame rate analysis in **Section 6.2**.

3.6.2 Statistical Considerations and Calibration Procedures

To mitigate and quantify these sources of uncertainty, various calibration strategies were routinely employed. All excitation sources were characterised and calibrated using a Thorlabs power meter, PM100D with S121C sensor, prior to each measurement session. Additionally, the Terascan photomixing system was benchmarked against the known water absorption spectrum to confirm frequency accuracy. Each spatial pattern projected by the DMD was first confirmed using a CMOS camera

placed at the silicon sample plane. This ensured that the intended modulation mask was spatially aligned and undistorted before data acquisition as well as enabling confirmation of the projected mask dimensions prior to attempted THz modulation.

Wherever feasible, data was collected across multiple experimental runs, typically 5, to validate repeatability. While environmental conditions (laboratory temperature, humidity, minor alignment differences) introduced slight variations between runs, key performance indicators such as modulation depth, frame rate, and spatial resolution were monitored for retained consistency where anticipated. Where averages or statistical distributions are presented in subsequent chapters, they reflect these multi-session acquisitions unless otherwise stated.

3.7 Conclusion

This chapter has detailed the experimental methodologies and procedures integral to this thesis. Advanced techniques, including FIB-assisted TEM sample preparation, have been rigorously described alongside a suite of electron microscopy modes such as BF-TEM, STEM, SAED, and EDS. Furthermore, the integration of sophisticated optical systems – from diode and Ti:Sapphire lasers to the NKTEvo super continuum laser – and THz imaging systems have been comprehensively outlined. These combined methods ensure precise sample analysis and reliable data acquisition. The subsequent chapter will critically examine the DMD characterisation, building upon these foundations laid here.

Chapter 4

Digital Micromirror Device Characterisation

In this chapter we aim to characterise the V7000 Vialux Digital Micromirror Device (DMD) in terms of resolution, frame rate, and power efficiency. This is done in multiple stages with resolution being captured by a DCC1545M ThorLabs camera, frame rate captured by a high speed Phantom VEO 610L camera, and power efficiency being captured by a PM100D Power-meter with S121C sensor. Characterisation of resolution and frame rate are performed by analysing intensity distributions produced by the DMD masks, while power efficiency is characterised by scanning a range of wavelengths onto the DMD and measuring reflected power. This enables us to determine the limits and capabilities of the DMD and therefore decide its suitability as the visible light modulator within the THz modulator design tested in **Chapter 6**.

4.1 Introduction

The DMD was invented in 1985 by Texas Instruments and developed for worldwide distribution by 1987 [124]. Since then, the initial design has been evolved into many different variations for numerous applications. Examples of such applications are

cinemas and office projectors [125]. The DMD utilises millions of micron-sized mirrors whose tilt can be individually controlled resulting in the ability to spatially modulate incident illumination on the DMD array. These capabilities make the technology crucial to scientific research in areas such as lithography, and medical imaging [126]. These research areas depend on the ability to precisely manipulate light spatially and dynamically which the DMD offers. Subsequently, it makes the DMD a prime component in designing a spatial THz modulator [84].

However, as with any technology, there are limitations to the DMD's capabilities. These include (but not limited to) notable characteristics such as: wavelengths the mirrors are able to effectively reflect, the overall dimensions of the array comprised of said mirrors, the maximum illumination power the device can handle, and the rate at which the mirror state can be altered. These characteristics greatly impact the device's utilisation in the THz modulator design. Specifically, the THz modulator requires high power illumination onto a semi-conductor wafer, discussed in **Chapter 5**, to effectively modulate the THz radiation, meaning the DMD must be able to handle equally high illumination. Additionally, due to limitations in laser diode wavelength choice able to excite the silicon wafer, it also means the DMD must be able to handle an appropriate wavelength. The array dimensions impact the size of semi-conductor able to be modulated, and consequently the mirror dimensions making up said array impact the resolution of the mask being cast onto the semi-conductor. Finally, the flip rate of the mirrors in the DMD limit the modulation rate of the THz modulator in **Chapter 6**.

Given the crucial nature of the DMD in a variety of other scientific areas of research, there has already been a lot of evolution of the DMD design and capabilities over the years. Alterations to its refresh rates, illumination wavelengths that can be effectively reflected, and overall array dimensions are among the range of attributes that have been evolved. Therefore, there is a decent abundance of choice when it comes to selecting an appropriate DMD to match the aforementioned requirements. Below in **Table 4.1** is the list of potential DMD options considered

for the role of spatial modulator within the THz modulator. The chosen DMD was the DLP7000 also known as the V7000 Vialux, picked due to its wide range of wavelengths, decently high thermal limit, and a reasonable resolution.

Product Name	Wavelength (nm)	Resolution (mirrors)	Limit (W/cm^2)
DLP7000	400 - 700	1024 x 768	< 11
DLP9000	400 - 700	1920 x 1080	< 11
DLP3010LC	420 - 700	1280 x 720	< 26.1
DLP300S	400 - 550	1280 x 720	< 3

Table 4.1: A list of four potential DMDs considered for use within the THz modulator in this work displaying their product name, operating wavelength range, micromirror array size (which corresponds to its resolution), and the upper thermal limit the DMD can handle.

To contextualise the performance of the DMD system, it is important to consider the various spatial scales relevant to THz modulation. The micromirror array of the DMD contains 1024×768 mirrors as seen in **Table 4.1**, each approximately 13.7 µm in size, leading to optical projection patterns with sub-wavelength features. The THz radiation used in the imager for this thesis has a wavelength of approximately 545 µm at 550 GHz, which is more than 30 times larger than the DMD pixel pitch. Consequently, each projected optical pixel is significantly smaller than the THz wavelength, meaning that the DMD resolution is not a limiting factor for THz patterning. The size of the illuminated area on the photoexcited silicon wafer, approximately 8 mm across, yields a projected mask comprising thousands of optical pixels, each capable of exciting localised regions within the silicon. However, the effective THz resolution is constrained by two independent effects: first, the diffraction-limited resolution of the THz imaging system, and second, the carrier diffusion length in the silicon, which is on the order of 10 µm. Both effects act to smooth or blur the high-resolution optical pattern, limiting the fidelity of the transferred mask at THz frequencies. This chapter therefore focuses on the characterisation of the DMD system itself, while a full analysis of its impact on THz modulation performance is presented in **Chapter 6**.

A rival to the DMD in terms of spatial modulation is the Liquid Crystal -

Spatial Light Modulator (LC-SLM). There are a couple of technical advantages that LC-SLMs have over the DMD [127]. These include the ability to modulate the phase component of incident light. While in some cases this may be an important feature, in our case of designing a modulator, it is less crucial. Additionally, the LC-SLMs can be illuminated from any angle which can be beneficial from a methodical standpoint, compared to DMDs which must be tilted to 45 degrees in plane due to the tilt mechanism of the mirrors which themselves also have a specified pitch angle when changing state. This limits illumination methods when using the DMD and impacts the overall design of the optical system. However, it is not expected to be detrimental to the effectiveness of the design. An advantage the DMD's have is the typically higher frame rate they can offer in comparison to their counterpart.

4.2 Resolution

Whenever imaging is being performed, a vital aspect of the performance is the clarity of the captured images. An impacting quality of this clarity is spatial resolution whereby having better resolution leads to sharper images [128]. When considering the design for a THz modulator, resolution is of paramount importance given the purpose of modulating the THz is for that manipulated radiation to eventually be captured and imaged. One method for quantifying the resolution specifically for the DMD is to use double slit analysis. Not only is the DMD capable of creating double slits, but the theoretical outputs of such a double slit can be accurately simulated. Resulting in a direct comparison between experiment and theory.

4.2.1 Double Slit Diffraction

While standard resolution characterisation techniques often use imaging of known test targets or Fourier optical transfer analysis [129, 130], the method employed

here adapts the classical double slit diffraction geometry to characterise the DMD's spatial modulation fidelity under conditions specific to this system. In particular, the absence of a relay imaging system between the DMD and the silicon wafer, and the requirement to assess projected pattern fidelity under divergent conditions, made traditional resolution charts impractical. Instead, slit pairs of variable spacing were used to project binary interference patterns onto a plane, enabling frequency discrimination and effective system calibration. This methodology, although developed in-house, offers a simple yet robust mechanism to extract system modulation limits.

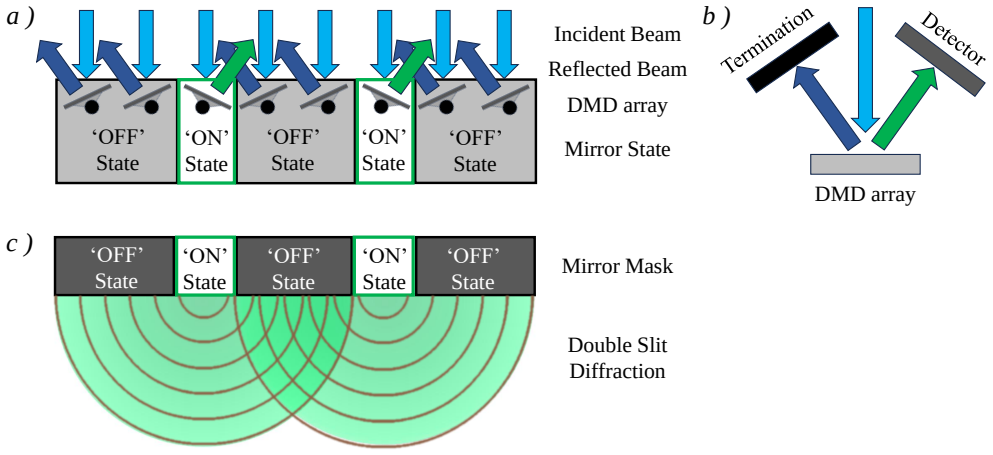

Figure 4.1: ***a)*** Schematic of the DMD array depicting how the incident beam is split into 2 reflections dependent on the state of the mirrors. ***b)*** Overview of the DMD and detector setup where on-state reflected beams are collected by the detector and off-state are terminated. ***c)*** Illustration of the double slit mask from the mirrors corresponding to the DMD's on-state reflections and the resulting double slit diffraction pattern this forms.

The DMD manipulates incident light by individually tilting its millions of micromirrors according to a preset mask. It tilts the mirrors into one of two states commonly referred to as 'off' and 'on' states seen in **Figure 4.1** ***a)***. This leads to incident light being separated into two directions where the 'on' state corresponds to the preset mask, and the 'off' state is the subtraction of this mask from the incident beam as seen in **Figure 4.1** ***b)***. This means if the mask were designed to be two thin lines set to be on while the rest of the mask is off, then it would act as a double slit in the 'on' state as the incident beam is only reflected in the 'on'

positions as depicted in **Figure 4.1** ***c)***.

Various parameters can be set when using this method. The width of each 'slit' can be adjusted relative to the mirror dimensions where the smallest possible slit would be a single mirror width. The slit gap (distance between slits) can be altered also relative to mirror dimensions where the smallest gap is a single mirror width as seen in **Figure 4.2** ***a)***. By varying these two parameters, a variety of double slit results can be collected from the DMD by imaging the corresponding intensity distributions cast from the illuminated DMD as seen in **Figure 4.2** ***b)***. These experimental results can then be compared to the theoretical expectations for validation and accuracy.

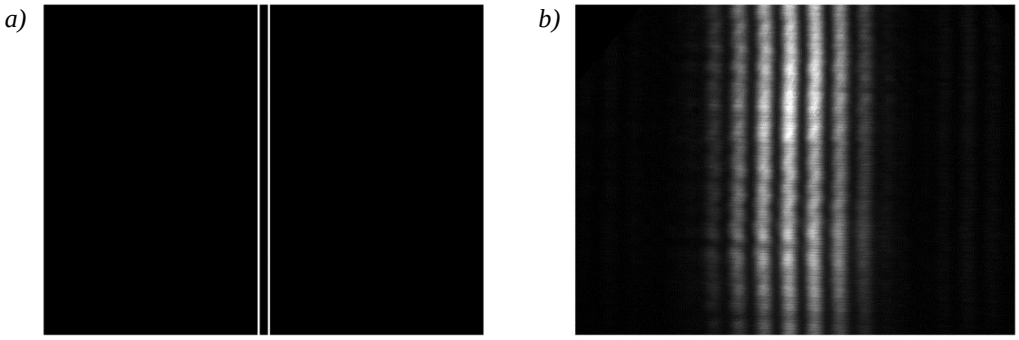

Figure 4.2: ***a)*** Image of a preset double slit mask with a slit width of 70 µm and slit gap of 260 µm. ***b)*** The resulting diffraction pattern cast from the DMD with the preset mask.

4.2.2 Diffraction Simulations

Simulations of double slit results often involve the application of mathematical principles derived from wave theory, particularly in the context of quantum mechanics. The key equation used to simulate the interference pattern in a double slit experiment is based on the principle of wave interference. This principle is encapsulated by the mathematical expression known as the double slit interference formula, which gives the resulting intensity distribution due to the interference of

waves.

The double slit interference formula is derived from the superposition principle, which states that the total amplitude at a given point is the sum of the amplitudes of individual waves. For a double slit experiment, where a wave passes through two adjacent slits, the resulting interference pattern from the slits can be derived.

Constructive interference, $dsin(\theta) = m\lambda$, where d is the distance between slits, θ is the angle from the slit to the mth order, m is an integer (such that $m = 0, \pm1, \pm2...$), and λ is the wavelength of the incident light. Now considering two point sources which are polarised similarly and with the same amplitude E we can define the expressions for their electric fields, $E_1(t) = Ecos(\omega t + \phi)$ and $E_2(t) = Ecos(\omega t)$, where ϕ is the phase difference between waves one and two denoted by E_1 and E_2 respectively. By assuming superposition between these two fields separated by a phase difference of ϕ, we attain an expression for E_p, the electric field at the point of superposition, $E_p = 2Ecos(\phi/2)$.

Rewriting the expression for E_p in terms of intensity we arrive at the expression

$$I_p = 4Icos^2(\phi/2), \tag{4.1}$$

where I_p is the intensity of the double slit interference, I is the maximum possible intensity in the system, and the phase difference ϕ is defined as

$$\phi = \frac{2\pi d}{\lambda} sin(\theta). \tag{4.2}$$

By utilising **Equation 4.1** and **Equation 4.2** we can now determine an intensity for a double slit interference pattern and simulate that result for comparison to experimental results for validation.

4.2.3 DMD Resolution Results

When comparing the experimental data to the simulation, a few steps need to be brought into consideration. The DMD, by its very nature, needs to be tilted to 45°

for it to operate safely on an optical work bench. This in turn means any masks sent to the DMD are also now tilted 45°. For the masks to have slits composed of mirrors in an orderly fashion, the mask is set with the slits occupying columns of mirrors as seen in **Figure 4.3** ***a)***. These columns are then rotated 45° by the DMD before being captured by the camera. This method results in a tilted image, but this can easily be tilted back during post-analysis.

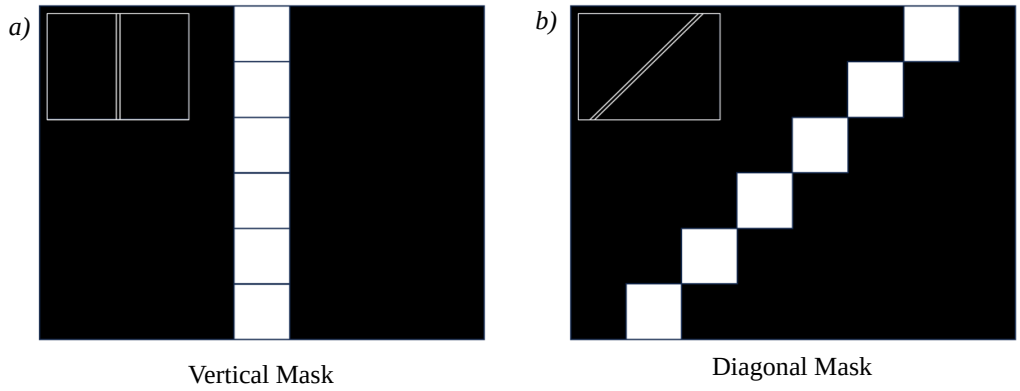

Figure 4.3: ***a)*** Image of a mask without pre-tilting (the chosen method) where rotation is required during the analysis step. In the top left corner of the diagram is the full mask showing the double slit in question. ***b)*** Image of a pre-tilted mask to be placed onto the DMD. Similarly, the diagram also shows in the top left corner the entire mask with double slits in question. The pre-tilting results in a diagonal line built up of square pixels creating a non-uniform profile across the slit.

An opposing method is pre-tilting the mask going into the DMD as seen in **Figure 4.3** ***b)***. If the masks were pre-tilted, this would produce an image which does not need rotating during analysis, however, the pre-tilting means the slits on the mask are diagonal. This results in the slit having jagged instead of straight, neat edges, producing a disorderly slit width much like a sawtooth edge with varying slit width along its profile.

As shown previously in **Figure 4.2**, the intensity distribution produced is a 2D image. However, the analysis only requires a singular line profile across this 2D image. To improve the accuracy of the analysis, an averaging method was employed whereby the entire 2D image is averaged perpendicular to the required line profile. This averaged array is then used as the line profile for analysis producing

very uniform results. This enables clear comparisons between experimental and simulation results to determine the resolution of the DMD.

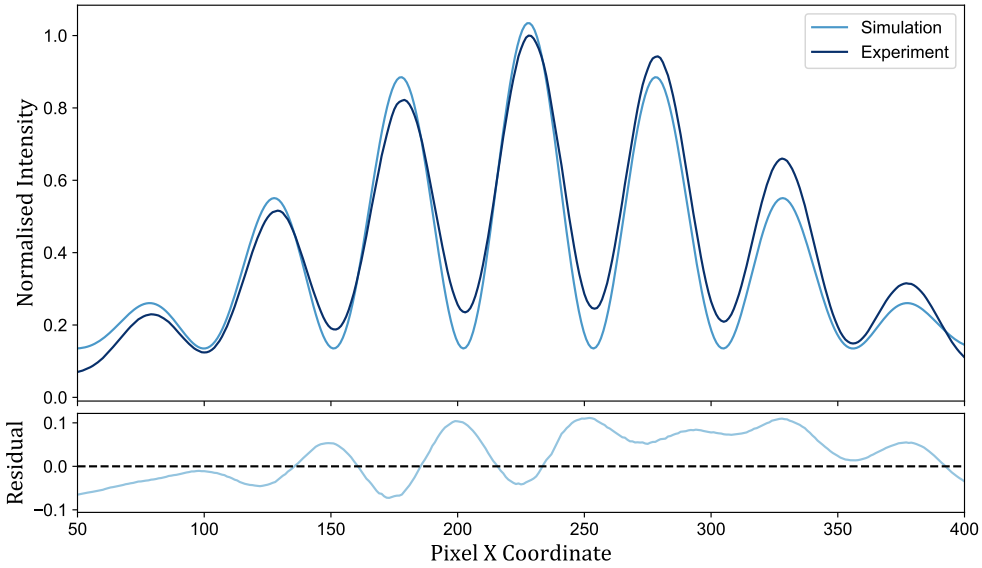

Figure 4.4: Example comparison between experimental data for a slit width of 70 µm, and a slit separation of 260 µm for 450 nm, and a simulation of similar parameters.

As stated earlier, the resolution of the DMD is equivalent to the dimensions of a single mirror given that this is the smallest possible dimension that the DMD is capable of using for modulating the incident light. From **Figure 4.4** a comparison between the anticipated diffraction patterns deduced from mirror dimensions and the captured experimental data shows agreement in manufacturer specified mirror dimensions and therefore resolution output of the DMD. The mirror pitch is stated by Texas Instruments to be 13.7 µm, and reduced chi-squared fitting of the simulation suggests that the experimental results match a theoretical mirror size and resolution capability of (12.9 ± 1.1) µm. The error here is determined by taking a variety of possible slit widths and separation example simulations and comparing to experimental results for each to attain a range of analysed mirror dimensions. The highest and lowest values in this range are then used to determine the error margin, and the average is the anticipated mirror dimension and therefore resolution.

The residual plot between the experiment and simulation data shows slight variation from left to right such that the simulation over estimates on the left and under estimates on the right. This is likely due to a systematic error with an offset of the incident Gaussian beam upon the DMD array causing the experimental data to skew in intensity and not an issue with the DMD's resolution capabilities. Additionally, it should be noted that the overall resolution of the THz modulator, as later characterised in **Chapter 6**, is fundamentally constrained by the wavelength of the THz radiation and the diffusion dynamics of photogenerated carriers within the silicon. Although the DMD features a high native resolution, with individual pixel dimensions of approximately 13.7 µm, this scale is substantially smaller than the free-space wavelength of the 550 GHz beam, which is approximately 545 µm. Consequently, the spatial resolution of the modulator is not limited by the DMD itself, but rather by the intrinsic diffraction limit of the THz radiation and the carrier diffusion length in the photoexcited silicon. This ensures that the DMD provides sufficient spatial definition for effective optical masking, without imposing a bottleneck on the achievable modulation resolution.

4.3 Frame Rate

The idea of using multiple still images in succession to emulate a motion picture dates back over a hundred years to the time of Eadweard Muybridge [131] and Louis Aimé Augustin Le Prince [132]. The official inventor of the idea is widely disputed, but its effectiveness is not. Since its creation, the concept has been utilised in countless industries across the globe. Starting with only the capabilities to emulate a motion picture at tens of frames per second, innovation has led to productions of machines capable of tens of thousands of frames per second. One such machine is the V7000 Vialux DMD used in this work which is specified to have a frame rate capable of 22,000 Hz.

4.3.1 Image Sampling Theory

When the DMD is updating its mask at its maximum refresh rate, to the human eye it cannot even be perceived to be changing state. In fact, the majority of imaging equipment will be unlikely to even notice an effect at such high speeds. To capture the DMD a camera capable of extremely fast capturing is required. For the data collection in this experiment a high speed Phantom VEO 610L camera is utilised. Such a camera is capable of 20,840 fps at 640 x 480 enabling it to capture the refresh rate of the DMD for characterisation up to approximately 10,000 fps due to temporal aliasing according to the Nyquist-Shannon sampling theorem [133].

4.3.2 Frame Rate Analysis

To extract the frame rate of the collected high-speed images we first organise the captured images chronologically. These images now represent consecutive frames in the sequence of events that took place. The time step between these images corresponds to the capture rate the Phantom camera was set to, the camera also ensures a consistent temporal sampling rate. A chronological 1D signal is then created by extracting intensity values of all pixels in each image and averaging them independently. This results in a single 1D array of data where the values represent image intensity, and the order of the data represents progression through time.

Applying the Fast Fourier Transmform (FFT) to the 1D signals obtained from the pixel intensities over time means the FFT evolves the signal from the time domain to the frequency domain, revealing the frequency components present in the data. Then by examining the resulting frequency spectrum obtained from the FFT it becomes possible to identify the dominant frequency component, which corresponds to the frequency of repetitive patterns or changes in the image sequence. By now taking into account the frame rate the camera is set to during capturing, this dominant frequency or repetitive pattern represents the frame rate of the image

sequence as the pattern corresponds to 'on' and 'off' images changing state (or more technically, it corresponds to higher and lower average intensity data changing values over time). The reciprocal of this dominant frequency gives the frame rate of the image sequence.

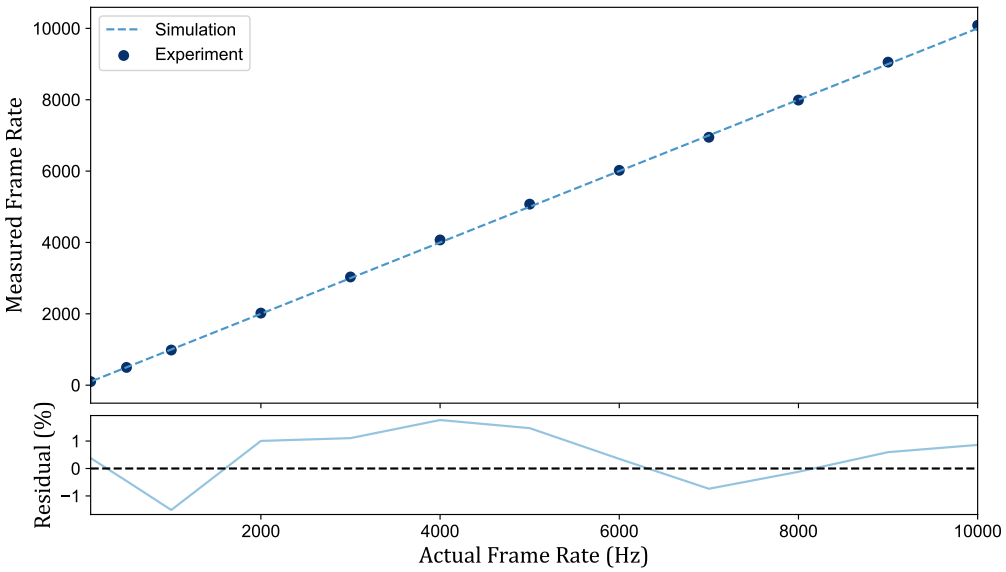

Figure 4.5: A comparison of all measurements taken between 100 and 10,000 Hz for actual verses measured frame rates for the DMD after performing FFT on the captured image intensities.

The results in **Figure 4.5** show a range of tests performed from 100 Hz up to the aliasing limit of 10,000 Hz. For each example frame rate, the test was run three times and results averaged to determine the final measured frame rate and associated error. There was consistent agreement between the anticipated frame rate and that which was measured across the entire range up to 10,000 Hz with a typical error margin of less than 1.4% as seen from the residual plot. This suggests that the DMD is capable of accurately delivering up to 10,000 fps as expected which when compared to the THz imager to be used in **Chapter 6** with a capture rate of similar magnitude suggests the chosen DMD should be effective in this design.

4.4 DMD Power Efficiency

Within the realm of scientific imaging, the quest for clarity and precision is unyielding. Power-efficient optical systems emerge as pivotal allies in this pursuit by effectively minimising noise levels inherent in imaging processes. Particularly crucial in fields such as astronomy [134], microscopy [135], and medical imaging [136], where these systems optimise signal-to-noise ratios, fostering the capture of clearer and more reliable images. By curbing noise interference, we can attain heightened accuracy in data acquisition and analysis, thus advancing scientific inquiry with greater confidence and precision.

In addition to improved resolution, the ability to discern subtle signals amidst complex backgrounds is paramount. Power-efficient optical systems play a transformative role in enhancing signal detection sensitivity, empowering detection of fainter signals or nuanced changes in intensity [137]. This capability is especially critical in fields like fluorescence microscopy [138], where the detection of weak signals against a backdrop of noise presents a formidable challenge. Through the optimisation of optical components, these systems bolster the capacity to glean insights from intricate datasets, facilitating breakthroughs in scientific understanding.

By harnessing specific lenses and components designed to improve power efficiency in optical systems, the performance of the system can benefit in the aforementioned ways. A key aspect is Anti-Reflection (AR) coating [139], typically used on reflective surfaces such as lenses and mirrors. Coordinating the chosen illuminating laser wavelength with the correct AR coating can greatly impact the power efficiency of the system. In the case of the THz modulation system in question here, an important component is the DMD which is a reflective surface and is coated with AR coating. However, the nature of the micro-mirrors leads to blaze diffraction of the incident laser source which is also wavelength dependent [140]. Therefore, not only does AR coating need to be considered, but also the blaze diffraction effects

of the DMD in order for the system to reach peak power efficiency.

4.4.1 Super Continuum Laser

To fully characterise the DMD's power efficiency it needs to be tested across a range of wavelengths. This means a single laser diode typically used in previous characterisation tests producing only a single wavelength would not be adequate for such testing. Instead, a Super Continuum Laser [141] such as the SuperK discussed in **Chapter 3** would be beneficial for scanning a range of wavelengths effectively.

The SuperK EVO EU-4 Laser along with the SuperK LLTF Contrast VIS HP8 is capable of scanning 400 – 1000 nm with a spectral bandwidth less than 2.5 nm. This covers the operational wavelength range of the DMD at 400 – 700 nm. By setting up the DMD and then scanning the wavelength range in steps of 10 nm and capturing intensity distributions produced by the DMD, a good understanding of the blaze-dependent diffraction efficiency can be determined [142]. For more information on the SuperK laser refer to **Appendix B**.

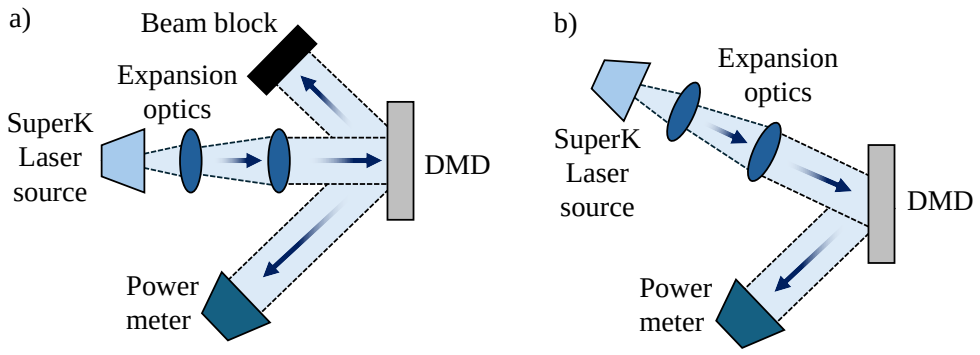

Figure 4.6: The SuperK laser setup with the DMD in two variations to compare blaze diffraction from ***a)*** with coating effects from ***b)***. In ***a)*** the DMD is 'activated' with mirrors tilted whilst in ***b)*** the DMD is 'deactivated' and in float mode with mirrors set to 0 degrees.

The optical arrangement used to evaluate the blaze diffraction efficiency of the DMD is shown in **Figure 4.6**. In **Figure 4.6 a)** a broadband beam from the NKT SuperK laser was collimated, expanded, and directed onto the DMD at a fixed angle of incidence. The power output data was collected via a power meter placed

at the first-order diffraction angle corresponding to the expected blaze maximum. The beam block in this case is more of a safety feature as all light is expected to head towards to the power meter via diffraction. A second configuration was also used in **Figure 4.6 b)** where the DMD is deactivated and the mirrors return to a float state at 0 degrees. In this float state the DMD acts like a typical mirror but with grating diffraction effects but, crucially, without blaze diffraction effects due to no tilting of the mirrors. These two DMD mirror configurations could then be compared: an "activated" state in which all mirrors were tilted to +12°, thus enabling angular blaze diffraction; and a "float" state, in which mirrors were held at 0° to approximate a flat mirror configuration. This dual-mode comparison permits direct measurement of blaze-induced diffraction efficiency relative to standard reflection, highlighting the influence of angular tilt on system performance.

In **Figure 4.7**, both the activated and deactivated (float states) show measurable optical power, which may initially seem counterintuitive. However, this arises from the nature of broadband illumination and the angular acceptance of the collection system. In the float mode, mirrors reflect specularly across the array surface, and the measured signal corresponds to typical broadband reflection from the DMD coating. In contrast, the activated state induces wavelength-dependent diffraction governed by the blaze condition, causing selective enhancement at angles satisfying constructive interference. Due to the finite bandwidth of the source and imperfect angular filtering, some overlap in detected power between these two states is expected.

This configuration does not imply poor contrast in projected images. Instead, it demonstrates the relative efficiency of the DMD when used in typical blaze diffraction conditions. In practical THz modulation operation, structured patterns are projected using narrowband laser sources and additional angular filtering optics, enhancing contrast by suppressing off-angle or broadband scatter. The image contrast achieved in **Chapter 6** confirms that, despite moderate overlap in this comparison measurement, the DMD provides sufficient spatial modulation perform-

ance when integrated into the full system.

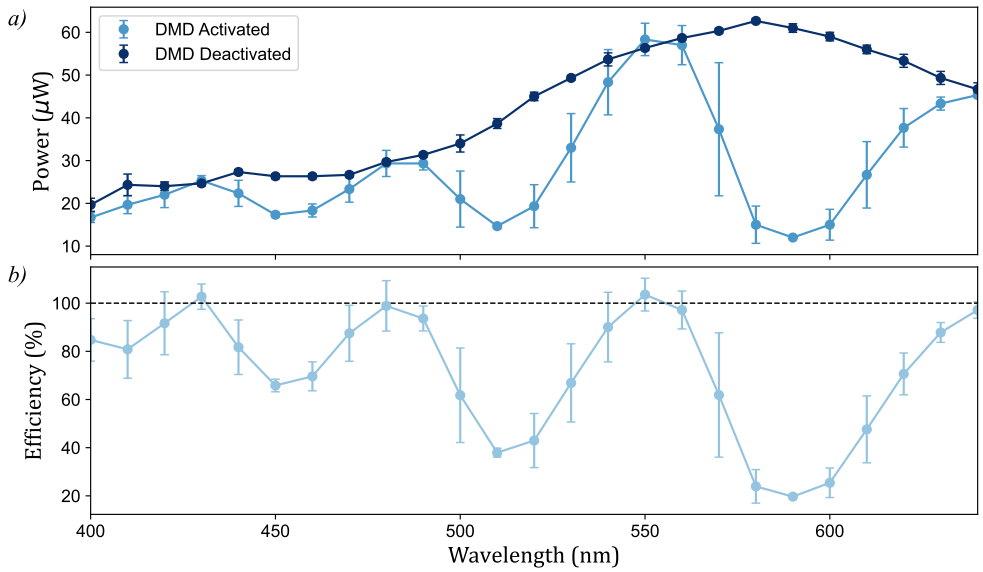

Figure 4.7: ***a)*** Depicts the average reflected laser power at a given wavelength from the DMD when it is both deactivated (set to float mode) and activated (set to entirely 'on' mode). ***b)*** Depicts the normalised output by dividing the activated data by the deactivated to remove intrinsic laser properties and normal diffraction grating effects due to the use of micron-sized mirrors. This leaves just the effects of blaze diffraction on the reflected power relative to incident wavelength.

The data in **Figure 4.7** is acquired from the setup depicted in **Figure 4.6** and it can be seen that the SuperK laser has effectively characterised the blaze diffraction properties of the DMD. There is a rhythmic pattern presented in the data, in which peaks correspond to blaze wavelengths where the maximum potential laser power is concentrated into a central order, and troughs are the counter to this where maximum potential laser power is divided among central orders. Therefore, for this DMD, wavelengths such as 450 nm, 515 nm, and 590 nm all result in a critical drop in DMD reflection efficiency due to these wavelengths residing in the trough regions. Conversely, 430 nm, 480 nm, 550 nm, and 640 nm provide excellent reflection efficiency for this particular DMD.

With these results in mind, the wavelength for the laser in the THz modulation system can be chosen such that power efficiency is maximised while also complying

with any other restraints set by the rest of the system. Restrains such as the maximum power output of the chosen laser diode must be relatively high to create the required excitation in the semiconductor element of the system [143]. A laser diode such as the L637G1 (discussed in **Chapter 3**) provides 637 nm which falls into the required efficiency peak from **Figure 4.7**. The diode also provides up to 1.3 W of power which fulfils the high power constraint of the system requirements thus making it an ideal choice of diode in this modulator design at least in terms of efficient reflection from the DMD.

4.4.2 Blaze Simulations

The term "blaze" in blaze diffraction refers to the strategic orientation of the micromirror surface, which optimises the diffraction efficiency for specific wavelengths or spectral bands [144]. By carefully tuning the angle of the micromirror facets, the diffraction efficiency can be maximised at desired wavelengths while minimising unwanted scattering or dispersion effects.

The diffraction efficiency of a DMD therefore depends on several key factors, including the angle of incidence, the wavelength of light, and the geometric parameters of the micromirror array. These parameters are looked at for reference in **Appendix C**. By combining these parameters, a simulation of the anticipated blaze diffraction can be created. From this simulation it would then be possible to determine the diffraction efficiency of the DMD under different illumination wavelengths and thus verify the most efficient wavelengths to be operating at.

Numerous studies and application notes have modelled DMD blaze conditions using both scalar diffraction theory and rigorous coupled wave analysis [145, 146], which confirm the angular and wavelength dependencies of peak efficiency. Therefore the theory required to simulate the blaze diffraction efficiency has already been extensively explored [147] and shall be used here to verify the effects witnessed in **Figure 4.7**. In brief, the DMD's far-field diffraction pattern is determined by

the Fourier transforms of pixel functions, considering the aforementioned factors of device's geometry and incident light angles. The diffraction angle for the m^{th} order is given by $(\lambda f_x)_m = \sqrt{2}(m\lambda)/p - sin(\theta_i)$, where λ is the wavelength of incident light, f_x is the spatial frequency corresponding to the m^{th} order in the x-direction, m is an integer diffraction order, p is the pixel pitch, and θ_i is the incident angle of incoming light relative to the normal of the DMD surface. The energy diffraction efficiency for the m^{th} order can then be expressed as

$$\eta_m = sinc^4 \left[\frac{w}{\sqrt{2}\lambda} \left[\frac{\sqrt{2}m\lambda}{p} - (sin(\theta_s) + sin(\theta_i)) \right] \right], \tag{4.3}$$

where η_m is the energy diffraction efficiency for a given m^{th} order, w is the micromirror width, and θ_s is the scattering angle determining the angle at which the light is collected. This equation illustrates how diffraction efficiency varies with wavelength and diffraction order, highlighting the DMD's performance across different wavelengths.

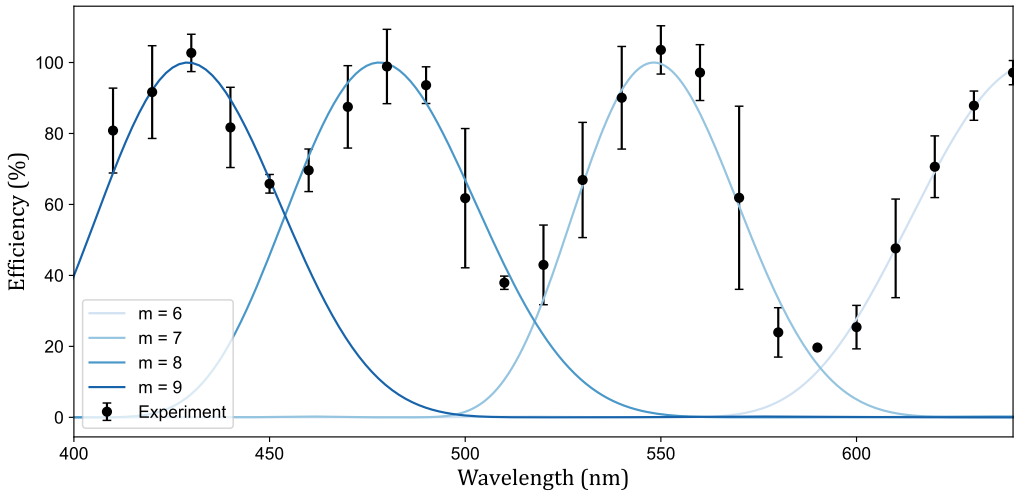

Figure 4.8: The graphs depict a comparison between the blaze simulation [147] and experimental results for the DMD with 13.7 µm mirror pitch, a mirror tilt of 12.4 degrees, and a wavelength range of 400 to 700 nm.

From the theory in **Equation 4.3**, we can now construct a simulation of the blaze diffraction intensity distribution corresponding to wavelength. By specifying known values of the DMD, such as the mirror tilt angle and the mirror pitch, which

is the distance between corresponding mirror centres, the normalised intensity can be deduced.

As can be seen in **Figure 4.8**, the expectations of the blaze effects closely match the results seen in the collected super continuum data. Therefore, validating the conclusions drawn concerning the optimum wavelengths to choose from regarding illumination wavelength to utilise in coordination with this particular DMD to ensure the best design possible.

4.5 Conclusions

This chapter aimed to capture three key characteristics of the V7000 Vialux DMD required for the effective design of the THz modulation system. These key features were the resolution capabilities of the DMD, the maximum frame rate potential of the device, and the power efficiency of this component. It was shown using double slit diffraction analysis that the resolution of the DMD is (12.9 ± 1.1) µm which is sub-wavelength in comparison to the THz signal that the DMD is to be modulating. This suggests the DMD is more than capable of performing the required masking step it was chosen for.

Frame rates of the DMD were shown to be accurate and reliable up to at least 10,000 Hz. This is on the order of magnitude the THz imaging system is capable of [6] and therefore shows the DMD again matches requirements. Finally, the power efficiency of the device was tested over a variety of wavelengths with a super continuum laser. This characterised blaze diffraction effects intrinsic to DMDs. It was found that the device had a peak efficiency transmission to a central order peak at 637 nm, and a low efficiency transmission to a central order at 450 nm. Based on these results it would suggest that the V7000 Vialux DMD is an exemplary choice for use within the design of a THz spatial modulation system.

Chapter 5

Silicon Characterisation

In this chapter we characterise a silicon sample used in designing a THz spatial light modulator. Fundamental factors such as purity, structural defects, and resistivity are examined due to their critical impact on silicon's optical and electrical responses under photoexcitation. Techniques including Energy-Dispersive X-ray Spectroscopy (EDS), Transmission Electron Microscopy (TEM), and Scanning Transmission Electron Microscopy (STEM) assess these imperfections and their effects. These techniques were performed with assistance from Kaviyadharshini Dhamotharan and Prof. Budhika Mendis. The discussion then explores sample thickness and tilt angle before finally investigating modulation effects from variations in optical excitation intensity and wavelength. Understanding these dependencies is crucial for achieving high modulation efficiency, contrast, and precise control in practical THz applications discussed in **Chapter 6**.

5.1 Introduction

Silicon, a cornerstone material of modern technology, has profoundly shaped the landscape of electronic and photonic devices over the past century. Discovered in 1824 by the Swedish chemist Jöns Jacob Berzelius [148], silicon initially found modest applications in alloy production [149]. However, the true technological significance of silicon began emerging in the mid-20th century, primarily driven by the

invention of the silicon transistor in 1954 by Morris Tanenbaum at Bell Labs [150]. This pivotal event marked the dawn of the semiconductor era, transforming silicon into the fundamental building block of microelectronics, powering the computing revolution and enabling the proliferation of digital technology globally [151].

Silicon's unique combination of properties, including its abundant availability, stable crystal structure, and semiconductor characteristics, has cemented its dominance in the electronics industry. It became the primary substrate for integrated circuits, ushering in continuous advancements under Moore's Law [152], which accurately predicted the exponential increase in transistor density on silicon chips. Consequently, silicon-based technologies have found widespread use in computers, smartphones, photovoltaic solar cells, and various sensor applications [153–155]. Its versatility, reliability, and cost-effectiveness underpin its sustained preference over alternative materials.

However, silicon is not without its limitations. One notable constraint is its indirect electronic bandgap, which hampers efficient light emission, thus limiting its applications in optoelectronic devices like lasers and light-emitting diodes (LEDs) [156]. Additionally, silicon's performance begins to degrade significantly at frequencies beyond the microwave region [157], presenting challenges for applications in the THz spectrum. THz technology, poised to revolutionise fields such as imaging, communications, spectroscopy, and security screening, demands materials with superior electronic and photonic characteristics beyond silicon's conventional capabilities.

Despite these limitations, silicon has demonstrated remarkable adaptability, evolving through innovative engineering approaches that have significantly extended its functional scope. Techniques such as doping, heterostructure formation, and photoexcitation have been extensively explored to enhance silicon's intrinsic properties, enabling new functionalities [158, 159]. Photoexcited silicon, in particular, represents a promising direction for overcoming traditional barriers associated with silicon's indirect bandgap and limited high-frequency response. By optically

exciting charge carriers within silicon, it is possible to transiently modify its electrical and optical properties, enabling dynamic control of electromagnetic radiation across a wide frequency range, including the challenging THz domain.

Nonetheless, alternatives to silicon continue to garner significant research interest, driven by the need to surpass silicon's intrinsic limitations. Materials such as gallium arsenide (GaAs), indium phosphide (InP), graphene, and various metamaterials have emerged as promising candidates in the pursuit of superior THz performance [160–163]. GaAs and InP exhibit direct bandgaps and higher electron mobilities, making them attractive for optoelectronic and high-frequency applications. Graphene, with its extraordinary electronic properties, including ultra-high carrier mobility and broadband optical response, has shown immense potential for next-generation THz modulators and detectors [164]. Similarly, engineered metamaterials provide unique capabilities, such as negative refractive indices and highly customisable electromagnetic responses, imperative for advanced THz manipulation [165].

However, despite the allure of these novel materials, silicon remains highly attractive due to its mature, large-scale fabrication infrastructure, extensive knowledge base, and environmental stability. Therefore, continued research into silicon's characterisation, specifically under photoexcitation for THz applications, is vital. This chapter aims to comprehensively characterise photoexcited silicon thereby contributing essential knowledge towards optimising silicon-based THz spatial light modulators and overcoming current technological boundaries.

5.2 Sample Properties

In the context of designing a spatial THz light modulator using photoexcited silicon, the presence of impurities and defects in silicon samples is an integral factor influencing the performance of the device. Silicon, while an excellent semiconductor, is not immune to imperfections that arise during its production and processing.

These imperfections, which can take the form of impurities or structural defects, can significantly affect the electrical and optical properties of the material. A key part of understanding the behaviour of silicon in THz light modulators is to examine the nature of these defects and impurities, their specific impact on carrier properties, and methods for manipulating their occurrence. In this section, the fundamental properties of the silicon samples utilised for THz modulation are examined, with particular focus on the presence and impact of impurities, structural defects, and the high-resistivity float zone method employed to enhance material quality.

5.2.1 Sample Impurities

Impurities in silicon can be broadly classified into two categories: intentional and unintentional. Intentional impurities, or dopants, such as phosphorus and boron, are introduced to modify the electrical properties of silicon by controlling its conductivity. However, in the context of THz modulation, it is indispensable to manage the concentration of these dopants carefully, as excessive doping can create scattering centres that degrade the mobility of charge carriers as discussed in **Chapter 2**.

Unintentional impurities such as oxygen, carbon, and metallic contaminants such as iron, nickel, and copper can be introduced during the crystal growth or processing steps. Oxygen, for example, is commonly incorporated into silicon during the Czochralski (CZ) growth method [166]. It can precipitate within the silicon lattice, leading to the formation of scattering centres that reduce carrier mobility and act as traps for carriers, ultimately lowering the effective carrier lifetime. Carbon impurities, while less common, can result in the formation of silicon carbide precipitates, which further degrade the transport properties of the material.

To assess the impurity content of the silicon sample used in this study EDS analysis was employed. EDS is an analytical technique used to determine the elemental composition of materials by detecting the characteristic X-rays emitted

from a sample when it is bombarded with an electron beam; see **Appendix A** for more details. The process involves exciting atoms within the material, causing them to emit X-rays with energy levels unique to each element. These emitted X-rays are then analysed to identify the presence and relative abundance of elements within the sample.

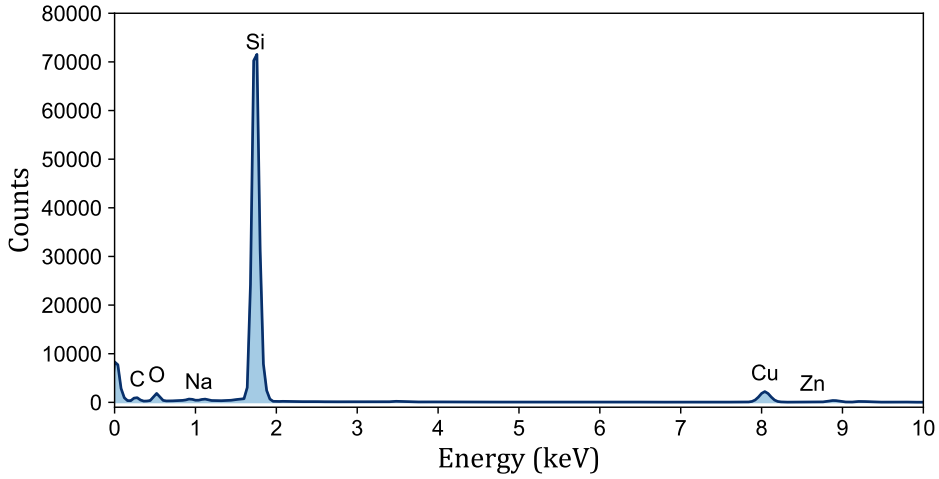

Figure 5.1: An EDS analysis indicating predominantly silicon contents and showing no detected impurities which implies the sample is of high purity.

The EDS analysis of the silicon sample in **Figure 5.1** revealed no detectable traces of unintentional impurities, with the spectrum predominantly indicating the presence of silicon. It should be noted that the slight presence of copper is expected to arise from the copper grid used to hold the sample during the experiment. This suggests that the material is of high purity and does not contain significant concentrations of oxygen, carbon, or metallic contaminants that could adversely affect its electronic or optical properties. This absence of detectable impurities is particularly relevant for THz applications, as it reduces the likelihood of scattering centres and defect states that could compromise modulation performance.

However, it is vital to note the limitations of EDS, which typically has a detection threshold around 0.1-0.5 atomic percent. Therefore, impurities below this threshold may remain undetected despite their potential to impact semiconductor performance. For a more sensitive analysis of trace impurities, Secondary Ion Mass

spectrometry (SIMS) or Fourier-Transform Infrared Spectroscopy (FTIR) could be employed, as these techniques offer significantly lower detection limits, making them ideal for confirming ultra-high purity silicon required for THz modulation applications [167, 168].

5.2.2 Sample Defects

In addition to potential foreign impurities, silicon samples can also contain intrinsic defects, which arise from imperfections within the silicon crystal lattice itself. These defects include vacancies, where silicon atoms are missing from their lattice positions, and interstitials, where silicon atoms occupy spaces between the regular lattice sites. Both types of intrinsic defects can trap charge carriers, leading to increased recombination and a reduction in overall electrical performance of the material. Dislocations, another form of intrinsic defect, involve a misalignment of atoms within the crystal lattice. These dislocations can create strain fields that scatter carriers and degrade their mobility, further compromising the performance of silicon in THz modulators.

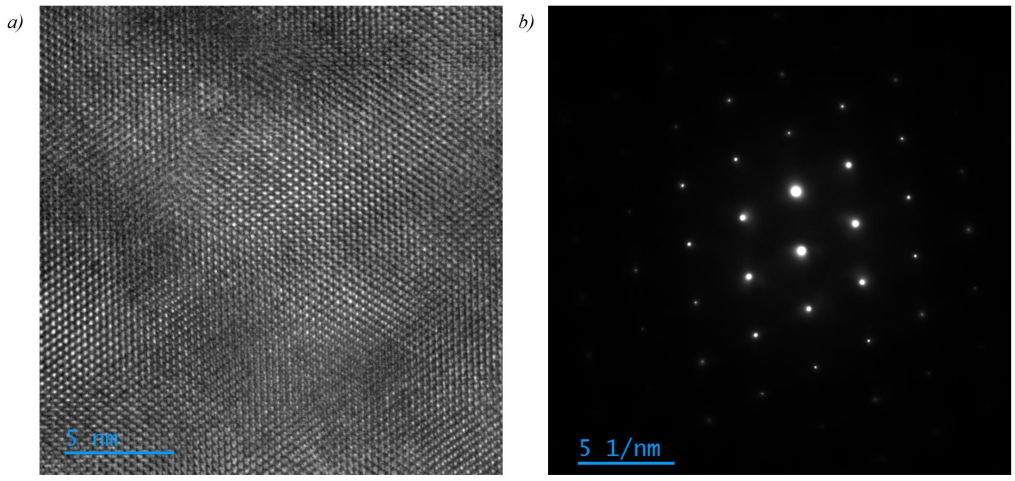

Figure 5.2: The TEM bright field image of the silicon lamella prepared using FIB demonstrating slight non-periodicity is shown in **a)**. The SAED pattern showing well-defined spots implying a crystalline lattice and that any deformations must be localised is shown in **b)**.

To investigate the presence of such defects in the silicon sample, imaging was

performed using TEM analysis. A thin lamella of the sample was prepared using FIB milling, allowing for detailed structural analysis. Bright-field TEM imaging shown in **Figure 5.2 a)** revealed slight non-periodic variations in the lattice, suggesting the presence of dislocations within the crystal structure. While these variations were subtle, their identification is indispensable since even low densities of dislocations can significantly influence material properties through carrier scattering and recombination enhancement. Importantly, such defects can compromise the uniformity of THz modulation across the wafer, leading to spatial inconsistencies in the modulation performance.

To further characterise the crystallinity of the sample, Selected Area Electron Diffraction (SAED) was performed [169]. **Figure 5.2 b)** shows the resulting diffraction pattern confirming that the silicon sample is crystalline rather than amorphous, as evident from the presence of well-defined diffraction spots rather than diffuse rings. This confirms that the structure is ordered at the atomic scale, with any observed dislocations likely being localised rather than indicative of large-scale disorder.

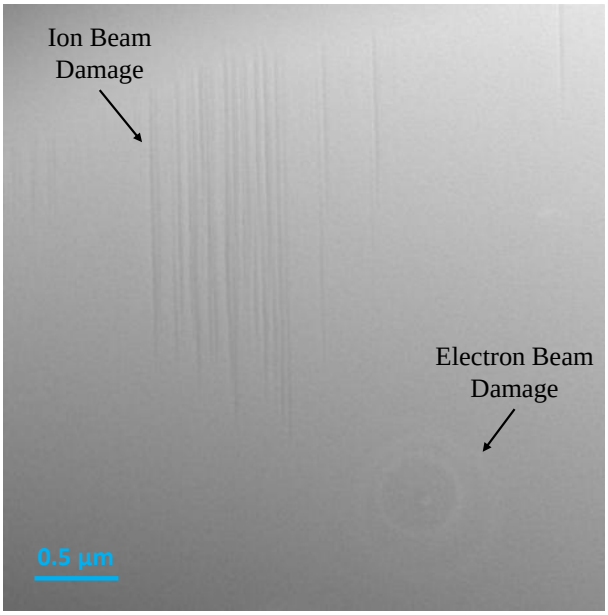

Figure 5.3: Bright field STEM imaging of the silicon sample showing no evidence of structural defect streaking. Evidence of ion and electron beam damage is highlighted.

To determine whether the apparent non-periodicity seen in the TEM image is a genuinely localised structural defect or an artefact caused by beam damage during FIB preparation, STEM imaging was conducted. STEM, which offers higher spatial resolution and contrast sensitivity compared to conventional TEM, provides further insight into the defect distribution and potential strain regions within the silicon lattice. The STEM results in **Figure 5.3** revealed no evidence of local dislocations or structural defects at the nanoscale, suggesting that the non-periodicity observed in the TEM image is more likely a result of ion beam damage introduced during the FIB milling process rather than an intrinsic defect within the silicon. This damage is highlighted in the figure taking the form of what is known as curtain damage. Additionally, electron beam damage can been seen by the rings present. Therefore, these results suggest the sample used in this work has no detectable impurities or defects, making it theoretically suitable for use in THz modulator designs.

5.2.3 High Resistivity Float Zone Method

The presence of any impurities or defects would directly affect several key properties of silicon, which are indispensable for the performance of THz light modulators. One of the most significant of these properties is carrier mobility, which refers to how quickly charge carriers can move through silicon when subjected to an electric field. Impurities and defects act as scattering centres, reducing this mobility and thus limiting the material's ability to respond effectively to modulation signals. For example, oxygen-related defects can trap carriers and restrict their movement, leading to a reduction in modulation efficiency. Similarly, dislocations and vacancies further degrade mobility by increasing the likelihood of phonon scattering.

Another important property affected by impurities and defects is the carrier lifetime, which is the average time a charge carrier exists before it recombines. Metallic impurities, particularly those like iron and copper, create deep-level traps that accelerate recombination. This rapid recombination reduces the number of carriers available for modulation, thus degrading the performance of the modulator by

reducing the carrier lifetime. Furthermore, defects that increase the recombination rate limit the depth and bandwidth of modulation, further reducing the overall efficiency of the device.

Given the significant impact of impurities and defects on the performance of silicon, it is imperative to adopt methods that manipulate their occurrence. One of the most effective techniques for reducing impurity in silicon is the Float Zone (FZ) growth method [170]. Unlike the CZ process, which introduces a significant amount of oxygen during crystal growth, the FZ method involves passing a molten zone through a silicon rod, allowing impurities to segregate and move out of the crystal. As a result, silicon produced through the FZ method is of much higher purity, with lower levels of oxygen and other metallic impurities. This reduction in impurity concentration is particularly beneficial for applications that require high carrier mobility and long carrier lifetimes, such as THz modulators.

A more refined variation of the Float Zone method is the High Resistivity Float Zone (HRFZ) technique, which is specifically designed to produce silicon with extremely high resistivity [171]. The HRFZ process results in silicon that has very low levels of both oxygen and metallic impurities, making it ideal for applications in which low defect concentrations and minimal impurity scattering are important and therefore is the chosen growth method for this work. Silicon grown using the HRFZ method has fewer recombination centres, leading to longer carrier lifetimes and improved mobility, both of which are crucial for efficient THz modulation.

In addition to crystal growth methods, techniques such as thermal annealing and gettering are employed to repair or isolate defects. Annealing allows silicon atoms to return to their proper lattice positions, reducing the number of vacancies and interstitials, while gettering techniques trap impurities in regions of the silicon that do not affect the device's active areas.

5.3 Etalon Effects

In the development of silicon-based THz modulators, understanding etalon effects is essential, as these effects can significantly influence the efficiency, precision, and tunability of THz modulation. When THz radiation is transmitted through a silicon wafer, interference effects, known as etalon effects, can occur. An etalon is a device consisting of two parallel reflecting surfaces, which can create multiple reflections of an incident light beam within the cavity formed by these surfaces. This phenomenon leads to constructive and destructive interference patterns that modify transmitted and reflected signals.

When THz radiation enters the silicon wafer, it encounters the boundary between air and silicon. Due to the difference in refractive indices, part of the THz wave is transmitted to silicon, while part is reflected back into the air. This was demonstrated previously in **Figure 2.7** from **Chapter 2**. The transmitted wave continues to propagate through the silicon wafer until it reaches the opposite boundary, where a similar partial reflection and transmission occur.

The THz waves reflected back and forth within the silicon wafer interfere with each other. If the distance between the paths of successive reflections is an integer multiple of the THz wavelength, constructive interference occurs, enhancing the transmitted signal at certain frequencies. Conversely, if the path length difference is a half-integer multiple of the wavelength, destructive interference occurs, reducing the transmitted signal at those frequencies. In this section we shall explore the parameters influencing the etalon patterns, and discuss the potential to fine-tune the modulator using these effects.

5.3.1 Sample Thickness Dependence

The transmission function of the silicon wafer, accounting for etalon effects, can be mathematically described by considering the interference of multiple reflected

waves. The intensity of the transmitted THz radiation (I_t) can be expressed as:

$$I_t = I_0 \frac{(1-R)^2}{1 - 2R\cos(2\delta) + R^2}, \tag{5.1}$$

where I_0 is the incident intensity, R is the reflectance at the silicon-air interface, $\delta = 2\pi nd/\lambda$ is the phase difference between successive reflections, n is the refractive index of silicon, d is the thickness of the silicon wafer, and λ is the wavelength of the THz radiation. The refractive index and reflectance can be approximated by using Fresnel's equations discussed in **Equation 2.6** to be 3.42 and 30% respectively.

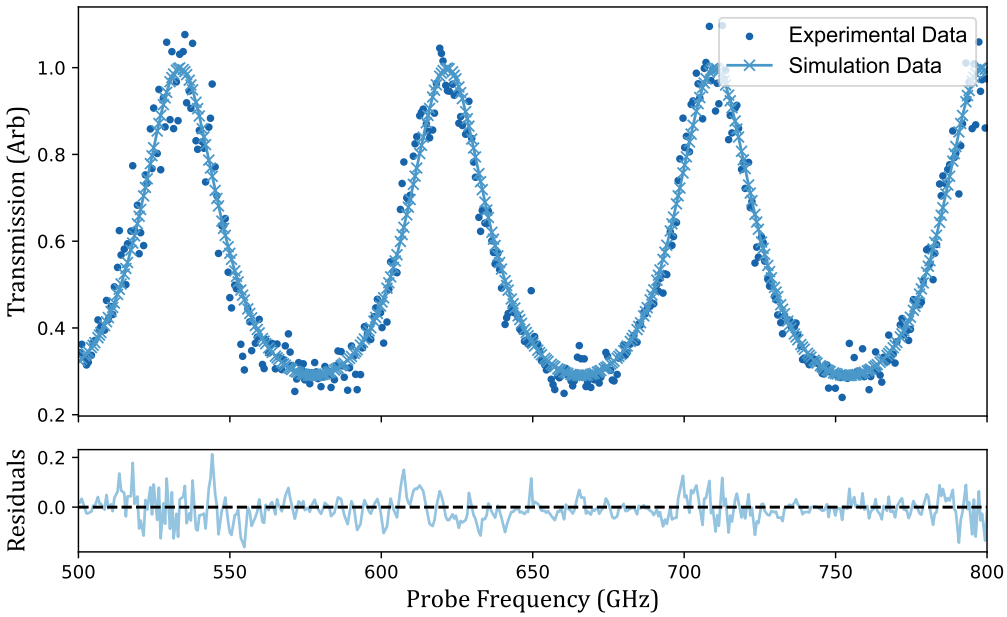

Figure 5.4: Terahertz probe frequency against transmission intensity for a wafer of 480 µm thickness showing a comparison of silicon's experimental etalon period against its theoretical simulation.

By using **Equation 5.1**, it is now possible to create a simulation of the etalon patterns produced by a silicon sample of known thickness. **Figure 5.4** is the experimental data compared against the simulation results where the experimental data is collected by use of the Terascan system, discussed in **Section 3.4.1**, where the transmission is collected by scanning the sample through a range of THz frequencies. This transmission is then normalised by dividing through by the background scan without the sample. Additionally, a residual analysis was conducted, generating a residual plot that exhibited very good agreement between the simulation

predictions and the experimental measurements. The residuals appear randomly distributed around zero without any noticeable patterns or systematic deviations, indicating that the model appropriately captures the underlying trends and variations observed experimentally.

Quantitative analysis further confirmed the robust agreement between the experimental data and simulation outcomes. The Mean Absolute Percentage Error (MAPE) was calculated to be 7.25%, demonstrating that on average, the simulation predictions deviate from the experimental data by approximately this percentage. This relatively low value of MAPE is indicative of high predictive accuracy. Additionally, the Relative Root Mean Square Error (R-RMSE) was computed, yielding a value of 9.4%. The R-RMSE provides an aggregate measure of the magnitude of the prediction errors relative to the range of observed data, further affirming the model's reliability. Overall, both the qualitative residual plot and the quantitative metrics (MAPE and R-RMSE) substantiate the effectiveness of the simulation model, confirming that it provides a reliable representation of the experimental observations.

5.3.2 Fine-tuning Apex Locations

Tilting a silicon wafer is an effective method to alter the locations of the interference maxima (apices) caused by etalon effects in the THz region. The fundamental principle behind this technique involves modifying the path length differences of the multiple internal reflections within the wafer, which in turn affects the interference pattern of the transmitted THz signal.

When a wafer is tilted, the effective optical path length for THz waves changes. This is because the angles of incidence and transmission are modified, thereby altering the distance travelled by the waves within the wafer. The phase difference between successive reflections is a function of this optical path length. In a standard etalon, the effective round-trip distance is $2nd\cos(\theta)$, where n is the refractive

index of the wafer, d is its thickness, and θ is the angle of incidence inside the wafer. Therefore, the phase difference δ is given by $\delta = \frac{4\pi nd\cos(\theta)}{\lambda}$, where λ is the wavelength of the incident THz radiation.

Constructive interference (resulting in maxima or apices) occurs when the phase difference is an integer multiple of 2π, leading to $\frac{4\pi nd\cos(\theta)}{\lambda} = 2\pi m$, which simplifies to $2nd\cos(\theta) = m\lambda$, with m being an integer representing the order of interference. Similarly, destructive interference (resulting in minima) occurs when the phase difference is an odd multiple of π: $\frac{4\pi nd\cos(\theta)}{\lambda} = (2m+1)\pi$, which leads to the simplified $2nd\cos(\theta) = \frac{(2m+1)\lambda}{2}$.

When the wafer is tilted by a small angle α, the effective angle becomes $\theta+\alpha$, and the modified phase difference δ' becomes $\delta' = \frac{4\pi nd\cos(\theta+\alpha)}{\lambda}$. Thus, the new positions of the interference maxima are obtained by $2nd\cos(\theta+\alpha) = m\lambda$. Finally, by considering the relationship between wavelength and frequency, specifically using the relation $\Delta f = \Delta\lambda\left(\frac{c}{\lambda^2}\right)$, and substituting the condition for constructive interference, the Free Spectral Range (FSR) of the wafer can be expressed as:

$$\Delta f = \frac{c}{2nd\cos(\theta+\alpha)}. \tag{5.2}$$

Here, Δf is the frequency difference between successive apices, and c is the speed of light in vacuum.

We can now see that tilting of the silicon wafer should pose as an effective technique for shifting the FSR, and therefore as a means of shifting the locations of the apices. To verify this, transmission data was collected with the Terascan system for a 480 µm thick silicon wafer over a broad range of probe THz frequencies, as presented in **Figure 5.5**. The experiment included tilt angles for the wafer ranging from 0° (normal incidence) to 40°, where increasing tilt progressively modified the etalon interference conditions. Once the scans were completed at each angle, the data for 0 degrees tilt was processed to normalise the transmission by dividing through by the background scan without the sample. For the remaining tilt data,

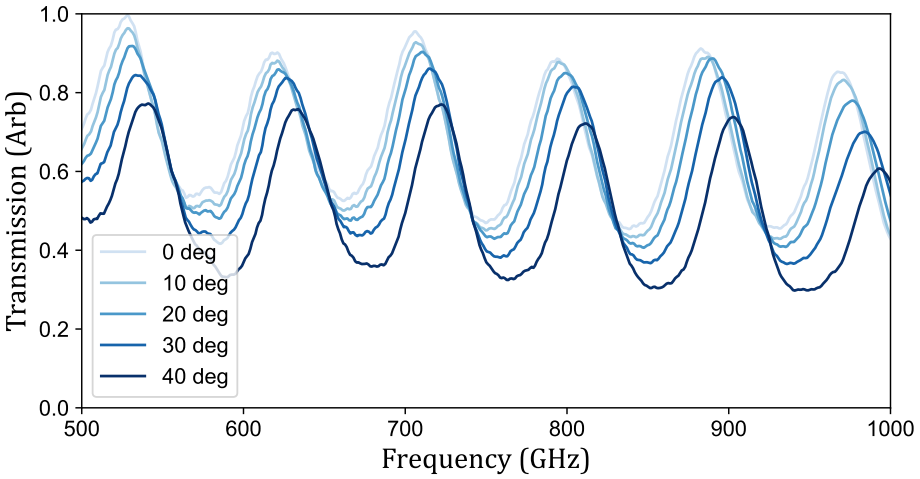

Figure 5.5: Terahertz probe frequency against transmission intensity for a wafer of 480 µm thickness, showing a range of etalon periods for varying tilt angles relative to the normal incident THz radiation.

the transmission was normalised by dividing through by the 0 degree tilt data to retain information concerning the difference in magnitude between these scans.

From an analysis of the data, two significant effects are evident. Firstly, tilting the silicon wafer induces the expected shift in apices locations, confirming the theoretical increase in FSR with tilt. The FSR, from **Equation 5.2**, for the untilted case (0° tilt) was calculated to be 91.9 GHz, closely matching the experimentally observed value of (92.1 ± 1.4) GHz, demonstrating strong agreement between theory and measurement.

This effect becomes increasingly pronounced at higher THz frequencies, as evident in the dataset where, by 1000 GHz, the separation between successive apices differs significantly between tilted and untilted configurations. Theoretical predictions indicate that for a 40° tilt, the FSR should increase by +1.69 GHz, yielding a theoretical FSR of approximately 93.6 GHz. This aligns well with the experimentally measured value of (93.8 ± 1.5) GHz, reinforcing the validity of the model and confirming that tilting provides a controllable mechanism for spectral tuning in THz applications.

Secondly, an overall decrease in transmission amplitude is evident as the tilt

angle increases. This reduction is attributed to a combination of Fresnel losses, increased optical path length, and potential partial Total Internal Reflection (TIR). Specifically, the angle-dependent Fresnel coefficients predict higher reflection losses at the silicon-air interface, leading to reduced transmitted power. Furthermore, as tilt increases, the THz wave propagates through a longer effective thickness of silicon, enhancing both absorption and scattering. This compounding effect explains the monotonic reduction in transmitted intensity as a function of increasing tilt.

For THz spatial light modulators, optimising the modulation performance requires the careful positioning of interference maxima. These results demonstrate that tilt control provides a tunable mechanism for aligning the interference maxima with operating frequencies of interest, maximising modulation efficiency and contrast. This alignment can significantly improve the performance of the modulator by enhancing signal-to-noise ratios and ensuring the modulator is intrinsically designed to operate at the THz frequency of the corresponding imaging device.

5.4 Modulation Effects

The optical modulation of THz signals in silicon is governed by the generation of free carriers under photoexcitation and their subsequent interaction with incident THz radiation. When the silicon wafer is illuminated, charge carriers are excited in a depth-dependent profile governed by the optical absorption coefficient at the excitation wavelength. This leads to an exponentially decaying carrier density into the material, which in turn modifies the local dielectric response via the Drude model. The cumulative effect of this depth-varying permittivity alters the propagation of THz waves through the wafer. Consequently, the modulation depth observed in transmission experiments depends not only on the total carrier population but also on the spatial distribution of carriers relative to the penetration depth of the THz field. These physical relationships, developed more fully in **Chapter 2**, underpin the experimental analyses that follow.

This section presents a characterisation of these modulation effects by focusing on two key excitation parameters. First, the impact of excitation intensity is examined to determine how increasing optical power alters free-carrier absorption and influences the amplitude of transmitted THz signals. Intensity dependence is central to assessing the upper limits of modulation depth, which is essential for high-contrast imaging applications such as the THz spatial light modulator developed here. Second, the excitation wavelength is varied to evaluate how different photon energies affect the depth of carrier generation and the corresponding modulation efficiency. Since shorter wavelengths generate carriers closer to the surface, where the THz field is most sensitive, this dependence is crucial for optimising spatial resolution and carrier localisation in silicon-based THz devices.

5.4.1 Excitation Intensity Dependence

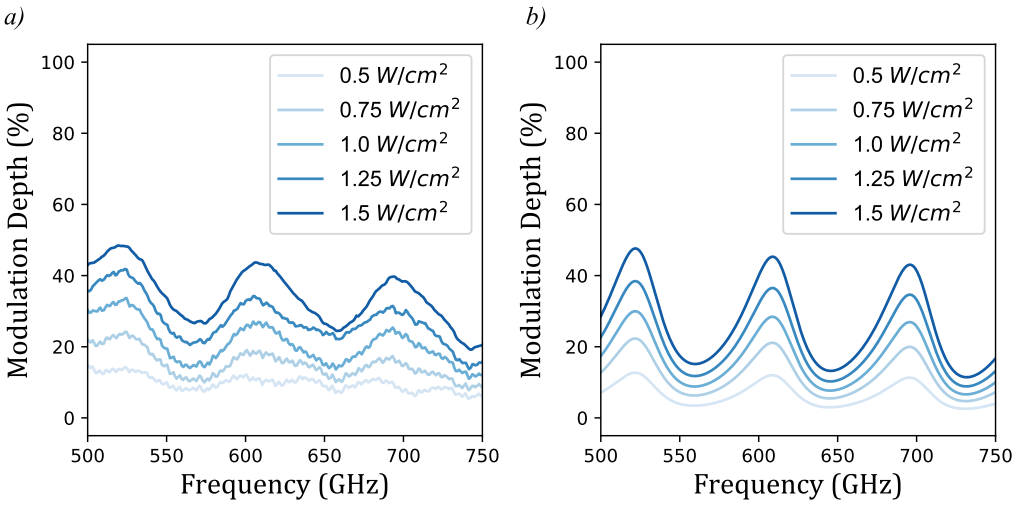

Figure 5.6: Terahertz probe frequencies against modulation depths for an uncoated pure silicon sample (resistivity of 5000 Ω cm, thickness of 480 µm) under varying excitation intensities demonstrating the intensity dependence of silicon's modulation effects for ***a)*** experimental and ***b)*** simulated data.

The influence of optical excitation intensity on THz modulation is primarily dictated by the density of photogenerated carriers. As the excitation intensity increases, the number of electron-hole pairs rises proportionally, leading to enhanced

free-carrier absorption and a corresponding reduction in THz transmission. THz modulation is the comparison of this transmission response to that of a non-excited sample as seen in **Equation 2.28**. The modulation depth as a function of THz frequency and excitation intensity is illustrated in **Figure 5.6**, which demonstrates the progressive attenuation of THz signals, and increased modulation depth, with increasing optical power. This was performed by using the Terascan system to provide THz probing through the silicon sample while exposed to a 450 nm laser, described in **Section 3.3.1**. The intensity was varied by altering the power output of the laser for a set excitation area.

From analysis of the experimental data in **Figure 5.6** ***a)***, several key trends emerge. Higher excitation intensities result in stronger THz absorption, with modulation depth increasing across all THz probe frequencies as laser intensity increases. This confirms that free-carrier absorption is the dominant mechanism governing the modulation process. Additionally, low-frequency THz waves exhibit slightly greater sensitivity to variations in excitation intensity, as the increase in modulation depth is more pronounced at lower THz frequencies. This behaviour aligns with the frequency-dependent nature of free-carrier absorption predicted by the Drude-Lorentz model shown in **Figure 5.6** ***b)***.

This frequency-dependent characteristic can be explained by a second mechanism which involves the Drude-Lorentz absorption characteristics. This is where increased carrier densities result in higher plasma frequencies and stronger absorption at lower THz frequencies. This dependence highlights the role of free-carrier dynamics in shaping the modulation response, with low-frequency THz waves experiencing the most significant attenuation.

A third contributing factor is carrier scattering and recombination. As carrier densities rise, various scattering mechanisms, including carrier-carrier interactions, phonon scattering, and Auger recombination, become increasingly significant. These processes impose fundamental limits on further absorption enhancement, eventually leading to a saturation effect at higher excitation intensities. The com-

petition between free-carrier generation and recombination ultimately defines the efficiency and upper limits of optical modulation in silicon-based THz systems.

In addition to this, further practical limitations exist when increasing excitation intensity beyond certain thresholds. At higher intensities, significant thermal effects can arise due to increased absorption and subsequent heating, potentially leading to thermal damage or degradation of silicon's optical and electrical properties. Limitations in other components must also be considered whereby the masking element (DMD) has thermal limits on the maximum intensity allowed before degradation. Additionally, non-linear effects, such as two-photon absorption, eventually become prominent, reducing modulation efficiency and introducing unwanted optical losses. Therefore, a careful balance must be maintained between achieving high modulation depths and avoiding these adverse effects to ensure long-term device reliability and optimal performance.

5.4.2 Excitation Wavelength Dependence

In addition to optical intensity, the excitation wavelength plays an important role in determining the modulation depth of THz transmission. The penetration depth, absorption coefficient, and carrier generation efficiency all vary with wavelength, leading to significant differences in the spatial distribution of photogenerated carriers and, consequently, the modulation characteristics. As a result, the efficiency of THz modulation is strongly wavelength-dependent.

Figure 5.7 presents a comparison of experimental and simulation data for modulation depth as a function of optical excitation wavelength. This was performed using all three laser diodes described in **Section 3.3.1**, as well as the Ti:Sapphire laser detailed in **Section 3.3.2**. Both datasets follow a consistent trend: modulation depth peaks at lower wavelengths (400 nm), decreases near 500 nm, and then increases again as the wavelength extends toward 900 nm. This non-monotonic behaviour highlights the complex dependence of modulation depth

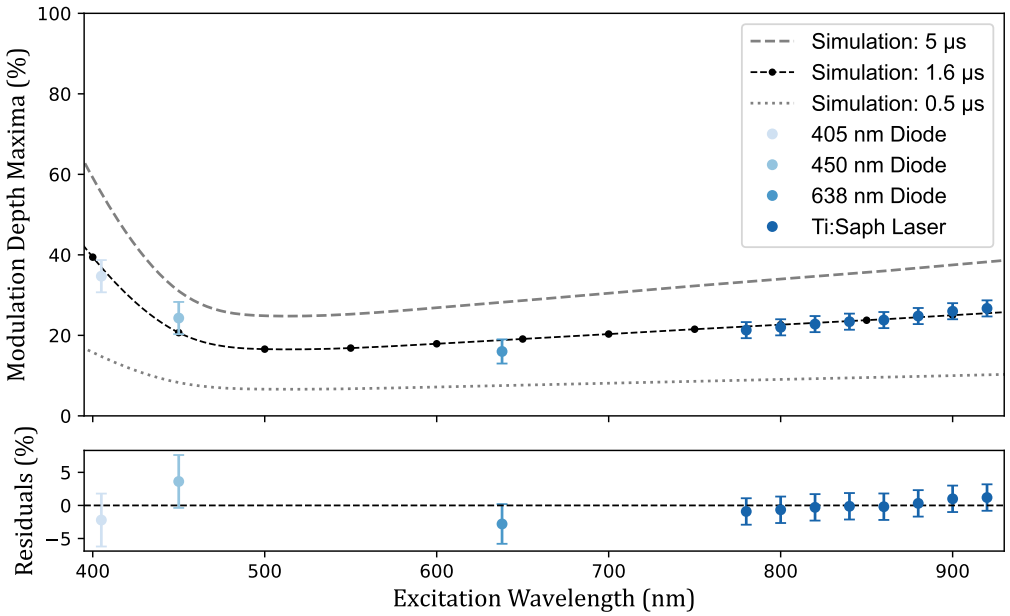

Figure 5.7: A comparison of simulated (5 µs, 1.6 µs, and 0.5 µs effective carrier lifetime simulations) and experimental data for excitation laser wavelengths against modulation depth maxima for an uncoated pure silicon sample (resistivity of 5000 Ω cm, thickness of 480 µm) demonstrating the excitation wavelength dependence of silicon's modulation effects

on silicon's optical properties under varying excitation wavelengths.

Understanding this wavelength-dependent modulation effect is essential for designing silicon-based THz modulators, as it provides insight into selecting the most effective excitation conditions for a given application. In our case, effective choices for excitation wavelength would be with diodes producing 400 nm radiation given this produces the most efficient modulation depth values.

The real and imaginary refractive index values used in the simulation, **Equation 2.5**, come from a database that covered samples similar to our setup [172]. This database is for a silicon sample with 10^{14} carriers, whereas our sample would be in the lower range of 10^{13} carriers. While this represents an order of magnitude difference, the anticipated impact on the refractive index is minimal within the spectral regions of interest.

Between 400 and 700 nm, the optical response of silicon is primarily governed

by interband electronic transitions, which are largely independent of free carrier concentration. Since free carrier absorption plays a relatively minor role in this range, variations in carrier density have only a negligible effect on the real part of the refractive index [173].

In the near-infrared range (700–900 nm), free carrier absorption significantly influences the imaginary component of the refractive index. According to the Drude model, this absorption is proportional to free carrier concentration. However, the effect remains relatively small, as intrinsic silicon properties dominate absorption over extrinsic doping in this range [174]. Therefore, the database refractive index values provide a reasonable approximation for our simulation, with only minor deviations expected, mainly due to reduced free carrier absorption in the near-infrared region.

These refractive index values impact the sample's absorption coefficient and reflectivity. These values were defined for use in **Equations 2.5** and **2.6**. Considering the changes in photon energy, and their respective penetration capabilities from the samples absorption and reflection characteristics, we can begin to understand the complex behaviour we witness in **Figure 5.7**.

The minimum modulation depth at 500 nm indicates a competition between optical penetration and carrier generation efficiency. Shorter wavelengths (400 nm) generate high carrier density in a thin region, while longer wavelengths (900 nm) penetrate deeper, increasing free-carrier absorption. The 500 nm inflection point likely marks a transition where carrier generation per unit depth becomes suboptimal due to changes in reflectivity and absorption.

Carrier lifetime adjustments were made to fit the simulation to experimental data. Generated carriers have lifetimes influenced by diffusion and recombination, with these limiting factors captured through lifetimes assigned to various recombination processes. These processes collectively make up the bulk carrier lifetime (τ_{bulk}), defined in **Equation 2.16**. Adjusting the bulk carrier lifetime adjusts the

recombination and diffusion processes, and therefore the overall number of generated carriers. These changes to net carrier concentration ultimately change the modulation depth as witnessed in **Figure 5.6**.

Additional surface passivation alters surface recombination velocities, significantly impacting the total effective carrier lifetime (τ_{eff}). Ultimately, this dictates the difference between excited and intrinsic states as $\frac{1}{\tau_{\text{eff}}} = \frac{1}{\tau_{\text{bulk}}} + \frac{2S}{d}$, where S is surface recombination velocity, and d is sample thickness. Therefore, adjusting the effective carrier lifetime in the simulation allows a single parameter to tune the trends for optimal fitting.

An effective carrier lifetime of 1.6 µs produced the best-matching trend line. While the exact lifetime was not experimentally determined, the high-resistivity, unpassivated sample suggests a bulk recombination lifetime within the range of 100 µs to 1 ms [175]. The unpassivated surface will have a surface recombination velocity in the range of 10^3 cm/s to 10^6 cm/s [176]. This distortion shifts the anticipated effective carrier lifetime to 0.025–25 µs. The analysis confirms that the chosen lifetime qualitatively aligns with experimental data and fits the expected theoretical range.

The error bars were obtained from uncertainty in the laser power and beam waist. Measurements for the ratio of the elliptical beam's semi-major and semi-minor axes (88%, 88%, 92% and 94% for 405 nm, 450 nm, 638 nm, and Ti:Sapphire lasers respectively) lead to error in the relative beam radius (6%, 6%, 4.2%, and 3% respectively). This radial error leads to error in the total beam area (12%, 12%, 8.4%, and 6% respectively, computed by doubling the radial error), and consequentially an error in the beam intensity. From **Figure 5.6** we can now estimate the equivalent error in modulation depth from this estimated error in excitation intensity (4.3%, 4.3%, 3.1%, and 2% respectively).

Considering the error bars, the simulation trend aligns with experimental data but requires a 50 K increase in silicon temperature during excitation. This heating,

expected from high-power laser excitation, affects carrier mobility, slightly reducing the expected modulation depth output compared to the no-heating case. Furthermore, the residual analysis of **Figure 5.7** indicates a slight deviation of modulation depth in the simulation at 400-500 nm and a minor variance at 900 nm. This discrepancy could arise from factors such as imperfect optical alignment, variations in carrier diffusion assumptions, or temperature-dependent mobility effects not fully captured in the model.

The experimental alignment with the simulation confirms the model accurately captures THz modulation physics. The qualitative agreement supports the theoretical framework, particularly wavelength-dependent absorption and carrier dynamics. However, slight residual disparities suggest the need for further investigation into factors affecting real-world performance.

5.5 Conclusion

In summary, this chapter has provided a detailed characterisation of silicon samples used in designing our THz spatial light modulator. Significant findings emerged from the careful analysis of sample impurities, structural defects, and the advantages offered by employing the HRFZ method. EDS analysis confirmed the high purity of the silicon samples, detecting no substantial impurities that could degrade device performance. TEM and STEM imaging analyses provided assurance regarding the crystalline integrity of the samples, revealing minimal defect densities and attributing observed anomalies primarily to preparation artefacts rather than inherent defects.

The examination of etalon effects underscored the importance of sample thickness and wafer tilt as crucial parameters influencing THz interference patterns. Experimental results, supported by robust simulations, confirmed that precise control over these parameters allows effective tuning of the FSR, enabling fine adjustments in the positions of interference maxima. This ability is particularly valuable in op-

timising the device's performance for specific operational frequencies, enhancing modulation efficiency and contrast.

The modulation effects analysis highlighted the significant influence of optical excitation intensity and wavelength on THz signal modulation depth. Increasing excitation intensity consistently enhanced modulation depth across various THz frequencies, albeit with slight diminishing returns due to recombination and saturation effects at higher intensities. The study of excitation wavelength revealed a complex, non-monotonic relationship, indicating optimal modulation performance at specific wavelengths—particularly around 400 nm—due to the balance between optical absorption, carrier diffusion, and recombination dynamics. However, it should be noted that due to limitations on potential lasers capable of adequate excitation around 400 nm, limited data has been collected to verify this relationship. In future work, additional depth into this region of wavelength dependent modulation depth should be explored.

Collectively, these results provide critical insights into material and operational parameters that define the performance of silicon-based THz modulators. The findings confirm that best modulation depths occur at certain THz frequencies and under specific excitation wavelengths, guiding future designs and optimisations of advanced THz modulation systems.

Chapter 6

Terahertz Imaging Application

In this chapter, we begin by discussing the THz imager, covering its background theory of operation which we touched upon in **Chapter 3**. The modulator, whose design directly embodies the modulation depth predictions from **Chapter 2** with carrier-induced refractive index changes modelled via the continuity equation (**Equation 2.18**), is then used in tandem with the THz imager for characterisation of the modulator in terms of its achievable modulation depth, resolution, and frame rate.

6.1 The Terahertz Imager

The THz imaging system utilises a Caesium vapour typically heated to between 40 and 60°C, where atoms are excited to a Rydberg state. In this system, incident THz radiation interacts with the excited atomic vapour, leading to THz-to-optical conversion. The resulting green fluorescence is then imaged using an optical camera. This approach yields a full-field, real-time imaging system that has been demonstrated to achieve near diffraction-limited spatial resolution and capture images at kilohertz frame rates. The following sections detail the theory behind this phenomena and the specific performance parameters of the imager.

6.1.1 Background Theory

The imager operates by converting THz radiation into a readily detectable optical signal of 535 nm through a carefully designed atomic vapour system, utilising a three-step laser excitation scheme and two distinct Rydberg states in Caesium. This approach enables full-field imaging with diffraction limited resolution and high sensitivity.

Initially, a Caesium vapour is contained within a quartz cell heated to approximately 50°C, which increases the vapour pressure and thereby the atomic density. Three lasers are then employed in sequence to excite the Caesium atoms from their ground state into a specific Rydberg state. The process begins with the first laser, operating at 852 nm, which excites atoms from the ground state ($6S_{1/2}$) to an intermediate excited state ($6P_{3/2}$). This step is critical since it sets the stage for subsequent excitations by efficiently promoting a significant fraction of atoms to an accessible excited level.

The second laser, with a wavelength of 1470 nm, then transfers these atoms from the $6P_{3/2}$ state to another intermediary state, the $7S_{1/2}$ level. The stability and precise tuning of this coupling laser are imperative, as it ensures that the energy of the atoms is correctly prepared for the final excitation. Finally, the third laser, typically operating at 843 nm (referred to as the Rydberg laser), excites the atoms further from the $7S_{1/2}$ state into a high-lying Rydberg state, specifically the $14P_{3/2}$ state. At this juncture, a two-dimensional sheet of excited atoms is formed within the cell.

Even in the absence of incident THz radiation, the atoms in the $14P_{3/2}$ state are not permanently stable. They undergo spontaneous decay via a range of different pathways, producing a background level of fluorescence known as the "THz-off" signal. This fluorescence is inherently broadband, as the decay routes involve multiple transitions that emit at various wavelengths. Consequently, the initial optical signal without the influence of a THz field comprises a mixture of wavelengths

corresponding to the different decay channels from the $14P_{3/2}$ state.

When a continuous-wave THz field at 0.55 THz is applied to the excited vapour, it resonantly couples the $14P_{3/2}$ state to a neighbouring Rydberg state—the $13D_{5/2}$ state. For reference, at 550 GHz, the free-space wavelength is approximately 545 µm ($\lambda = c/f$). This wavelength represents the relevant spatial scale for diffraction and imaging constraints in the THz regime." The incident THz radiation essentially provides the energy needed to induce this transition. Unlike the spontaneous decay from the $14P_{3/2}$ state, this THz-induced transition channels the atoms into the $13D_{5/2}$ state where the decay occurs primarily through a cascade involving an intermediate state (generally the $6P_{3/2}$ state) before returning to the ground state. The key point here is that this cascade predominantly produces a narrow-band optical emission, with most photons emitted at 535 nm, a distinct green fluorescence. This particular fluorescence, called the "THz-on" signal, is markedly different from the broadband "THz-off" fluorescence.

To distinguish between these two cases, the imager employs a narrow-band optical filter centred on 535 nm. This filter effectively isolates the green fluorescence originating from the THz-coupled $13D_{5/2}$ decay pathway and suppresses the broader background fluorescence from the unperturbed $14P_{3/2}$ state. The resulting image, captured by a conventional optical camera, directly maps the spatial distribution of the incident THz field.

In summary, the imager utilises a three-step laser excitation scheme to prepare the Caesium vapour in the $14P_{3/2}$ Rydberg state, which exhibits spontaneous decay (broadband fluorescence) in the absence of THz radiation. When exposed to a resonant THz field, the atoms transition to the $13D_{5/2}$ state and decay predominantly via a cascade that produces distinct green fluorescence at 535 nm, thus allowing selective and high-speed imaging of the THz field.

6.1.2 System Capabilities

The THz imaging system demonstrates near diffraction-limited spatial resolution, as evidenced by imaging experiments performed by Dr. Downes [6] that resolved 0.50 mm diameter pinholes spaced 1.00 mm apart. Analysis of the resulting Airy patterns and the corresponding Strehl ratio of 0.57 confirms that the optical design, while affected by some aberrations, achieves resolution close to the theoretical diffraction limit. This performance is a testament to the efficient optical collection and the precision of the in-house designed optical elements used in the system.

Temporal resolution is equally admirable, with the imager capturing images at frame rates up to 6 kHz. In dynamic experiments, such as those involving the motion of a water droplet and a rotating optical chopper wheel, the system demonstrated the ability to record high-speed events reliably. Although the intrinsic lifetime of the THz-coupled excited state is around 0.8 µs—suggesting the possibility of imaging at even higher speeds—the practical frame rate is limited by the sensitivity of the optical camera. In the testing configuration, the FASTCAM detector provided high-speed imaging with a signal-to-noise ratio that remained acceptable up to 6 kHz, beyond which the signal-to-noise ratio dropped to approximately 2.

Sensitivity is another key capability of the imager. The minimum detectable THz power was quantified as (190 ± 30) femtowatts per 40×40 µm² pixel over a 1-second integration period. This high sensitivity is achieved by efficient THz-to-optical conversion, where each absorbed THz photon has a conversion probability of roughly 52.4% into a detectable optical photon. The system's sensitivity was determined through calibration using the Andor iXon camera, where the incident THz power was calculated by assuming a Gaussian beam profile for the THz source and accounting for losses incurred in the optical setup. With a THz source output of approximately 17 µW at 0.55 THz, only a fraction of this power is focused onto the active imaging area.

The full-field imaging capability, which allows the collection of a 2D image in

a single shot, further enhances the practicality of the system. Unlike conventional single-pixel or raster scanning systems, this approach enables real-time imaging without the need for scanning procedures. Moreover, the optical detection method allows for flexibility in the choice of cameras, which could further improve performance if more sensitive detectors are employed in future iterations.

6.2 Modulator Characterisation

Although the THz modulator being designed in this work is primarily developed for implementation into the THz imager, it is possible to use the imager to initially characterise the modulator instead. The following sections cover the characterisation of the modulator in terms of captured image contrast, resolution, and frame rate capabilities for the chosen design.

6.2.1 Image Contrast

In typical operation, the processing of images from the THz imager is performed by comparison of 'THz field-off' vs 'THz field-on' images. This is essentially comparisons of the images whose signals contain just background noise, and background noise with the addition of the THz signal respectively. By performing a subtraction of 'off' from 'on', it enables the reduction of noise from the produced THz image.

The addition of the THz modulator to the setup further complicates the processing as additional factors of silicon interference from absorption of the THz, and effects of masked excitation on the THz transmission both add to the aforementioned signal compositions. A comprehensive diagram of all four imaging stages (background signal (THz field-off), Terahertz field (THz field-on), wafer inserted, and modulation activated) are shown in **Figure 6.1** ***a)*** along with their corresponding signal compositions in **Figure 6.1** ***b)***.

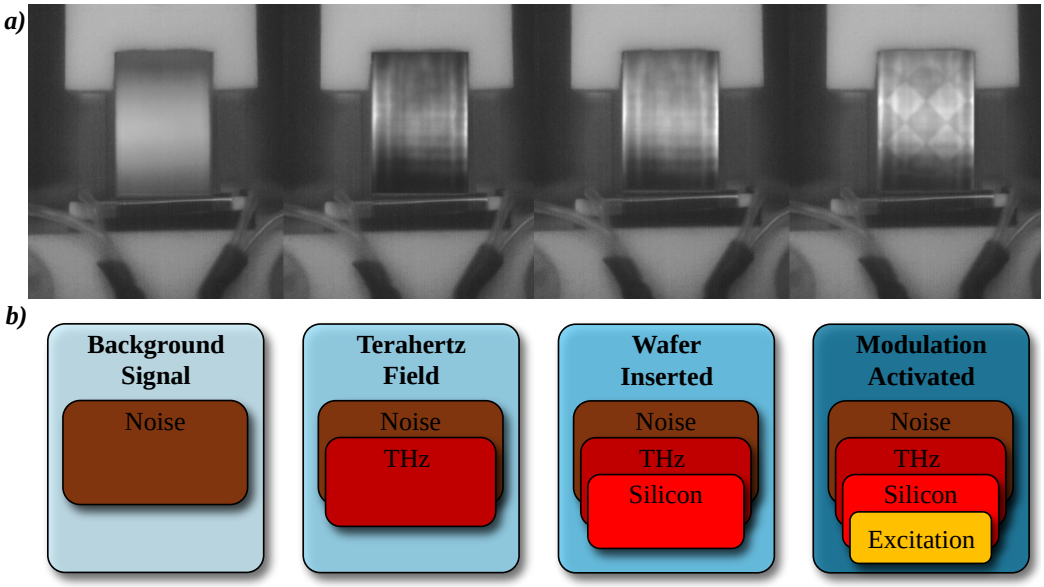

Figure 6.1: ***a)*** Images of the Caesium vapour cell optical fluorescence. From left to right, the images depict the cell during imaging of the background signal, then the application of the THz field, then the addition of a silicon wafer in the THz field path, and finally the addition of a checkerboard excitation mask to the silicon (applying modulation). ***b)*** The four stages of imaging (from ***a)***) and their signal compositions. From left to right, the diagram depicts the progressive addition of background noise, THz signals, silicon interferences, and the modulation via masked excitation to the signal.

In this new setup's typical operation, the silicon wafer will remain in position rather than being removed for the capture of the background and terahertz field images. This leaves a comparison between the wafer inserted and modulation activated images. As seen in **Figure 6.1** ***b)***, the remaining signal composition after processing between these two images will be the signal induced by the excitation process (modulation). Therefore a comparison of this nature directly allows for the extraction of the modulation process's influence upon the THz field.

Figure 6.2 shows the modulation depth calculated by taking the difference between the modulation activated and wafer inserted images then normalising against the modulation activated image. To enhance the signal to noise even further for visibility, horizontal profiles of the modulated image are taken and then averaged vertically across the entire height of the image. This produces fairly clear triangular peaks where the apices correspond to the centres of the modulated

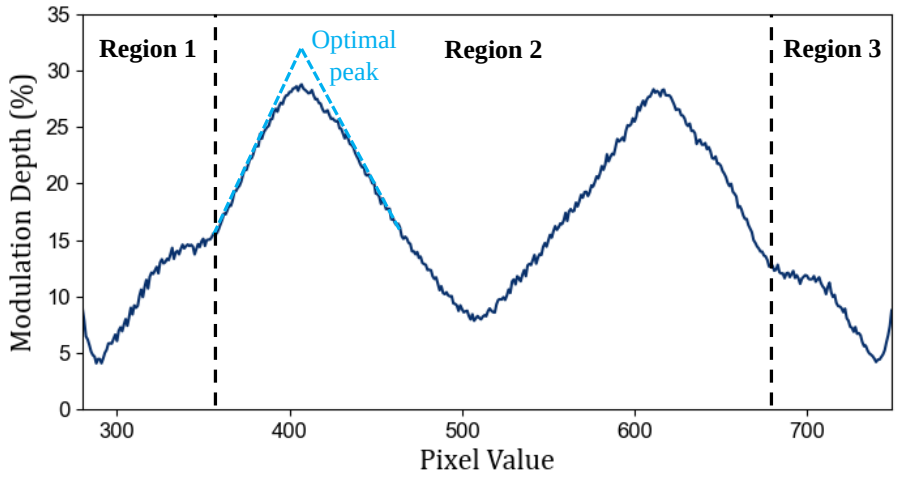

Figure 6.2: The modulation depth for an example checkerboard pattern tested in the THz imager. Horizontal profiles of the modulated pattern are taken then averaged vertically across the entire image. The peaks therefore correspond to the centres of the checkers. A theoretical optimal peak without the effects of lateral diffusion is shown for comparison, and the experimental data is split into three regions where regions 1 and 3 denote anticipated vapour cell interference while region 2 depicts optimal modulation and imager performance.

THz, and the troughs correspond to the points at which the concurrent illuminated checker boarders meet.

To determine the contrast, the Modulation Transfer Function (MTF) for contrast can be used which is defined as

$$MTF = \frac{I_{max} - I_{min}}{I_{max} + I_{min}}, \tag{6.1}$$

where I_{max} and I_{max} are the maximum and minimum intensities respectively from **Figure 6.2**. These values from the peaks and troughs of 29% and 8% respectively shows that the relative contrast achieved in the image is 0.568. This is a relatively low modulation depth compared to other existing THz modulators which can reach 99%. The limiting factor for this comes from the silicon wafer as discussed in **Chapter 5** for which alternatives should be looked for in future work to improve this design. In addition to weakened modulation depth capabilities, lateral diffusion effects can also be seen when comparing the shape of the 'blunt' profile with that of the optimal peak. This dullness will originate from a imperfect step function

between checkers caused by diffusion effects smoothing out the step and will lead to further reductions in the MTF contrast.

In regions 1 and 3 of the profile, anomalies are introduced onto the familiar triangle profile. These anomalies are not present within region 2 of the profile, therefore are likely to originate from interference with the edges of the vapour cell. As these interference effects are anticipated to be due to components within the imaging setup, we can conclude that they are not due to issues within the design of the modulator.

6.2.2 Spatial Resolution

The method for determining the spatial resolution involves using a series of images of these checkerboard patterns with progressively smaller check sizes to evaluate the capabilities of the THz modulator. Since the THz imager can be assumed to have optimal resolution, any deterioration in contrast in these images is primarily due to the modulator's performance. By plotting the contrast against the checker size, we can observe how well the modulator is reproducing the pattern details.

As the checker size decreases, the modulator's finite resolution means it can no longer accurately reproduce the sharp transitions between the dark and light areas of the pattern. This inability results in a reduction of the contrast in the images. At a certain point, the contrast will drop below a predefined threshold, which is taken as the minimum contrast required to reliably resolve the pattern. The checker size at which this occurs is then considered the minimum resolvable resolution of the modulator.

Typically, the predefined threshold is 50% however, this would likely not result in a fair comparison. A modulator with higher modulation depth would likely achieve better resolution from this threshold value despite also being constituted mainly of silicon. As discussed in **Chapter 2**, the limiting factor for resolution comes from lateral diffusion of charge carriers which is an intrinsic mechanism

to silicon, therefore it would be reasonable to expect modulators build upon the same silicon wafer design to have comparable resolution. To correct for this, the predefined threshold of 50% has been normalised to our maximum achievable modulation depth to give a value of 14.5% as the threshold. This should ensure that modulator's limited modulation depth does not impact its resolution unreasonably.

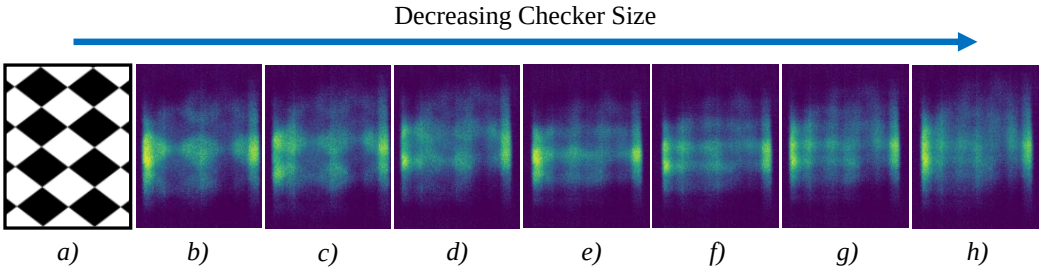

Figure 6.3: A series of modulated and imaged checkerboard patterns of decreasing checker size from ***b)*** though to ***h)***, with ***a)*** being an example checkerboard to assist with visualising the pattern. The checker sizes for each image are: ***b)*** 960 µm, ***c)*** 850 µm, ***d)*** 740 µm, ***e)*** 620 µm, ***f)*** 510 µm, ***g)*** 400 µm, ***h)*** 290 µm.

Figure 6.3 depicts the series of modulated checkerboard images collected with decreasing checker size. With visual inspection, and the help of **Figure 6.3** ***a)***, it should be possible to discern the checkers by eye in the majority of the images. It should be noted that the images have been adjusted to better highlight the contrast using two techniques. Firstly, the greyscale image has been converted to a high contrast colour map to enable better deduction between light and dark areas. And secondly, the colour map has been normalised to ensure that the darkest and lightest regions correspond to the extreme ends of the colour map respectively.

Performing the contrast analysis from **Equation 6.1** across each of the images in **Figure 6.3** produces the MTF plot seen in **Figure 6.4**. There is a clear trend across the MTF values whereby decreasing checker size leads to decreasing contrast. An exponential decay curve has been fitted to the data to interpolate between the data points, and error values for the data points are collected from repeated runs of checkerboard sizes and their standard deviations. Now using the threshold value, set to 14.5% as previously discussed, the exponential curve intersection suggests

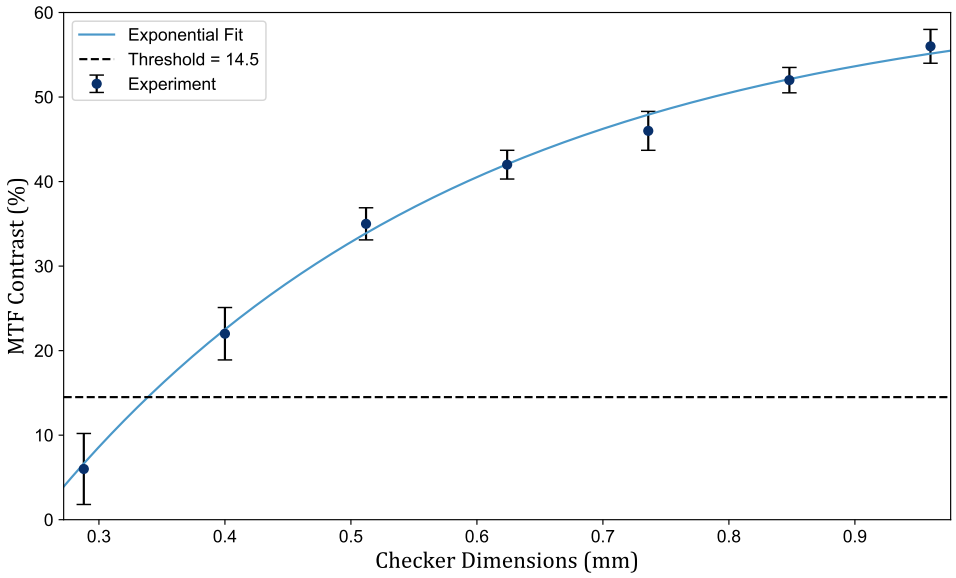

Figure 6.4: An exponential fitting to experiment data collected for a range of checkerboard dimensions depicting the change in MTF contrast values and the intersection with the predefined minimum resolvable threshold of 14.5% at 340 µm.

that the minimum resolvable resolution of this designed modulator is approximately 340 µm. This corresponds to **Figure 6.3 *g*)** being the last resolvable checkerboard pattern with **Figure 6.3 *h*)** being unresolvable.

When comparing this modulator design with a maximum modulation depth of only 29% to others with higher modulation depths, the resolution is found to be quite similar as typical values for other similar systems tend to be in the range of 140-500 µm [177]. This is because the limiting factor is not the modulation depth itself but the lateral spreading of the photoexcited carriers. Thus, even if a device design can only achieve low modulation depth, its resolution limit – defined by the minimum feature size that remains distinguishable – still falls within the range of several hundred micrometres. The measured resolvable resolution is also along the lines of the diffraction limitations of the THz imager in use, suggesting that the current design is at least compatible up to the limitations imposed by the imager [6].

When empirically exploring theoretical resolution limits from **Equation 2.17**

using the calculated effective carrier lifetime from **Chapter 5**, the diffusion length is expected to be on the order of 10 µm. This is considerably smaller than the 340 µm attained experimentally. The reason for this comes from the THz diffraction limits imposed by the THz imaging setup whereby the greater resolution achievable by the silicon is not fully realised by the current imager setup.

6.2.3 Frame Rate

In order to achieve practical THz modulation for real-time imaging, the spatial light modulator must be capable of rapid, repeated switching. The expected maximum operational frame rate is determined by two primary limitations: the refresh rate of the DMD, and the recombination lifetime of photoexcited charge carriers in the silicon wafer. As demonstrated in **Chapter 5**, the high-resistivity float-zone silicon used in this work exhibits sub-microsecond carrier lifetimes under moderate to high excitation intensities.

The DMD device employed supports pattern switching rates exceeding 10 kHz, enabling dynamic optical patterning of the silicon surface. Provided that carrier recombination occurs within comparable or shorter timescales, the modulator is expected to respond dynamically to each DMD refresh cycle, avoiding charge accumulation, latency, or image smearing [178]. This sets the upper bound on frame rate operation.

However, from a theoretical standpoint, increasing the frame rate also reduces the total exposure time of the silicon to each excitation pattern, thereby decreasing the time available for carrier generation. Under such conditions, the generation rate may not fully replenish the carrier density between cycles, potentially resulting in lower modulation depth. Therefore, it is anticipated that modulation contrast might degrade at higher frame rates due to a reduced carrier population — particularly if carrier lifetime and photon flux are not sufficient to maintain full optical saturation during rapid cycling.

To test this hypothesis, a series of modulation experiments were performed using dynamic checkerboard patterns projected at varying frame rates, from static operation up to 10 kHz. THz transmission images were captured synchronously to assess spatial fidelity and contrast across frames. The modulation depth was measured as a function of pattern rate to determine the maximum frequency at which stable modulation could be sustained.

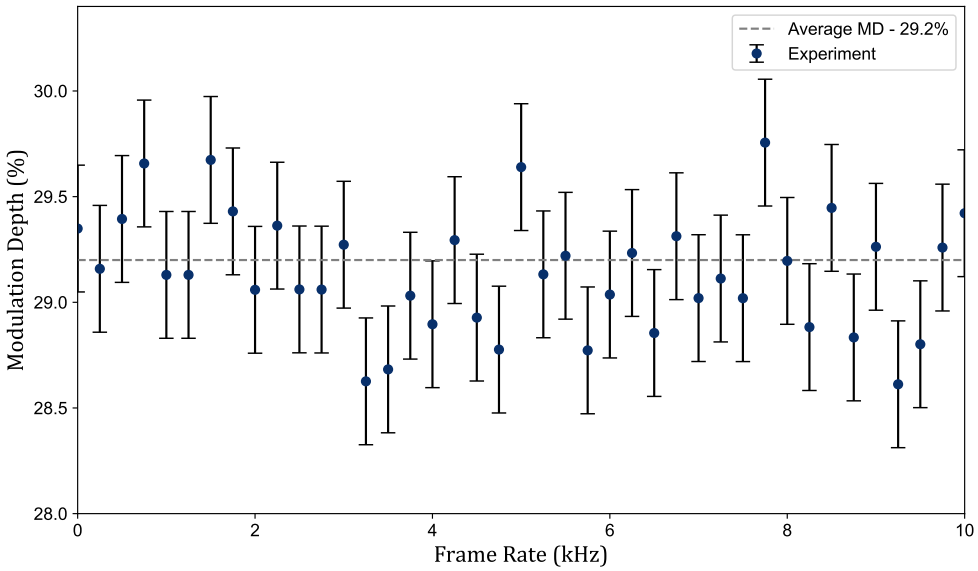

Figure 6.5: Data collected using the Terascan 1550 system for a series of modulator frame rates between 0 and 10 kHz and their corresponding modulation depths.

As shown in **Figure 6.5**, the modulation contrast remained effectively constant across the tested range, with no significant degradation observed up to 10 kHz. This experimental outcome confirms that the carrier dynamics in the silicon sample are fast enough to support repeated high-speed switching with no appreciable loss of contrast. The observed behaviour validates the hypothesis that the system operates within the bounds set by the DMD's refresh capabilities and silicon's recombination timescales.

Interestingly, despite theoretical predictions of reduced carrier density at shorter exposure times, the high photon flux and short carrier lifetimes appear sufficient to ensure full carrier replenishment within each modulation cycle. This allows the

modulation depth to be preserved, even under high speed operation.

These results demonstrate that the photoexcited silicon modulator is capable of operating at real-time video frame rates — a critical requirement for practical THz imaging applications. The ability to maintain modulation contrast at 10 kHz confirms that the combination of high-speed optical patterning and fast carrier dynamics in silicon results in a spatial modulator well-suited to rapid THz imaging, including dynamic materials characterisation and security screening scenarios.

6.3 Conclusion

The spatial selectivity achieved through DMD projection in **Chapter 4**, paired with the THz imager enabled validation of the theoretical resolution limits imposed by the diffusion length, derived in **Equation 2.17**. From imaging of the modulator, we determined a maximum modulation depth capability of 29%, limited by the silicon surface recombination properties discussed in **Chapter 5**. Additionally, imaging of a variety of checkerboard patterns suggests the minimum resolvable resolution for this particular design is approximately 340 µm, which corresponds to approximately 0.62λ at the operational frequency of 550 GHz. This resolution approaches the theoretical diffraction limit, supporting the effectiveness of the modulator in high-fidelity THz imaging. This also shows that despite the lower modulation depth capability, the resolution remains high near the diffraction limit. Finally, analysis of dynamic changes shows the design is capable of frame rates along the order of that imposed by the DMD.

For typical HRFZ silicon wafers used in THz modulation, longer-lifetime wafers can, in ideal conditions, achieve modulation depths exceeding 50–60%, particularly when paired with high-intensity optical excitation. By contrast, our wafer with a lower anticipated lifetime of 1.6 µs only supports a lower maximum modulation depth, under similar high pump fluence and wafer thickness. While this is still substantial for many applications, particularly in imaging and dynamic field mapping,

it is not optimal for goals such as ultra-high contrast modulation.

However, in terms of spatial resolution, the carrier lifetime has a less direct but still important role. A longer lifetime allows carriers to diffuse farther before recombining, which reduces spatial sharpness and can blur fine features in time-resolved THz images or patterned modulators. A 1.6 µs lifetime suggests little diffusion, thereby retaining relatively good spatial resolution compared to very long-lifetime wafers, matching the result of 340 µm diffraction limited resolution found. This is advantageous for applications requiring high spatial fidelity, such as THz near-field imaging or holography. Therefore, by balancing reasonable contrast typical of long-lifetime silicon, and the better resolution and frame rate capabilities of short-lifetime silicon, this design becomes well suited for integration into the THz imager which relies on its high resolution and frame rate capabilities.

Chapter 7

Summary and Outlook

This thesis has presented a comprehensive investigation into the design, fabrication, and characterisation of a novel spatial THz light modulator. This work was motivated by the persistent challenges associated with the so-called "THz gap" and the need for efficient, high-speed modulation devices that can be seamlessly integrated into advanced THz imaging systems. In summary, the research has addressed key limitations in modulation speed, efficiency, and device integration by utilising innovative approaches rooted in semiconductor photoexcitation and digital micromirror technology.

In **Chapter 1**, an extensive overview of THz technology was provided, placing the work within the broader context of electromagnetic research and its manifold applications. It was demonstrated that the unique properties of THz radiation – its non-ionising nature, ability to penetrate non-metallic materials, and the associated spectroscopic capabilities – make it a valuable tool for applications ranging from medical diagnostics and security screening to non-destructive testing in industrial settings. Nonetheless, the limitations inherent in conventional electronic and photonic systems have long hindered the exploitation of this spectral region, thereby motivating the pursuit of alternative modulation strategies.

The theoretical underpinnings of the THz modulator were rigorously developed in **Chapter 2**. A detailed framework was established by analysing silicon's elec-

tronic properties, particularly its indirect band gap, charge carrier dynamics, and recombination mechanisms. The application of the Drude model, along with plasma frequency analysis and the derivation of the complex dielectric function, provided a robust basis for understanding how photoexcitation influences the electro-optical properties of silicon. These theoretical insights not only informed the design of the modulator but also later facilitated quantitative predictions of modulation depths under varying excitation conditions.

Chapter 3 described the experimental methodologies and procedures that were central to this investigation. Advanced fabrication techniques – including High Resistivity Float Zone (HRFZ) wafer production, Focused Ion Beam (FIB) milling and Transmission Electron Microscopy (TEM) – were employed to prepare and analyse the high-purity silicon wafer. The integration of a Digital Micromirror Device (DMD), characterised in **Chapter 4**, allowed for the spatially resolved projection of dynamic optical patterns onto the silicon substrate. This, in turn, enabled localised photoexcitation, resulting in a reconfigurable modulator capable of dynamically altering THz wave propagation. Detailed assessments of resolution, frame rate, and power efficiency were undertaken, and the experimental results were corroborated by simulation data, thus confirming the efficacy of the modulator design.

Chapter 5 was dedicated to the in-depth characterisation of silicon, emphasising its suitability for THz modulation. Systematic analyses of wafer resistivity, carrier mobility, and etalon effects provided further insight into how photoexcitation influences the material's optical and electronic properties. This chapter highlighted the delicate interplay between excitation intensity, wavelength, and the resulting modulation depth, establishing a solid experimental foundation on which the modulator's performance could be evaluated and optimised. Importantly, it was found that the silicon wafer in our design likely has an effective carrier lifetime of only 1.6 µs, far shorter than the typical silicon wafer used in THz modulators. Additionally, it was discerned that the shorter lifetime was most likely due to sur-

face recombination states limiting the faster intrinsic effects of the silicon's bulk material.

In **Chapter 6**, the integration of the modulator with a state-of-the-art THz imaging system was explored. The application of the modulator in an imaging context highlighted its theorised capabilities of high resolution near the diffraction limit of 340 µm. Additionally, analysis of frame rate dependence on modulation depth showed that the shorter lifetime silicon achieved remarkably effective performance up to at least 10 kHz in contrast to its longer lifetime counterpart which theoretically would have performed worse. This proof-of-concept study validated the modulator's applicability in real-world imaging scenarios and paves the way for its further refinement.

Looking ahead, several avenues for future work have been identified. One promising direction is the optimisation of the photoexcitation parameters, such as the excitation wavelength and intensity profile, to further increase modulation depths and operational speeds. In addition, the integration of novel semiconductor materials – for example, graphene or indium phosphide – may offer superior charge carrier mobility and tunability, potentially leading to modulators with even higher efficiency and broader bandwidth capabilities than that of the current bare silicon design.

While it was determined that the silicon in this modulator design can achieve diffraction limited resolution and extremely high frame rates, the contrast offered was perhaps lower than ideal. Better balancing of the modulation depth by slightly reducing surface recombination effects would improve the contrast perhaps past 50%, while still ensuring that the modulator achieves near diffraction limit resolution and does not impede the THz imager's fast frame rate capabilities.

Another potential area of exploration is the incorporation of machine learning algorithms to optimise the dynamic patterning provided by the DMD. By utilising intelligent control systems, it may be possible to further enhance the spatial resolu-

tion and frame rate of the modulator by taking advantage of the sub-wavelength resolution potential provided by the DMD. This exploration could therefore broaden the modulator's applicability in high resolution THz imaging and communication systems.

Finally, the translation of this technology from a laboratory prototype to a fully integrated, deployable system remains a significant challenge. Future research should focus on the practical aspects of device packaging, scalability, and robustness under diverse operating conditions. In this context, collaboration with industry partners could facilitate the development of commercially viable THz modulators that meet the rigorous demands of modern applications while also abiding by the intricate component synthesis rules highlighted in this work.

In conclusion, the research presented in this thesis seeks to enhance our understanding in the field of THz modulator design for the purpose of implementation in imaging applications. By successfully integrating advanced material characterisation, innovative fabrication techniques, and state-of-the-art optical modulation strategies, this work not only addresses longstanding technical challenges but also opens new pathways for future technological developments. The insights gained herein provide a solid foundation for subsequent explorations, and the proposed future directions offer a clear roadmap for achieving even greater advancements in THz technology.

Bibliography

[1] P. H. Siegel *et al.*, 'Terahertz technology,' *IEEE Transactions on Microwave Theory and Techniques*, vol. 50, no. 3, pp. 910–928, 2002.

[2] P. U. Jepsen, D. G. Cooke and M. Koch, 'Terahertz spectroscopy and imaging–modern techniques and applications,' *Laser & Photonics Reviews*, vol. 5, no. 1, pp. 124–166, 2011.

[3] R. Degl'Innocenti *et al.*, 'All-integrated terahertz modulators,' *Nanophotonics*, vol. 7, no. 1, pp. 127–144, 2018.

[4] H. T. Chen *et al.*, 'Active terahertz metamaterial devices,' *Nature*, vol. 444, no. 7116, pp. 597–600, 2006.

[5] K. Fan *et al.*, 'Dynamic electromagnetic metamaterials,' *Optica*, vol. 2, no. 6, pp. 532–537, 2015.

[6] L. Downes, 'A high-speed THz imaging system based on THz-to-optical conversion in atomic vapour,' Ph.D. dissertation, Durham University, 2020.

[7] D. M. Mittleman, 'Twenty years of terahertz imaging,' *Optics Express*, vol. 26, no. 8, pp. 9417–9431, 2018.

[8] J. W. Haus, K. Moloni and N. J. Halas, 'Enhanced tunable terahertz generation in photonic band-gap structures,' *Laser Physics*, vol. 14, no. 5, pp. 635–642, 2004.

[9] M. Tonouchi, 'Cutting-edge terahertz technology,' *Nature Photonics*, vol. 1, no. 2, pp. 97–105, 2007.

[10] B. Ferguson and X. C. Zhang, 'Materials for terahertz science and technology,' *Nature Materials*, vol. 1, no. 1, pp. 26–33, 2002.

[11] D. M. Mittleman, *Sensing with Terahertz Radiation*. Springer, 2013.

[12] Y. C. Shen *et al.*, 'Terahertz pulsed spectroscopy and imaging,' *Philosophical Transactions of the Royal Society of London A: Mathematical, Physical and Engineering Sciences*, vol. 362, no. 1815, pp. 2039–2057, 2005.

[13] A. K. Panwar, D. Kumar and S. Tripathi, 'Terahertz imaging system for biomedical applications: Current status,' *System*, vol. 28, p. 44, 2013.

[14] H. Kitahara *et al.*, 'Application of THz imaging for medical diagnostics,' in *International Quantum Electronics Conference, 2005.*, IEEE Computer Society, 2005, pp. 1238–1239.

[15] M. Dick *et al.*, 'Collisional cooling investigation of THz rotational transitions of water,' *Physical Review A—Atomic, Molecular, and Optical Physics*, vol. 81, no. 2, p. 022 706, 2010.

[16] A. Virk *et al.*, 'Design and characterization of a single-pixel imaging system using double hyperbolic-elliptical objective lens for THz spherical scanning of cornea with a large field-of-view,' in *Advanced Biomedical and Clinical Diagnostic and Surgical Guidance Systems XXI*, SPIE, vol. 12368, 2023, pp. 89–95.

[17] S. Shur *et al.*, 'Biomedical applications of terahertz technology,' in *Advances in Terahertz Biomedical Imaging and Spectroscopy*, SPIE, vol. 11975, 2022, p. 1 197 502.

[18] B. Clough, J. Dai and X.-C. Zhang, 'Laser air photonics: Beyond the terahertz gap,' *Materials Today*, vol. 15, no. 1-2, pp. 50–58, 2012.

[19] A. Krotkus, 'Semiconductors for terahertz photonics applications,' *Journal of Physics D: Applied Physics*, vol. 43, no. 27, p. 273 001, 2010.

[20] B. S. Williams, 'Terahertz quantum-cascade lasers,' *Nature Photonics*, vol. 1, no. 9, pp. 517–525, 2007.

[21] S. Lepeshov *et al.*, 'Enhancement of terahertz photoconductive antenna operation by optical nanoantennas,' *Laser & Photonics Reviews*, vol. 11, no. 1, p. 1 600 199, 2017.

[22] M. Jazbinsek, M. Zidan and P. Günter, 'Organic crystals for THz photonics,' *Applied Sciences*, vol. 9, no. 5, p. 882, 2019.

[23] R. Köhler *et al.*, 'Terahertz semiconductor-heterostructure laser,' *Nature*, vol. 417, no. 6885, pp. 156–159, 2002.

[24] P. Jeunesse, E. Freysz and P. L. Richards, 'Ultrafast pulsed terahertz sensing for process monitoring and industrial imaging,' in *11th European Conference on Non-Destructive Testing*, 2014.

[25] M. Strąg *et al.*, 'Application of terahertz radiation in non-destructive testing of military-designated composite materials,' *Problemy Mechatroniki: uzbrojenie, lotnictwo, inżynieria bezpieczeństwa*, vol. 14, no. 4, p. 54, 2023.

[26] E. Pickwell and V. P. Wallace, 'Biomedical applications of terahertz technology,' *Journal of Physics D: Applied Physics*, vol. 39, no. 17, 2006.

[27] R. M. Woodward *et al.*, 'Terahertz pulse imaging of ex vivo basal cell carcinoma,' *Journal of Investigative Dermatology*, vol. 120, no. 1, pp. 72–78, 2003.

[28] T. Globus *et al.*, 'Terahertz fourier transform characterization of biological materials in a liquid phase,' *Journal of Applied Physics*, vol. 93, no. 5, pp. 3217–3221, 2003.

[29] R. A. Lewis, 'A review of terahertz sources,' *Journal of Physics D: Applied Physics*, vol. 47, no. 37, p. 374 001, 2014.

[30] J. F. Federici *et al.*, 'THz imaging and sensing for security applications—explosives, weapons and drugs,' *Semiconductor Science and Technology*, vol. 20, no. 7, 2005.

[31] R. Appleby and H. B. Wallace, 'Standoff detection of weapons and contraband in the 100 GHz to 1 THz region,' *IEEE Transactions on Antennas and Propagation*, vol. 55, no. 11, pp. 2944–2956, 2007.

[32] T. D. Dorney, R. G. Baraniuk and D. M. Mittleman, 'Material parameter estimation with terahertz time-domain spectroscopy,' *Journal of the Optical Society of America A*, vol. 18, no. 7, pp. 1562–1571, 2001.

[33] S. L. Dexheimer, *Terahertz Spectroscopy: Principles and Applications*. CRC Press, 2008.

[34] X.-C. Zhang and J. Xu, *Introduction to THz Wave Photonics*. Springer, 2009.

[35] Y. Kabetani *et al.*, 'Terahertz time-domain spectroscopy of water vapor based on asynchronous optical sampling,' in *IEEE: Conference on Lasers and Electro-Optics-Pacific Rim*, 2007, pp. 1–2.

[36] A. Rawson *et al.*, 'Recent advances in terahertz time-domain spectroscopy and imaging techniques for automation in agriculture and food sector,' *Food Analytical Methods*, pp. 1–29, 2022.

[37] G. J. Wilmink and J. E. Grundt, 'Invited review article: Current state of research on biological effects of terahertz radiation,' *Journal of Infrared, Millimeter, and Terahertz Waves*, vol. 32, no. 10, pp. 1074–1122, 2011.

[38] P. Emilien, J.-M. Manceau and G. Ducournau, *Fundamentals of terahertz devices and applications*. Wiley, 2021, vol. 46071, pp. 978–1119.

[39] M. Nagel *et al.*, 'THz technology for label-free genetic diagnostics,' in *IEEE Lasers and Electro-Optics Society*, vol. 1, 2002, p. 3.

[40] Y. C. Shen *et al.*, 'Detection and identification of explosives using terahertz pulsed spectroscopic imaging,' *Applied Physics Letters*, vol. 86, no. 24, p. 241 116, 2005.

[41] N. Palka *et al.*, '3d non-destructive imaging of punctures in polyethylene composite armor by THz time domain spectroscopy,' *Journal of Infrared, Millimeter, and Terahertz Waves*, vol. 36, pp. 770–788, 2015.

[42] R. Stantchev *et al.*, 'Real-time terahertz imaging with a single-pixel detector,' *Nature communications*, vol. 11, no. 1, p. 2535, 2020.

[43] A. Iacono *et al.*, 'Focal plane arrays for THz imaging,' in *2012 6th European Conference on Antennas and Propagation (EUCAP)*, IEEE, 2012, pp. 893–897.

[44] F. Simoens *et al.*, 'Real-time imaging with THz fully-customized uncooled amorphous-silicon microbolometer focal plane arrays,' in *Terahertz Physics, Devices, and Systems Vi: Advanced Applications in Industry and Defense*, SPIE, vol. 8363, 2012, pp. 57–68.

[45] X. Tu *et al.*, 'Microbolometers integrated with diffractive lens for THz imaging,' in *2013 38th International Conference on Infrared, Millimeter, and Terahertz Waves (IRMMW-THz)*, IEEE, 2013, pp. 1–2.

[46] A. Luukanen *et al.*, 'An array of antenna-coupled superconducting microbolometers for passive indoors real-time THz imaging,' in *Terahertz for Military and Security Applications IV*, SPIE, vol. 6212, 2006, pp. 270–278.

[47] Irwin *et al.*, 'Transition-edge sensors,' *Cryogenic particle detection*, pp. 63–150, 2005.

[48] J. Baselmans, 'Kinetic inductance detectors,' *Journal of Low Temperature Physics*, vol. 167, pp. 292–304, 2012.

[49] S. Sheng-Cai, 'Superconducting THz detectors and their applications in radio astronomy,' *Terahertz Science and Technology*, vol. 1, no. 4, pp. 190–206, 2008.

[50] L. Downes *et al.*, 'A practical guide to terahertz imaging using thermal atomic vapour,' *New Journal of Physics*, vol. 25, no. 3, p. 035 002, 2023.

[51] P. H. Siegel, 'Terahertz technology in biology and medicine,' *IEEE Transactions on Microwave Theory and Techniques*, vol. 52, no. 10, pp. 2438–2447, 2004.

[52] D. Misokefalou, G. Ntogaras and P. P. Polychroniadis, 'Non-destructive testing for quality control in automotive industry,' *Int. J. Eng. Appl. Sci. Technol*, vol. 7, pp. 349–355, 2022.

[53] X. Neiers, S. Haidar and J. Siegel, 'Single shot pulsed terahertz non destructive evaluation systems for in-line production control and automated inspection,' in *11th International Symposium NDT in Aerospace*, 2019.

[54] G. P. Kniffin *et al.*, 'Advances in terahertz time-domain spectroscopy and imaging,' *Philosophical Transactions of the Royal Society A: Mathematical, Physical and Engineering Sciences*, vol. 368, no. 1934, pp. 3015–3033, 2010.

[55] A. Stylianou, G. Alomou and C. P. Halsey, 'Nanotechnology-supported THz medical imaging,' *F1000 Research*, p. 2, 2013.

[56] T. Amini *et al.*, 'A review of feasible applications of THz waves in medical diagnostics and treatments,' *Journal of Lasers in Medical Sciences*, p. 12, 2021.

[57] Y. Sun *et al.*, 'A promising diagnostic method: Terahertz pulsed imaging and spectroscopy,' *World Journal of Radiology*, vol. 3, no. 3, p. 55, 2011.

[58] B. M. Fischer, M. Walther and P. U. Jepsen, 'Far-infrared vibrational modes of DNA components studied by terahertz time-domain spectroscopy,' *Physics in Medicine & Biology*, vol. 47, no. 21, p. 3807, 2002.

[59] D. Markl, G. Braun and D. Zeitler, 'Pharmaceutical applications of terahertz spectroscopy and imaging,' *Eur. Pharm*, vol. 21, no. 4, pp. 45–50, 2016.

[60] M. Kalra, A. Sharma and V. K. Sharma, 'Recent advanced-smarter techniques of analysis,' *International Journal of Pharma Professional's Research (IJPPR)*, vol. 2, no. 2, pp. 238–245, 2011.

[61] M. Naftaly and R. Dudley, 'Industrial applications of terahertz sensing: State of play,' *Sensors*, vol. 19, no. 19, p. 4203, 2019.

[62] M. Rahm *et al.*, 'THz wave modulators: A brief review on different modulation techniques,' *Journal of Infrared, Millimeter, and Terahertz Waves*, vol. 34, pp. 1–27, 2013.

[63] L. Bibbò *et al.*, 'High-speed amplitude modulator with a high modulation index based on a plasmonic resonant tunable metasurface,' *Applied Optics*, vol. 58, no. 10, pp. 2687–2694, 2019.

[64] Y. Shen *et al.*, 'Nonlinear cross-phase modulation with intense single-cycle terahertz pulses,' *Physical Review Letters*, vol. 99, no. 4, p. 043 901, 2007.

[65] G. Sinatkas *et al.*, 'Electro-optic modulation in integrated photonics,' *Journal of Applied Physics*, vol. 130, no. 1, 2021.

[66] S. Hou *et al.*, 'High-speed electro-optic modulators based on thin-film lithium niobate,' *Nanomaterials*, vol. 14, no. 10, p. 867, 2024.

[67] H. Kato *et al.*, 'A high-speed GaAs-based electro-optic modulator for polarization, intensity, and phase modulation,' in *SPIE, The Nature of Light: What are Photons*, vol. 8832, 2013, pp. 27–33.

[68] Z. Wang *et al.*, 'Recent progress in terahertz modulation using photonic structures based on two-dimensional materials,' *InfoMat*, vol. 3, no. 10, pp. 1110–1133, 2021.

[69] R. R. Subkhangulov *et al.*, 'Terahertz modulation of the faraday rotation by laser pulses via the optical kerr effect,' *Nature Photonics*, vol. 10, no. 2, pp. 111–114, 2016.

[70] Y. Tan *et al.*, 'Ultrafast optical pulse polarization modulation based on the terahertz-induced kerr effect in low-density polyethylene,' *Optics Express*, vol. 28, no. 23, pp. 35 330–35 338, 2020.

[71] Y. Ji *et al.*, 'All-optical signal processing technologies in flexible optical networks,' *Photonic Network Communications*, vol. 38, pp. 14–36, 2019.

[72] S. Bigo *et al.*, 'All-optical fiber signal processing and regeneration for soliton communications,' *IEEE Journal of Selected Topics in Quantum Electronics*, vol. 3, no. 5, pp. 1208–1233, 1997.

[73] C. Li *et al.*, 'Superconducting complementary metamaterial based switchable device for terahertz wave manipulation,' *physica status solidi (b)*, vol. 260, no. 10, p. 2 300 203, 2023.

[74] Y. Chen *et al.*, 'Enhancement of high transmittance and broad bandwidth terahertz metamaterial filter,' *Optical Materials*, vol. 115, p. 111 029, 2021.

[75] P. K. Singh *et al.*, 'Metamaterials for remote generation of spatially controllable two dimensional array of microplasma,' *Scientific Reports*, vol. 4, no. 1, p. 5964, 2014.

[76] H. A. Hafez *et al.*, 'Extremely efficient terahertz high-harmonic generation in graphene by hot dirac fermions,' *Nature*, vol. 561, no. 7724, pp. 507–511, 2018.

[77] R. D. Averitt *et al.*, 'Terahertz metamaterial devices,' in *Terahertz Physics, Devices, and Systems II*, vol. 6772, 2007, pp. 23–31.

[78] J. O'Hara, J. Chen and T. Chang, 'A perspective on terahertz next generation wireless communications,' *Technologies*, vol. 7, no. 2, p. 43, 2019.

[79] S. Das, *Advances in terahertz technology and its applications*. Springer, 2021.

[80] Y. Liang *et al.*, 'Terahertz metadevices for silicon plasmonics,' *Chip*, vol. 1, no. 4, p. 100 030, 2022.

[81] H. Xing *et al.*, 'Terahertz metamaterials for free-space and on-chip applications: From active metadevices to topological photonic crystals,' *Advanced Devices & Instrumentation*, 2022.

[82] R. A. Lewis, *Terahertz Physics*. Cambridge University Press, 2004.

[83] Wang *et al.*, 'A review of THz modulators with dynamic tunable metasurfaces,' *Nanomaterials*, vol. 9, no. 7, p. 965, 2019.

[84] S. Guanet *et al.*, 'Recent progress of terahertz spatial light modulators: Materials, principles and applications,' *Micromachines*, vol. 13, no. 10, p. 1637, 2022.

[85] Yu-Lian *et al.*, 'Photo-excited silicon-based spatial terahertz modulators,' *Terahertz Science and Technology*, vol. 14, no. 1, pp. 1–19, 2021.

[86] M. McCluskey *et al.*, *Dopants and Defects in Semiconductors*. CRC Press, 2012.

[87] M. Cardona and F. Pollak, 'Energy-band structure of germanium and silicon: The kp method,' *Physical Review*, vol. 142, no. 2, p. 530, 1966.

[88] N. Arora *et al.*, 'Electron and hole mobilities in silicon as a function of concentration and temperature,' *IEEE Transactions on Electron Devices*, vol. 29, no. 2, pp. 292–295, 1982.

[89] J. Broisch *et al.*, 'Resistivity, doping concentrations, and carrier mobilities in compensated n- and p-type czochralski silicon: Comparison of measurements and simulations and consistent description of material parameters,' *IEEE Journal of Photovoltaics*, vol. 5, no. 5, pp. 1276–1284, 2015.

[90] R. van Schelven *et al.*, 'Drude dispersion in the transmission line modeling of bulk absorbers at sub-mm wave frequencies: A tool for absorber optimization,' *IEEE Antennas and Propagation Magazine*, vol. 64, no. 1, pp. 50–60, 2021.

[91] Karimi *et al.*, 'A quantum mechanical transport approach to analyze of dg silicon nanowire transistor,' in *2010 3rd International Nanoelectronics Conference*, 2010, pp. 602–603.

[92] A. Taheri, *Predicting Phonon Transport in Two-Dimensional materials Using First-Principles Calculations and the Boltzmann Transport Equation*. University of Toronto (Canada), 2020.

[93] L. D. Hong *et al.*, 'Switchable and tunable metamaterial absorber in THz frequencies,' *Journal of Science: Advanced Materials and Devices*, vol. 1, no. 1, pp. 65–68, 2016.

[94] A. Faramarz *et al.*, 'Design and analysis of a high-performance terahertz photoconductive modulator enhanced by photonic crystal cavity,' *Applied Physics B*, vol. 128, no. 11, p. 211, 2022.

[95] B. Jinjun *et al.*, 'A non-volatile tunable terahertz metamaterial absorber using graphene floating gate,' *Micromachines*, vol. 12, no. 3, p. 333, 2021.

[96] P. Goley *et al.*, 'Modeling transient loss due to ionizing particles in silicon photonic waveguides,' *IEEE Transactions on Nuclear Science*, vol. 69, no. 3, pp. 518–526, 2021.

[97] A. Kannegulla *et al.*, 'Photo-induced spatial modulation of THz waves: Opportunities and limitations,' *Optics express*, vol. 23, no. 25, pp. 32 098–32 112, 2015.

[98] C. Zhao *et al.*, 'Design optimization of silicon-based optically excited terahertz wave modulation,' in *Photonics*, MDPI, vol. 11, 2024, p. 202.

[99] Kamaruddin *et al.*, 'Some observations about the application of Fick's first law for membrane separation of multicomponent mixtures,' *Journal of membrane science*, vol. 135, no. 2, pp. 147–159, 1997.

[100] D. Heyes, 'System size dependence of the transport coefficients and Stokes–Einstein relationship of hard sphere and weeks–chandler–andersen fluids,' *Journal of Physics: Condensed Matter*, vol. 19, no. 37, p. 376 106, 2007.

[101] H. Nguyen *et al.*, 'Temperature dependence of the radiative recombination coefficient in crystalline silicon from spectral photoluminescence,' *Applied Physics Letters*, vol. 104, no. 11, 2014.

[102] S. Wang and D. Macdonald, 'Temperature dependence of Auger recombination in highly injected crystalline silicon,' *Journal of Applied Physics*, vol. 112, no. 11, 2012.

[103] A. G. Aberle, 'Surface passivation of crystalline silicon solar cells: A review,' *Progress in Photovoltaics: Research and Applications*, vol. 8, no. 5, pp. 473–487, 2000.

[104] R. Kumar *et al.*, 'Recombination parameters for antimonide-based semiconductors using rf photoreflection techniques,' Lockheed Martin Inc., NY 12301-1072 (US), Tech. Rep., 2002.

[105] M. Mrnka *et al.*, 'Terahertz imaging through emissivity control,' *Optica*, vol. 10, no. 12, pp. 1641–1646, 2023.

[106] S. Byrnes, 'Multilayer optical calculations,' *arXiv preprint:1603.02720*, 2016.

[107] Z. Fang *et al.*, 'THz modulation of monolayer WSe2-silicon hybrid structure and its performance after oxidation,' in *Infrared, Millimeter-Wave, and Terahertz Technologies V*, SPIE, vol. 10826, 2018, pp. 292–297.

[108] N. Yao, *Focused ion beam systems: basics and applications*. Cambridge University Press, 2007.

[109] L. A. Giannuzzi and F. A. Stevie, 'A review of focused ion beam milling techniques for tem specimen preparation,' *Micron*, vol. 30, no. 3, pp. 197–204, 1999.

[110] Li *et al.*, 'Recent advances in focused ion beam nanofabrication for nanostructures and devices: Fundamentals and applications,' *Nanoscale*, vol. 13, no. 3, pp. 1529–1565, 2021.

[111] J. Melngailis, 'Focused ion beam lithography,' *Nuclear Instruments and Methods in Physics Research Section B: Beam Interactions with Materials and Atoms*, vol. 80, pp. 1271–1280, 1993.

[112] B. David *et al.*, *The transmission electron microscope*. Springer, 2009.

[113] E. Ruska, 'The development of the electron microscope and of electron microscopy,' *Reviews of modern physics*, vol. 59, no. 3, p. 627, 1987.

[114] Findlay *et al.*, 'Dynamics of annular bright field imaging in scanning transmission electron microscopy,' *Ultramicroscopy*, vol. 110, no. 7, pp. 903–923, 2010.

[115] Shindo *et al.*, 'Energy dispersive x-ray spectroscopy,' *Analytical electron microscopy for materials science*, pp. 81–102, 2002.

[116] Weirich *et al.*, 'Structures of nanometre-size crystals determined from selected-area electron diffraction data,' *Foundations of Crystallography*, vol. 56, no. 1, pp. 29–35, 2000.

[117] Pennycook *et al.*, *Scanning transmission electron microscopy: imaging and analysis*. Springer Science & Business Media, 2011.

[118] Thermal Grizzly, *Kryosheet – graphene thermal pads*, `https://www.thermal-grizzly.com/en/kryosheet/s-tg-ks-24-12`, Accessed: 10 November 2024.

[119] Wall *et al.*, 'Titanium sapphire lasers,' *The Lincoln laboratory journal*, vol. 3, no. 3, pp. 447–462, 1990.

[120] Vengelis *et al.*, 'Supercontinuum generation in polarization maintaining photonic crystal fiber by using various harmonics of sub-nanosecond Q-switched laser,' in *Nonlinear Optics and its Applications IV*, SPIE, vol. 9894, 2016, pp. 236–246.

[121] J. Chin, 'Designing optical systems for terahertz spectroscopy,' Ph.D. dissertation, Worcester Polytechnic Institute, 2021.

[122] Qin *et al.*, 'A new envelope algorithm of Hilbert–Huang transform,' *Mechanical systems and signal processing*, vol. 20, no. 8, pp. 1941–1952, 2006.

[123] L. Downes *et al.*, 'Full-field terahertz imaging at kilohertz frame rates using atomic vapor,' *Physical Review X*, vol. 10, no. 1, p. 011 027, 2020.

[124] Hornbeck *et al.*, 'Digital micromirror device™: Commercialization of a massively parallel MEMS technology,' in *ASME International Mechanical Engineering Congress and Exposition*, American Society of Mechanical Engineers, vol. 18435, 1997, pp. 3–8.

[125] Dudley *et al.*, 'Emerging digital micromirror device (DMD) applications,' in *MOEMS display and imaging systems*, SPIE, vol. 4985, 2003, pp. 14–25.

[126] G. Shuping *et al.*, 'Lithographic pattern quality enhancement of DMD lithography with spatiotemporal modulated technology,' *Optics Letters*, vol. 46, no. 6, pp. 1377–1380, 2021.

[127] T. Sergey *et al.*, 'Comparison of nematic liquid-crystal and DMD based spatial light modulation in complex photonics,' *Optics express*, vol. 25, no. 24, pp. 29 874–29 884, 2017.

[128] Evans *et al.*, 'How good are my data and what is the resolution?' *Biological crystallography*, vol. 69, no. 7, pp. 1204–1214, 2013.

[129] D. Dan *et al.*, 'DMD-based LED-illumination super-resolution and optical sectioning microscopy,' *Scientific reports*, vol. 3, no. 1, p. 1116, 2013.

[130] Perrin *et al.*, 'Fourier optics: Basic concepts,' *arXiv preprint arXiv:1802.07161*, 2018.

[131] M. Braun, *Eadweard Muybridge*. Reaktion Books, 2012.

[132] R. Howells, 'Louis Le Prince: The body of evidence,' *Screen*, vol. 47, no. 2, pp. 179–200, 2006.

[133] Por *et al.*, 'Nyquist–Shannon sampling theorem,' *Leiden University*, vol. 1, no. 1, pp. 1–2, 2019.

[134] J.-L. Starck and F. Murtagh, 'Astronomical image and signal processing: Looking at noise, information and scale,' *IEEE Signal Processing Magazine*, vol. 18, no. 2, pp. 30–40, 2001.

[135] Stelzer, 'Contrast, resolution, pixelation, dynamic range and signal-to-noise ratio: Fundamental limits to resolution in fluorescence light microscopy,' *Journal of Microscopy*, vol. 189, no. 1, pp. 15–24, 1998.

[136] I. A. Cunningham and R. Shaw, 'Signal-to-noise optimization of medical imaging systems,' *Journal of the optical society of America A*, vol. 16, no. 3, pp. 621–632, 1999.

[137] U. Ingard, *Noise reduction analysis*. Jones & Bartlett Publishers, 2009.

[138] H. R. Petty, 'Fluorescence microscopy: Established and emerging methods, experimental strategies, and applications in immunology,' *Microscopy research and technique*, vol. 70, no. 8, pp. 687–709, 2007.

[139] R. H. Kumar *et al.*, 'Anti-reflective coatings: A critical, in-depth review,' *Energy & Environmental Science*, vol. 4, no. 10, pp. 3779–3804, 2011.

[140] J. Piotrowski *et al.*, 'Optical diffraction simulation of a digital micromirror device,' in *Emerging Digital Micromirror Device Based Systems and Applications XIV*, SPIE, vol. 12014, 2022, pp. 45–52.

[141] R. R. Alfano, *The supercontinuum laser source: fundamentals with updated references*. Springer, 2006.

[142] Wilson *et al.*, 'First, second and third order blazes of diffraction gratings,' *Journal of Optics*, vol. 8, no. 4, p. 217, 1977.

[143] Timoshenko *et al.*, 'Quantitative analysis of room temperature photoluminescence of c-Si wafers excited by short laser pulses,' *Journal of Applied Physics*, vol. 85, no. 8, pp. 4171–4175, 1999.

[144] Hessel *et al.*, 'Bragg-angle blazing of diffraction gratings,' *Journal of the optical society of America*, vol. 65, no. 4, pp. 380–384, 1975.

[145] T. Instruments, 'Dmd optical efficiency for visible wavelengths,' *Application Report*, 2019.

[146] R. Casini and P. Nelson, 'On the intensity distribution function of blazed reflective diffraction gratings,' *Journal of the Optical Society of America A*, vol. 31, no. 10, pp. 2179–2184, 2014.

[147] L. Jinyang *et al.*, 'Grayscale laser image formation using a programmable binary mask,' *Optical Engineering*, vol. 51, no. 10, pp. 108 201–108 201, 2012.

[148] M. Berzelius, 'XLII. on the mode of obtaining silicium, and on the characters and properties of that substance,' *The Philosophical Magazine*, vol. 65, no. 324, pp. 254–267, 1825.

[149] G. L. Pearson and J. Bardeen, 'Electrical properties of pure silicon and silicon alloys containing boron and phosphorus,' *Physical Review*, vol. 75, no. 5, p. 865, 1949.

[150] M. Riordan, 'The lost history of the transistor,' *IEEE spectrum*, vol. 41, no. 5, pp. 44–46, 2004.

[151] B. Razavi, *Fundamentals of microelectronics*. John Wiley & Sons, 2021.

[152] R. R. Schaller, 'Moore's law: Past, present and future,' *IEEE spectrum*, vol. 34, no. 6, pp. 52–59, 1997.

[153] J. D. Meindl, 'Chips for advanced computing,' *Scientific American*, vol. 257, no. 4, pp. 78–89, 1987.

[154] A. Muller *et al.*, 'Silicon for photovoltaic applications,' *Materials Science and Engineering: B*, vol. 134, no. 2-3, pp. 257–262, 2006.

[155] S. Middelhoek *et al.*, 'Silicon sensors,' *Measurement Science and Technology*, vol. 6, no. 12, p. 1641, 1995.

[156] M. Green *et al.*, 'Efficient silicon light-emitting diodes,' *Nature*, vol. 412, no. 6849, pp. 805–808, 2001.

[157] Tsao *et al.*, 'Ultrawide-bandgap semiconductors: Research opportunities and challenges,' *Advanced Electronic Materials*, vol. 4, no. 1, p. 1 600 501, 2018.

[158] D. B. S. Sethuraman and C.-J. Liu, 'Doping methods and their effects,' in *Handbook of Semiconductors*, CRC Press, 2025, pp. 54–67.

[159] M. Masanobu *et al.*, 'Recent progress of heterostructure technologies for novel silicon devices,' *Applied surface science*, vol. 102, pp. 360–371, 1996.

[160] J. Blakemore, 'Semiconducting and other major properties of gallium arsenide,' *Journal of Applied Physics*, vol. 53, no. 10, R123–R181, 1982.

[161] E. Williams *et al.*, 'Indium phosphide: A photoluminescence materials study,' *Journal of The Electrochemical Society*, vol. 120, no. 12, p. 1741, 1973.

[162] K. Novoselov *et al.*, 'Electronic properties of graphene,' *physica status solidi (b)*, vol. 244, no. 11, pp. 4106–4111, 2007.

[163] G. V. Naik and A. Boltasseva, 'A comparative study of semiconductor-based plasmonic metamaterials,' *Metamaterials*, vol. 5, no. 1, pp. 1–7, 2011.

[164] Z. Chen *et al.*, 'Graphene controlled brewster angle device for ultra broadband terahertz modulation,' *Nature communications*, vol. 9, no. 1, p. 4909, 2018.

[165] J. S. Li *et al.*, 'Enhancement of silicon modulating properties in the THz range by YAG-Ce coating,' *Scientific Reports*, vol. 10, no. 1, p. 6605, 2020.

[166] Z. Galazka, 'Czochralski method,' *Gallium Oxide: Materials Properties, Crystal Growth, and Devices*, pp. 15–36, 2020.

[167] P. Van der Heide, *Secondary ion mass spectrometry: an introduction to principles and practices*. John Wiley & Sons, 2014.

[168] O. Faix, 'Fourier transform infrared spectroscopy,' in *Methods in lignin chemistry*, Springer, 1992, pp. 83–109.

[169] R. Phillips, 'Selected-area diffraction in the electron microscope,' *British Journal of Applied Physics*, vol. 11, no. 11, p. 504, 1960.

[170] W. Dietze, W. Keller and A. Mühlbauer, 'Float-zone grown silicon,' in *Silicon*, Springer, 1981, pp. 1–42.

[171] T. Digges and C. Yaws, 'Preparation of high-resistivity silicon by vacuum float zoning,' *Journal of The Electrochemical Society*, vol. 121, no. 9, p. 1222, 1974.

[172] D. E. Aspnes and A. Studna, 'Dielectric functions and optical parameters of Si, Ge, GaP, GaAs, GaSb, InP, InAs, and InSb from 1.5 to 6.0 ev,' *Physical review B*, vol. 27, no. 2, p. 985, 1983.

[173] Schroder *et al.*, 'Free carrier absorption in silicon,' *IEEE Journal of solid-state circuits*, vol. 13, no. 1, pp. 180–187, 1978.

[174] Baker-Finch *et al.*, 'Near-infrared free carrier absorption in heavily doped silicon,' *Journal of Applied Physics*, vol. 116, no. 6, 2014.

[175] Dasilva-Villanueva *et al.*, 'Bulk carrier lifetime surpassing 600 us in upgraded metallurgical-grade silicon multicrystalline wafers after phosphorus diffusion gettering,' *arXiv preprint arXiv:2111.13522*, 2021.

[176] D. Baek *et al.*, 'Surface recombination velocity of silicon wafers by photoluminescence,' *Applied Physics Letters*, vol. 86, no. 11, 2005.

[177] Z. Xie *et al.*, 'Spatial terahertz modulator,' *Scientific Reports*, vol. 3, no. 1, p. 3347, 2013.

[178] L.-J. Cheng and L. Liu, 'Optical modulation of continuous terahertz waves towards cost-effective reconfigurable quasi-optical terahertz components,' *Optics express*, vol. 21, no. 23, pp. 28 657–28 667, 2013.

[179] Paschotta *et al.*, 'Ytterbium-doped fiber amplifiers,' *IEEE Journal of quantum electronics*, vol. 33, no. 7, pp. 1049–1056, 1997.

[180] P. Russell, 'Photonic crystal fibers,' *science*, vol. 299, no. 5605, pp. 358–362, 2003.

[181] A. Arnau *et al.*, *Piezoelectric transducers and applications*. Springer, 2004, vol. 2004.

Appendix A

FIB, TEM, and EDS System Diagrams

This appendix contains information concerning the Focused Ion Beam (FIB) milling system used for silicon lamella preparation described in **Chapter 3**. Additionally, information on the Transmission Electron Microscopy (TEM) and its subsystem for Energy-Dispersive X-ray Spectroscopy (EDS) is covered. These systems are used in **Chapter 5** for silicon characterisation.

A.1 FIB Lamella Preparation

Preparing a sample for TEM using FIB is a precise process aimed at producing an electron-transparent lamella while minimising artefacts. The first step is depositing a protective layer over the region of interest to shield it from ion-induced damage, amorphisation, and redeposition as seen in **Figure A.1** ***a)***. This layer is typically 0.5–2 µm thick and is composed of platinum (Pt). Electron-beam-assisted deposition results in a thinner, uniform layer with minimal ion-induced defects, making it ideal for delicate samples such as semiconductors.

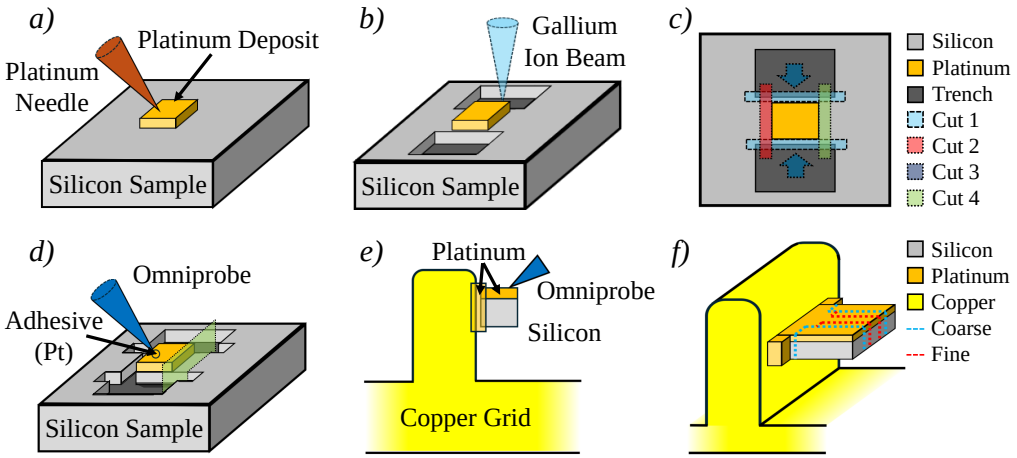

Figure A.1: TEM sample preparation using FIB milling. ***a)*** Deposition of a platinum protective layer on the silicon sample. ***b)*** Coarse milling with high energy gallium ion beam perpendicular to sample. ***c)*** Location of finer resolution milling cuts 1 - 4 with cuts 2 - 4 being done at 52 degrees to the sample. ***d)*** Attachment of omniprobe with platinum acting as adhesive prior to cut 4 which separates the lamella from the sample. ***e)*** Positioning and attachment of the lamella to the TEM copper grid. ***f)*** Thinning process for the lamella consisting of coarse and then fine milling from a perpendicular gallium ion beam.

After deposition, bulk milling is performed using a high-current Ga^+ ion beam at 20–30 kV and 10–30 nA to rapidly remove material and isolate the lamella through trench milling seen in **Figure A.1** ***b)***. Controlling the beam's angle and scan pattern minimises redeposition effects. In ***c)*** we see the finer trench cuts 1-4 using the same technique but with less power. Cut 1 is performed perpendicular to the sample, while cuts 2-4 are performed at a tilted 52° to the sample. The lamella is then ready for extraction and transfer to a TEM grid using a micromanipulator omniprobe. The probe is attached to the sample via ion-beam-induced platinum deposition in ***d)***, securing a stable connection. The sample is freed from the bulk material using low-current FIB milling to prevent stress fractures before being lifted onto a TEM grid in ***e)***, commonly copper or molybdenum, and permanently affixed with further platinum deposition.

Final thinning shown in **Figure A.1** ***f)*** ensures electron transparency, typically reducing the sample to below 100 nm. This process is carried out in stages using progressively lower ion beam currents. Intermediate coarse thinning at 50–100 pA

and 5–8 kV refines thickness while limiting damage. A final low-energy ion fine polish step at 2–5 kV with ion currents below 50 pA removes amorphisation layers, gallium implantation, and curtaining artefacts, improving sample quality. The final thickness depends on analytical needs but typically ranges between 30 and 100 nm.

Challenges such as gallium implantation and curtaining effects require precise control of milling parameters, beam scanning patterns, and a final low-energy polishing step. These refinements ensure high-quality samples suitable for advanced TEM analysis.

A.2 TEM Schematic

The TEM microscope consists of several key components that work together to generate high-resolution images as shown in **Figure A.2**. The electron source (electron gun) produces a high-energy beam, typically through thermionic or field emission. This beam is controlled by a condenser lens system, which ensures proper focus before interaction with the sample. The specimen holder and stage position the thin sample (prepared using FIB milling) precisely. The objective lenses form the primary image, aided by an objective aperture that enhances contrast by filtering scattered electrons. Additionally, a selected area aperture is found in this imaging and diffraction patterning section and is responsible for enabling Selected Area Electron Diffraction (SAED) imaging. Intermediate and projector lenses further magnify the image, which is then captured using fluorescent screens, Charge-Coupled Devices, or direct electron detectors. Since electrons are easily scattered in air, the system operates under ultra-high vacuum conditions.

The principles of TEM are based on the interaction of a high-energy electron beam with an ultra-thin sample. The electron gun generates a beam, which is accelerated to energies between 80 keV and 300 keV, allowing for atomic-scale imaging due to the short electron wavelength. When electrons pass through the

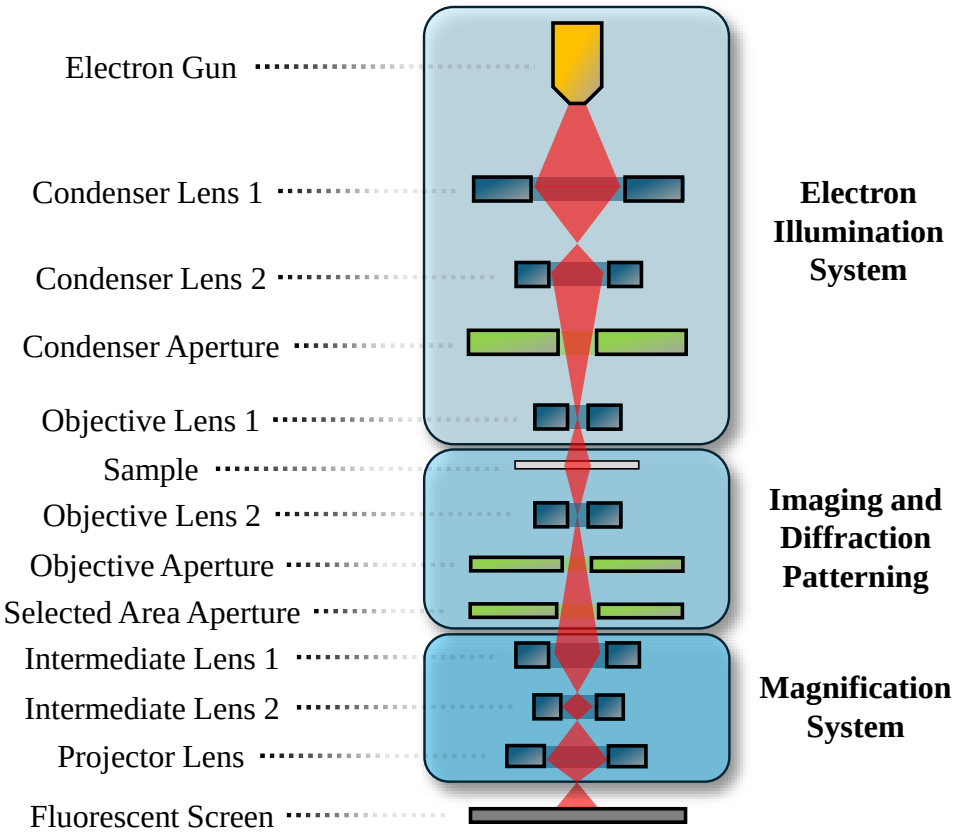

Figure A.2: TEM schematic depicting three main sections and their respective components. The sections are an electron illumination system, imaging and diffraction patterning, and a magnification system.

sample, they experience elastic scattering, where their direction changes without energy loss, and inelastic scattering, where they lose energy, producing secondary signals such as X-rays. The transmitted and scattered electrons form an image, with contrast arising from differences in thickness, density, and composition. The final image is magnified and detected, revealing structural details down to atomic resolution.

A.3 EDS Schematic

The principle of EDS is based on inelastic electron scattering. When the high-energy electron beam in TEM interacts with the atoms in a specimen, as seen in

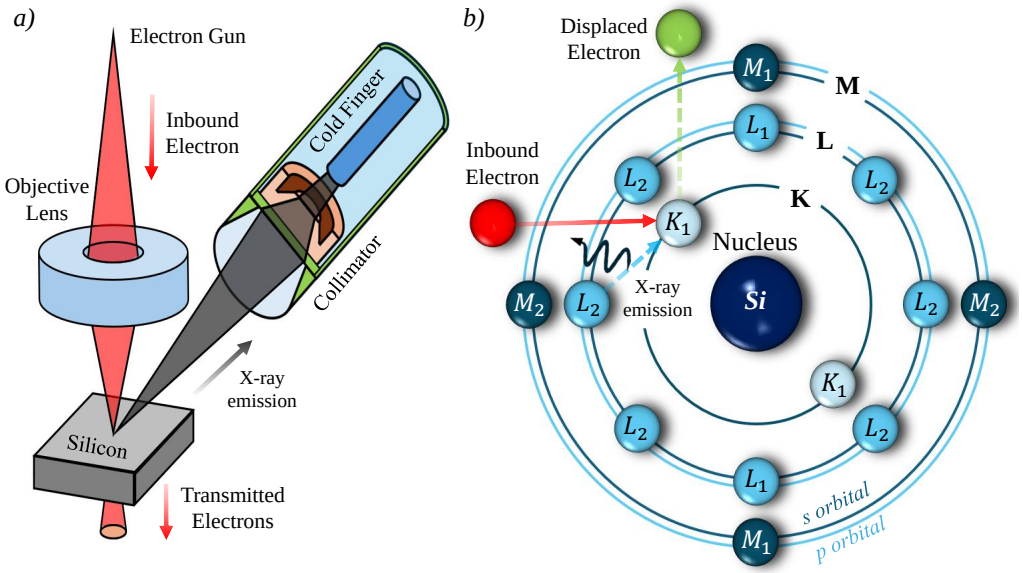

Figure A.3: ***a)*** Schematic of an electron gun firing electrons towards a silicon sample through an objective lens, leading to some transmission electrons, and some characteristic X-ray emission which is captured and detected. ***b)*** Silicon electron orbital diagram depicting an inbound electron displacing a K_1 and being replaced by an L_2 electron after it emits X-ray energy.

Figure A.3 ***b)*** it can eject an inner-shell electron, creating an electron vacancy. To restore stability, an electron from a higher energy shell transitions to fill the vacancy, releasing energy in the form of an X-ray photon. The energy of this emitted X-ray corresponds to the specific element's atomic structure, allowing identification through an energy spectrum.

Appendix **B**

Super Continuum Schematic Diagrams

This appendix contains information concerning the NKTEvo SuperK and Titanium Sapphire lasers. These lasers, and their corresponding methods, are discussed in **Chapter 3**, and they are used for characterisation in **Chapter 4** and **Chapter 5** respectively. The NKTEvo SuperK laser is used to characterise the power efficiency of the DMD, and the Ti:Sapphire laser is used to characterise the wavelength dependence of silicon's modulation depth.

B.1 Ti:Sapphire Schematic

The MSquared SolsTiS Ti:Sapphire laser used in this work has a bowtie cavity configuration as seen in **Figure B.1** ***a)***. In this arrangement, two curved mirrors focus the intracavity beam into a tight waist within the gain medium (which is the titanium-doped sapphire crystal), enhancing the mode matching efficiency and reducing beam divergence. The remaining two mirrors in the cavity are typically flat, with one serving as an output coupler, partially transmitting intracavity radiation to produce the final laser output, and the other is a piezoelectric actuator used for cavity length stabilisation.

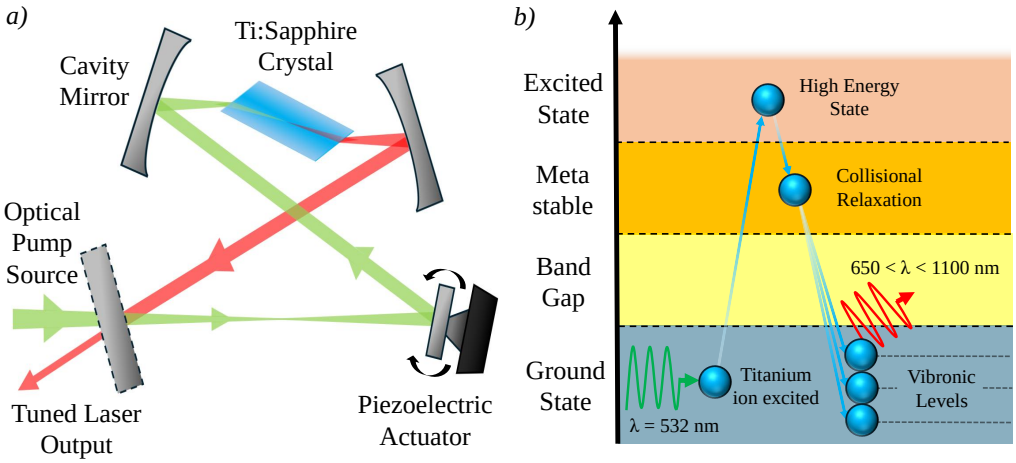

Figure B.1: ***a)*** A bowtie cavity which forms a tight intracavity beam in the titanium-doped sapphire crystal gain medium. Both the optical pump beam and tuned laser output pass through a partially transparent mirror. Additionally, a piezoelectric actuator is used for cavity length stabilisation. ***b)*** An energy band diagram for the titanium ions in the sapphire crystal depicting the process of excitation from a 532 nm pump source, collisional relaxation, and eventual stabilisation into a ground state vibronic level producing 650-1100 nm radiation.

The energy bands of the gain medium are depicted in **Figure B.1** ***b)***. This medium is doped with titanium ions at a low concentration of around 0.1%. When exposed to the optical pump, which is 532 nm, these ions become excited to a high energy state. Over time, these excited ions undergo collisional relaxation into a metastable state. Finally, ions return to the ground state, specifically into one of several potential vibronic levels. During this process, wavelengths between 650 and 1100 nm are produced depending on which vibronic level the ions move to.

B.2 NKTEvo SuperK Schematic

The laser generates a super continuum by first generating a mode-locked ytterbium seed laser at 1064 nm. This is then fed into a fiber amplifier [179] to boost the seed laser power up to 10 W as seen in **Figure B.2** ***a)***. This is achieved by ytterbium ions (Yb^{3+}) in the fiber being excited creating a population inversion leading to stimulated emission. Now to generate the super continuum, the boosted laser is fed into photonic crystal fibers [180]. This process induces nonlinear optical

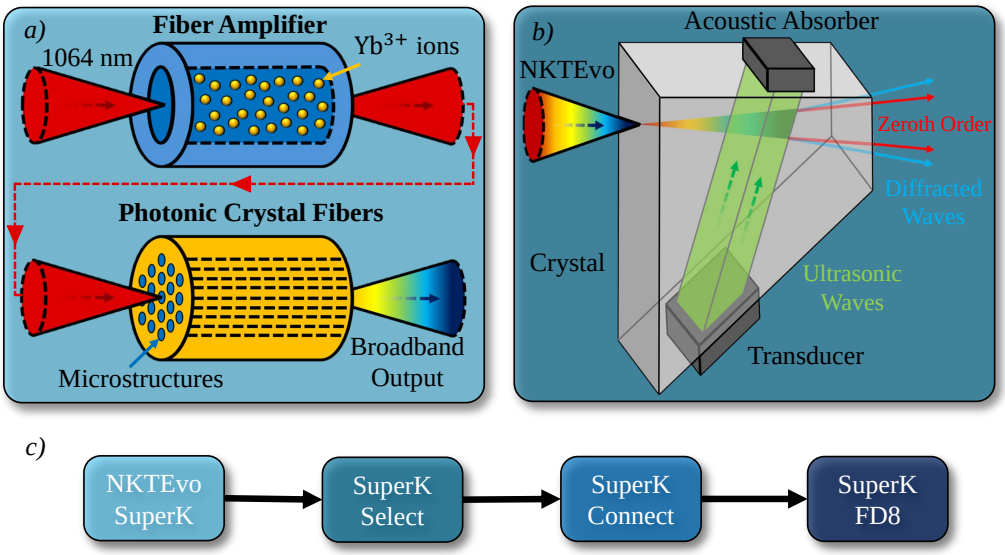

Figure B.2: ***a)*** The NKTEvo SuperK with a 1064 nm seed laser leading to a ytterbium doped fiber amplifier, boosting the output power to 10 W. This is then fed into photonic crystal fibers with built-in microstructures to create the broadband output (400-2400 nm). ***b)*** The SuperK Select schematic depicting a Tellurium Dioxide crystal with a piezoelectric transducer. The transducer generates ultrasonic waves to alter the crystal's refractive index which now acts like a diffraction grating on the inbound NKTEvo beam, generating tunable zeroth order waves as a spectral filter. ***c)*** A flowchart for the full super continuum laser system starting with the NKTEvo laser source, leading to the SuperK Select spectral filter, then the SuperK Connect which couples the output into the SuperK FD8 fiber output cables.

effects such as self-phase modulation, four-wave mixing, and stimulated Raman scattering, resulting in a broad and continuous spectrum covering the ultraviolet to near-infrared regions.

To achieve precise wavelength selection within this broad spectrum, the SuperK Select module is employed as seen in **Figure B.2** ***b)***. Utilising acousto-optic tunable filter technology, the SuperK Select allows for rapid and accurate tuning across multiple wavelength bands [181]. The filters are made from either Tellurium Dioxide (TeO_2) or quartz (SiO_2) and are attached to a piezoelectric transducer. The transducer generates ultrasonic waves into the crystal causing a period variation in the refractive index which act as a phase grating to diffract the super continuum laser. This acts as a variable spectral filter on the laser such that by altering the ultrasonic waves, we vary the most efficiently diffracted waves being

generated according to the Bragg condition. Using this, the SuperK Select covers tuning ranges such as 500-900 nm (VIS-nIR - our use case), 640-1100 nm (nIR1), 800-1400 nm (nIR2), and 1100-2000 nm (IR), depending on the specific crystal installed.

For stable and efficient fiber delivery of the super continuum light, the SuperK Connect system is utilised. This high-performance fiber delivery system ensures easy and stable single-mode coupling that can be disconnected and reconnected without alignment. The SuperK FD8 fibers cover the 400-2000 nm spectrum, and users can choose from various termination options, including FC/PC connectors or high-quality collimators, facilitating seamless integration into experimental setups. The full super continuum flowchart is shown in **Figure B.2** ***c)*** depicting the laser, the spectral filter, the fiber connector, and the fiber output for the system.

The NKTEvo laser system, along with its SuperK Select and SuperK Connect modules, is controlled via NKT Photonics' proprietary software, SuperKontrol. This intuitive interface allows customisable laser operation parameters, including wavelength tuning, power control, and pulse configuration. The software supports real-time adjustments and monitoring, ensuring precise control over experimental conditions and facilitating efficient data acquisition.

Appendix C

Thermal Mount Schematics, and DMD Mirrors

This appendix contains information regarding the final THz modulator design in **Chapter 3**, specifically a focused view of the custom thermal mounting solution, and analysis of the DMD mirrors from the Vialux V7000 device used in the modulator from **Chapter 4**.

C.1 Thermal Mount Design

The high intensity production of optical radiation from the diodes discussed in **Chapter 3** required an effective cooling mount to ensure the diodes remained at optimal operating temperatures, ensuring prolonged use. Initial testing was conducted with a simplistic mount seen in **Figure 3.6** which was an aluminium block, engineered to hold the diode without any active cooling elements. After analysing thermal images of the mount, it was found that significant thermal build up was occurring around the diode, potentially leading to diode deterioration. To prevent this, a custom mount was designed and built to actively dissipate this build up.

Figure C.1 depicts the thermal mount utilised in this work consisting of

a TECF2S thermal cooling element and Kryosheet cooling elements discussed in **Chapter 3**. The mount is split into three sections, and upper cold plate, a lower hot plate and the separating cooling elements between these two plates. The upper plate is where the diodes were placed and powered by the SR9HF-DB9 cable. To secure the diodes to the plate, an additional front plate is used which matched the shape of the diodes to maximise contact and ensure effective thermal dissipation from the diode into the upper mount. The upper mount is then separated from the lower mount entirely by the active cooling elements to enable the cooling elements to effectively control the amount of dissipation taking place.

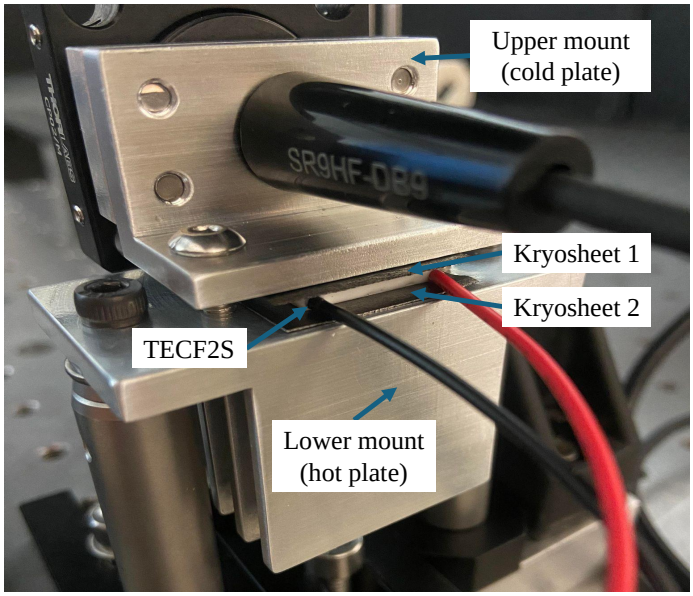

Figure C.1: The final custom thermal mount design consisting of an upper (cold plate) and lower (hot plate) mount, separated by the cooling elements of Kryosheets and TECF2S. The upper plate is where the diode is situated and powered by the SR9HF-DB9 cable shown. There is a front plate securing the diode to the upper mounting plate.

An MPT2500 controller unit is used along side a TH10K thermistor to monitor and control the cooling provided by the TECF2S unit. To monitor the temperature of the upper mount and thereby also the diode, the TH10K thermistor is attached to the upper mount via the use of EC360 thermally conductive glue. This glue is stated to have 2 W/mK of thermal conductivity which should be more than adequate for all our use cases. The 1.8 mpa bond strength ensures the glue can

effectively attach the thermistor directly to the aluminium casing used without concerns of the thermistor detaching.

Adjustments to the temperature and gain potentiometers on the MPT2500 controller board while monitoring with the thermal camera sets the mount to manipulate the temperatures of the upper mount to within a reliable range for diode operation. Tests showed the upper mount remained at approximately 20°C while the lower mount never exceeded 65°C as seen in **Chapter 3**. The lower mount has a typical heat sink design engineered into it to ensure dissipation of collected heat into the air.

C.2 DMD Mirrors and Terminology

In **Chapter 4**, extensive characterisation of the DMD is covered. The DMD is a device consisting of millions of micron sized mirrors whose dimensions were listed by the manufacturer but were verified in **Figure C.2** ***a)*** with the use of a light microscope.

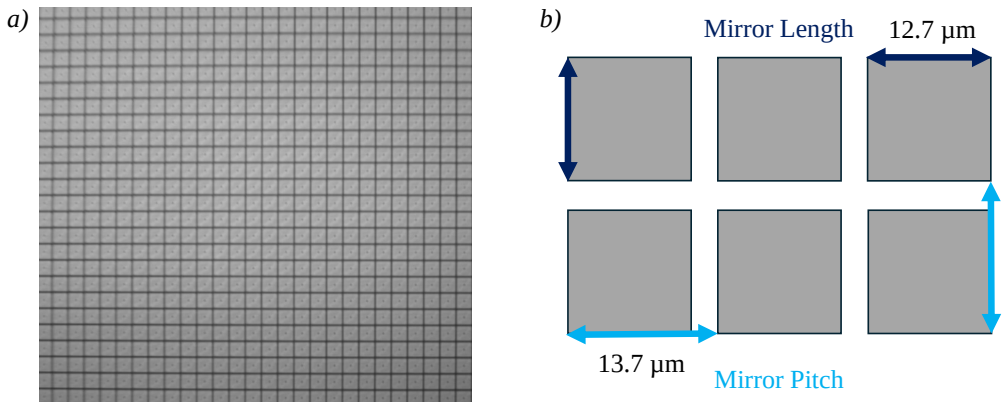

Figure C.2: ***a)*** The image of the DMD mirrors when captured with a light microscope. ***b)*** Diagram explaining the differences in terminology for mirror length and pitch which were found to be 12.7 and 13.7 µm respectively.

By taking the magnification of the light microscope system, and comparing a grid of known dimensions to that of the DMD mirrors, the dimensions of the mirrors can be calculated. **Figure C.2** ***b)*** shows the results of the calculations with

explanation for the common terminology used where mirror length is the actual height and width of the square mirrors in question, and mirror pitch is the dimensions for both the mirror length in combination with the gap between the mirrors. Having accurate measurements for these quantities is vital for the simulation posed in **Section 4.4.1** which takes into account the mirror pitch dimensions.

In addition to enabling calculations for the mirror dimensions, **Figure C.2** ***a)*** also enables examination of the condition of the DMD. Over time, it is not uncommon for the mirror array to have some variation in the float state of the mirrors such that when in float state (between 'on' and 'off'), the mirrors are not all completely flat. This lack of complete relaxation can indicate some of the mirrors are no longer functional and the 'on' and 'off' states will not be entered as expected. By looking at the mirrors in the float state here, we can verify that the mirror reflections are similar and in all likelihood, the vast majority of the array is functional and the DMD is in good working condition.